Multidisciplinary Optimization for the Design and Control of Uncertain Dynamical Systems

by

Srikanth Sridharan

A Dissertation Presented in Partial Fulfillment
of the Requirement for the Degree
Doctor of Philosophy

Approved February 2014 by the
Graduate Supervisory Committee:

Armando A. Rodriguez, Chair
Hans D. Mittelmann
Jennie Si
Konstantinos S. Tsakalis

ARIZONA STATE UNIVERSITY

May 2014

ABSTRACT

This dissertation considers an integrated approach to system design and controller design based on analyzing limits of system performance. Historically, plant design methodologies have not incorporated control relevant considerations. Such an approach could result in a system that might not meet its specifications (or one that requires a complex control architecture to do so). System and controller designers often go through several iterations in order to converge to an acceptable plant and controller design.

The focus of this dissertation is on the design and control an air-breathing hypersonic vehicle using such an integrated system-control design framework. The goal is to reduce the number of system-control design iterations (by explicitly incorporate control considerations in the system design process), as well as to influence the guidance/trajectory specifications for the system.

Due to the high computational costs associated with obtaining a dynamic model for each plant configuration considered, approximations to the system dynamics are used in the control design process. By formulating the control design problem using bilinear and polynomial matrix inequalities, several common control and system design constraints can be simultaneously incorporated into a vehicle design optimization. Several design problems are examined to illustrate the effectiveness of this approach (and to compare the computational burden of this methodology against more traditional approaches).

DEDICATION

To the five I care most for.

TABLE OF CONTENTS

CHAPTER Page

CHAPTER Page

CHAPTER Page

CHAPTER Page

CHAPTER Page

LIST OF TABLES

LIST OF FIGURES

Figure Page

INTRODUCTION.

1.1 Overview

This dissertation addresses a multidisciplinary optimization for the integrated approach to the design and control of systems. Traditionally, an iterative approach is taken to system design and control: the system is designed using rule-of-thumb guidelines, and control relevant considerations are not explicitly incorporated in the system design phase or in framing the specifications. Control engineers use the resulting system design and attempt to meet project specifications. If they are unsuccessful, the system design is revisited. Such an iterative approach can be time-consuming and expensive. In addition, the specifications themselves might be unreasonable for the class of acceptable system designs.

In order to address these shortcomings in the iterative system and controller design process, an integrated framework that incorporates control considerations in all phases of the project (formulating specifications, designing systems, and designing controllers) is required. We list some of the important characteristics that require closed loop and control limitations early in the design phase

Limited Controls: Saturation limitations are present in every real-world system. In the case of an aircraft, the saturation effects include mechanical limitations (such as elevator deflection saturation or rate limitations on fuel injection).

Non-minimum Phase characteristics: Non minimum phase characteristics (such as a right half plane zero or a time delay) can limit achievable trajectories and perfor-

mance (such as frequency domain peaks). Hypersonic aircraft suffer from such limitations.

Bandwidth limitations: Bandwidth limitations significantly limit closed loop performance. Such limitations can be due to sampling/update frequency, communication delays, etc. It is important to consider these limitations early in the design phase.

In this dissertation, we consider the problem of designing an air-breathing hypersonic vehicle to execute a pull-up maneuver. The impact of design on achievable performance (which influences specifications and guidance decisions) is examined, as well as the design of a controller. The focus of control design is on computationally efficient methodologies to integrate system and controller design such as convex optimization based techniques.

The work presented in this research document have appeared in several publications [1–12]. It is not the authors intention to claim sole credit for all results presented in this dissertation. However, they are presented in their entirety for completeness.

1.2 Motivation

Historically, control related considerations have not played a significant role in system design. As the complexity of systems continue to soar, the need for sophisticated computer aided design tools has never been greater.

The critical motivation here is that systems are often designed without taking into account control considerations. This was the case with the Chernobyl 1986 disaster a classic case of an unstable system operating in the presence of limited control (cooling) authority.

Recently, control and performance relevant constraints have played a greater role in system design due to limitations in the classical approach:

- In [13] the author describes how the initial X-29 aircraft designs were almost too unstable to control due to limitations introduced by the bandwidth of the hardware.
- Data centers are traditionally been designed based on static analysis of thermal flows and cooling, while the task distribution algorithms and control of cooling mechanisms have been considered after the layout of the data center is finalized.
- In [14] the authors describe how higher power density of modern microprocessors requires architecture design tools that incorporate achievable cooling performance in the floorplan design process.

Multidisciplinary optimization (MDO) attempts to address this by formulating a design optimization incorporating constraints from multiple disciplines simultaneously. Integrating control and performance specifications into system design, however, can be computationally expensive due to the nonlinear relation between the system and the closed loop map. In this research, emphasis is placed on computationally efficient methodologies (such as convex optimization techniques via Linear Matrix Inequalities, vector space optimization, etc) to integrate system and controller design.

1.3 Related Work and Literature Survey

1.3.1 Design and Control of Air-Breathing Hypersonic Vehicles

One of the first control-relevant design of a generic 3-Degrees of Freedom (DOF) hypersonic vehicle is considered in [15]. The authors use classical 2D Newtonian impact theory to approximate the aerodynamic forces and moments. The scramjet combustor is modeled

using 1D-Rayleigh flow. A single bending mode was included based on a NASTRAN derived mode shape. Another model using oblique shock-expansion theory is developed in [16]; the model is validated using Euler-based (inviscid) computational fluid dynamic models. A model that uses an Euler-Bernoulli beam based flexible model was developed in [17], and forms the basis of the models used in this work. A more comprehensive survey of 3-DOF and 6-DOF hypersonic vehicle models can be found in [18].

1.3.2 Multidisciplinary Optimization

Multidisciplinary optimization has been used for the design of aircraft systems and structural optimization [19]. While many different optimization techniques can be used, a gradient free method tend to be computationally faster, as computing derivatives is computationally expensive in many application areas (such as the examples considered in this dissertation). Multidisciplinary optimization architectures can be categorized into two broad classes [20]:

Monolithic : These algorithms solve a single optimization problem, and the multidisciplinary constraints can be handled in several different ways such as (1) Simultaneous Analysis and Design (SAND) [21], (2) Individual Discipline Feasible [22], or Multidisciplinary Feasible (MDF) [22]. The methodology in this dissertation is based on MDF.

Distributed : This class of algorithms decompose the original optimization into multiple smaller optimizations that result in the same solution when reassembled. The division generally exploits the structure of the problem (e.g. network flow or resource allocation problems [23]).

In order to solve the optimization problem, several approaches can be used; a gradient free optimization strategy is used for the main multidisciplinary optimization considered in this work. A survey of derivative free optimization methodologies is presented in [24]. They can be divided into two main categories:

Direct : Direct algorithms (such as Nelder-Mead algorithms [25], Generalized Pattern Search [26], Pattern search using simplex gradient [27], and Divide a Hyper-rectangle [28]) use the objective function value directly in computing search directions.

Model-Based : Model-based algorithms use a surrogate to the objective to guide the search process. These methods include trust-region methods [29], implicit filtering [30], and response-surface methods [31].

1.3.3 Integrated System-Controller Design

In [32] the authors identify the following plant properties that limit achievable closed loop performance irrespective of the controller used: Non-minimum phase (NMP) characteristics (RHP zeros and time-delays) [33–36], plant-model mismatch, and state constraints. Hypersonic vehicles (considered in this dissertation) possess several of these characteristics, and can significantly benefit from an integrated vehicle-controller design procedure. A control-centric approach to system design can result in significant improvement in closed loop performance [37]. This dissertation considers one such integrated approach to plant and controller design.

In [38], the authors consider the problem of integrated optimization of a single parameter plant and controller using an LMI-based approach. An iterative linear matrix inequalities (LMI) based approach (iterate over controller design and plant design) has

been considered in [39]. A simultaneous plant-controller redesign has been considered in [40]. In [41], the authors look at the coupling between modeling, uncertainty, and specifications affects a measure of coupling between the modeling and control design problems. The limitations of a non-integrated approach to system design and control design is explored in [37]. Several performance limitations and tradeoffs in feedback control can be found in the special section [42].

1.4 Organization

The rest of this document is organized as follows: mathematical preliminaries are presented in Chapter 2, and an integrated system and control design framework is presented in Chapter 3. Chapters 4 and 5 examine the modeling and control of an air-breathing hypersonic vehicle. Trade studies to assess the impact of design decisions on the static and dynamic properties of the vehicle are presented in Chapter 6. The application of the multidisciplinary optimization to the design of the hypersonic vehicle is considered in Chapter 7. A summary of this research, as well as future research directions is presented in chapter 8.

2

MATHEMATICAL PRELIMINARIES.

In this chapter mathematical results used in the rest of this dissertation are presented in a general form. In subsequent chapters application specific expressions derived from these results are used in order to gain system-specific insight. Section 2.3 presents results on performance limitations in various metrics. A discussion on the numerical optimization techniques used in this dissertation can be found in Section 2.2.

2.1 Notation and Preliminaries

2.1.1 Overview

In this section the notation and results used in the rest of this chapter are presented. The theorems are presented in a general form, and specific applications are considered later in this chapter. The definitions and theorems provided here can be found in several references [43, 44], and are provided here for completeness.

2.1.2 Definitions

Definition 2.1.1 (Convex Set) *A set S in a vector space (over real numbers) X is said to be convex if for every $x_1, x_2 \in S$, and for every $t \in [0,1]$, $tx_1 + (1-t)x_2 \in S$.*

Definition 2.1.2 (Convex function) *A real valued function $f : S \to \mathbb{R}$ (where S is a convex set in a vector space X) is said to be a convex function if, for every $x_1, x_2 \in S$, and every $t \in [0,1]$, $f(tx_1 + (1-t)x_2) \leq tf(x_1) + (1-t)f(x_2)$.*

Definition 2.1.3 (Linear operators) *Let X and Y be vector spaces over a field K. A function $f : X \to Y$ is said to be a linear operator if:*

$$f(x_1 + x_2) = f(x_1) + f(x_2) \tag{2.1}$$

$$f(\alpha x) = \alpha f(x) \tag{2.2}$$

$\forall\, x_1,\ x_2,\ x \in X,\ \alpha \in K.$

Definition 2.1.4 (Bounded linear operators) *Consider two normed vector spaces X, and Y. A linear operator $f : X \to Y$ is said to be a bounded iff f is a continuous linear operator from X to Y. The induced norm of f is given by:*

$$\|f\| = \sup_{\substack{x \in X \\ x \neq 0}} \frac{\|f(x)\|_Y}{\|x\|_X}. \tag{2.3}$$

Definition 2.1.5 (Dual spaces) *The collection of all bounded linear functionals from a normed vector space X to $\mathbb{R}$ is denoted by X^* (also known as the dual space of X). Whenever a linear functional is represented by some element $x^* \in X^*$, $< x, x^* >$ denotes the linear functional evaluated at x.*

Definition 2.1.6 (Annihilator space) *Let S be a subset of a normed linear space X. The annihilator of S (denoted by $S^{\perp}$) is the set of elements x^* of the dual space of X such that $< x, x^* >= 0\ \forall\ x \in X$.*

Definition 2.1.7 (Alignment) *$x^* \in X^*$ and $x \in X$ are said to be aligned if $< x, x^* >= \|x\|\|x^*\|$.*

2.1.3 Theorems

Theorem 2.1.1 (Minimum distance) *Let x be an element in a normed linear space X, and let S be a subspace of X.*

$$\inf_{s \in S} \|x - s\| = \max_{a^* \in S^\perp} < x, a^* > \tag{2.4}$$

where the maximum is achived for some a_o^* with $\|a_o^*\| = 1$. If the infimum is achieved by some $s_o \in S$, then $x - s_o$ is aligned to a_o^*.

Theorem 2.1.2 (Existence) *Let X be a topological vector space, and f be a lower semi-continuous functional on X. If S is a compact subset of X, then $\inf_{x \in S} f(x)$ has a solution $x_o \in S$.*

While the requirement that S be compact might seem restrictive, a solution to the minimum distance problem can be shown to exist by proving that the subspace is $weak^*$ closed [44]. We use the result in theorem 2.1.1 for several vector space optimization problems (such as model matching problems) presented later in this chapter. These results are used in other chapters to illustrate fundamental performance limitations of systems.

Theorem 2.1.3 (Schur Complement) *Consider a symmetric matrix M, and the Schur complements of A and C (S_A and S_C respectively) given by:*

$$M = \begin{bmatrix} A & B \\ B^T & C \end{bmatrix}$$

$$S_A = C - B^T A^{-1} B$$

$$S_C = A - B C^{-1} B^T$$

Then we have the following conditions:

- $M > 0 \Leftrightarrow A > 0,\ S_A > 0$.
- $M > 0 \Leftrightarrow C > 0,\ S_C > 0$.
- *If* $A > 0$*, then* $M \geq 0 \Leftrightarrow S_A \geq 0$.
- *If* $C > 0$*, then* $M \geq 0 \Leftrightarrow S_C \geq 0$.

The Schur complement can be used to convert quadratic inequalities to LMIs using the conditions listed above.

2.2 Numerical optimization

2.2.1 Overview

In this dissertation we examine several optimization problems that are of interest to system and control design engineers. There are several important problems for which closed form (analytical) solutions do not exist, requiring numerical methods for finding a suitable solution.

While there are many interesting optimization problems in system and control theory for which there do not currently exist efficient optimization algorithms, this dissertation focuses on problems which can be solved efficiently. While this excludes several problems which are of interest in the design of control systems, the main objective of this work is on integrating control design ideas into the development of specifications and systems. Control design metrics for which computationally efficient solutions do not currently exist are difficult to integrate into the system and specification phase. Control metrics that

can be quickly computed, on the other hand, can help limit the specification or design space, simplifying the iterative nature of the specification-system-controller design process.

In the rest of this chapter, we consider several numerical approaches used in the rest of this dissertation. We first discuss convex optimization problems in Section 2.2.2, followed by a discussion of linear matrix inequalities (a specific type of convex optimization problems). Other numerical optimization problems used in this dissertation is discussed in section 2.2.4.

The material presented here can be found in several references: convex optimization [45], linear matrix inequalities [46], and bilinear matrix inequalities [47, 48]. The material presented here is by no means exhaustive, and only those concepts that are directly utilized in the dissertation are provided for completeness.

2.2.2 Convex Optimization

Convex optimization deals with the minimization of a convex function over a convex set as follows:

$$\min_{x \in X} f(x) \tag{2.5}$$

where X is a closed convex set, and f is a convex function. Instead of a convex set, a convex optimization is often formulated in terms of convex constraints as given below:

$$\min_{x} f(x) \tag{2.6a}$$

subject to

$$g_i(x) \leq 0 \tag{2.6b}$$

$$h_j(x) = 0 \tag{2.6c}$$

where $g_i(x)$ ($i = 1,\ 2,\ \ldots,\ m$) are convex functions, and $h_j(x)$ ($j = 1,\ 2,\ \ldots,\ n$) are affine functions. If the cost and constraint functionals are all linear, then the above optimization is a linear programming problem.

There are several methods to solve convex optimization problems. Some common approaches include [49] (1) interior-point methods, (2) cutting-plane methods, and (3) subgradient methods. Subgradient methods are easy to implement, and can handle non differentiable convex functions [50].

Some common optimization problems that are convex include:

- Linear programming.
- Quadratic programming.
- Semidefinite programming.
- Linear Matrix Inequalities.

Linear Matrix Inequalities are of special interest in the design of control systems, and are explored in greater detail next.

2.2.3 Linear Matrix Inequalities for Linear Systems

Several important problems in the design of control systems can be formulated as linear matrix inequalities (LMIs). LMIs are convex optimization problems, and several efficient algorithms for solving LMIs exist. Some common control problems that can be formulated as LMIs include: $\mathcal{H}^\infty$ minimization, finding holdable ellipsoids, computing regions of attractions, etc.

Linear Matrix Inequalities have the following general form:

$$S(x) = S_0 + \sum_{i=1}^{m} x_i S_i > 0 \tag{2.7}$$

where $S_i \in \mathbb{R}^{n\times n}$ ($i = 0, 1, \ldots, m$) are symmetric matrices, and $x \in \mathbb{R}^m$ is the variable. Since $S(x)$ is a symmetric matrix, some of the terms in the LMI expressions can be omitted (replaced with a $*$). In this dissertation, only the upper or lower triangular elements of the symmetric LMI matrices are shown. The difference between Equation (2.7) and a nonstrict version of it is addressed in [46].

We start by presenting the general state-space model for this class of systems, followed by the LMI expressions for different metrics.

LMI Models

Consider a linear plant described by the following state space expression:

$$\dot{x} = Ax + B_u u + B_w w \tag{2.8a}$$

$$z = C_z x + D_{zu} u + D_{zw} w \tag{2.8b}$$

where $x \in \mathbb{R}^{n_x}$ is the state vector, $u \in \mathbb{R}^{n_u}$ is the vector of control signals, and $w \in \mathbb{R}^{n_w}$ is the vector of disturbances. In this section we use a static full-state feedback control law $u = Kx$, where $K \in \mathbb{R}^{n_u \times n_x}$. In order to convexify the LMI expressions, we rewrite the control law as follows: $K = YQ^{-1}$ where $Y \in \mathbb{R}^{n_u \times n_x}$, and $Q \in \mathbb{R}^{n_x \times n_x}$ is a positive definite matrix.

Stability

The condition for the quadratic stability of the closed loop is given by the following expression:

$$AQ + QA^T + B_u Y + Y^T B_u^T < 0 \tag{2.9}$$

$\mathcal{H}^\infty$ norm

The $\mathcal{H}^\infty$ norm of the closed loop system (the $\mathcal{L}^2$ induced norm or energy gain from w to z) is less than γ ($\gamma > 0$) if [51]:

$$\begin{bmatrix} AQ + QA^T + B_u Y + Y^T B_u^T & * & * \\ B_w^T & -\gamma I & * \\ C_z Q + D_{z,u} Y & D_{z,w} & -\gamma I \end{bmatrix} < 0 \tag{2.10}$$

Constraints on the control input

Norm constraints on the input vector $u = Kx$ can be enforced by making use of concepts from holdable ellipsoids. Let us assume that x_o is the initial state of the system, and that there are no disturbances. Then the constraint $\|u(t)\| \leq \overline{u} \; \forall \; t > 0$ is enforced if the

following LMIs hold:

$$\begin{bmatrix} 1 & * \\ x_o & Q \end{bmatrix} \geq 0 \qquad \begin{bmatrix} Q & * \\ Y & \overline{u}^2 I \end{bmatrix} \geq 0 \quad (2.11)$$

A different constraint on the input can also be used: $\|u(t)\|_{max} \stackrel{\text{def}}{=} \max_i |u_i(t)|$. For this metric, the constraint on $\|u(t)\|_{max} \leq \overline{u} \, \forall \, t > 0$ is satisfied if the following LMIs hold:

$$\begin{bmatrix} 1 & * \\ x_o & Q \end{bmatrix} \geq 0 \qquad \begin{bmatrix} Q & * \\ Y & \overline{u}^2 I \end{bmatrix} \geq 0 \qquad X_{ii} \leq \overline{u}^2 \quad (2.12)$$

2.2.4 Polynomial Matrix Inequalities

Several important control problems cannot be formulated as LMIs. For example, static output feedback control [52] problems can be formulated as bilinear matrix inequality (BMI) optimizations. BMI problems, however, are often nonconvex (for example consider the simple BMI set described by the expression $1 - xy > 0$, as shown in figure 1).

While BMIs can describe a much larger class of problems, they are more computationally complex to solve as they are not convex (specifically, they are NP-hard problems [53]). In order to find a global optimum value a branch and bound approach can be used [47, 54] ([48] compares the performance of a branch and bound approach with an evolutionary algorithm for several common control metrics). PenBMI [55] is the solver used for solving BMI problems in this work.

These issues also arise in solving more complex matrix inequalities, such as polynomial matrix inequalities (PMIs). PMI problems (of which BMIs are a special case) are also

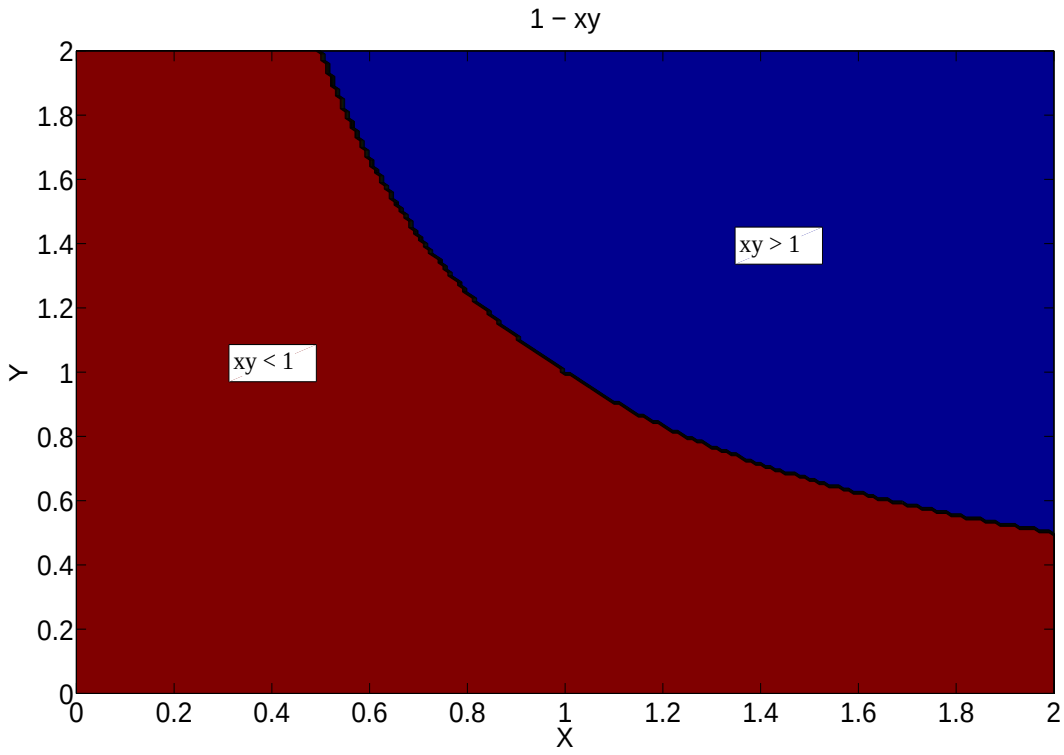

Figure 1: Bilinear Matrix Inequality 1-xy: Non-convex

non-convex in general, but in some cases SDP representations can be found to simplify the problem using LMIs in a lifted space [56]. A hierarchy of LMI relaxations to solve polynomial matrix inequalities is considered in [57].

In this work, both the plant and the controller are designed in an integrated framework. If the state space matrices A, B, C, or D are affine functions of a variable, the LMIs presented in Section 2.2.3 are now bilinear matrix inequalities. Such a problem formulation is considered in Chapter 3.

2.3 Limits of Performance

2.3.1 Overview

In this section, we examine several performance metrics that are of interest to control engineers. Some of these performance metrics are plant-centric (i.e. they can be computed without implicitly or explicitly designing a controller), while others require the design of stabilizing controllers. Examples of controller independent specifications include: computing the range of the plant (signal space), and null-controllability region estimation. Controller dependent specifications include computing the minimum achievable $\mathcal{H}^{\infty}$ performance (through LMIs).

The main objective (of considering performance limitations) is to include control metrics early in the system-design phase. If control limitations are incorporated early into the system/specification design process, we can: (1) design specifications that are more likely to be achievable, (2) design systems that are easier to control, and (3) reduce the number of specification-system-controller design iterations.

The focus is on metrics that can be quickly computed (and can therefore be easily incorporated into the vehicle design process); specifically, we consider metrics that can be computed analytically or can be formulated as a convex optimization problem (e.g. via Youla parameterization). In case we restrict controller to static full state-feedback control laws, several common control design problems can be formulated as Linear Matrix Inequalities (LMIs). An overview of convex optimization and LMIs (and related control design problems) can be found in section 2.2.

In the rest of this section we present several performance metrics (and how to compute them) that are of interest in the control-design phase. Where performance bounds can be computed, we present the limits of achievable performance as well. These metrics are broadly divided into two categories: (1) Frequency domain metrics, and (2) Time-domain metrics. The material presented in this section have appeared in several publications [9, 11].

2.3.2 Frequency Domain Metrics

Bode Integral

The Bode sensitivity integral for MIMO systems is determined by the location of the (N) unstable open loop poles [58]:

$$\sum_j \int_0^\infty \ln \sigma_j \left(S(j\omega)\right) d\omega = \pi \sum_{i=1}^{N} Re(p_i) \tag{2.13}$$

Since our plant is strongly stabilizable, a lower bound on the integral can be found using just the plant pole. In addition, the pole can be expressed in terms of the pitch rate stability derivative of the plant.

Sensitivity Bounds

We have the following relation for peak sensitivity and complementary sensitivity at the plant output: $\|S\|_\infty \geq c$, $\|T\|_\infty \geq c$, where

$$\phi = \arccos |y_z^H y_p| \tag{2.14}$$

$$c = \sqrt{\sin^2 \phi + \frac{|z+p|^2}{|z-p|^2} \cos^2 \phi} \tag{2.15}$$

where y_z is output directionality of the NMP zero, y_p is the output directionality of the RHP pole, and ϕ is the angle between them.

For a SISO plant with a single right-half plane zero z and right half plane pole p, the following holds [59]:

$$\int_0^\infty \ln|S(j\omega)| \quad \frac{2z}{z^2+\omega^2} \; d\omega \quad = \quad \pi \; \ln\left|\frac{p+z}{p-z}\right| \tag{2.16}$$

Additionally, we have the following bound on the impact of multiplicative output uncertainty E_O and input uncertainty E_I on the resulting sensitivity S':

$$\bar{\sigma}(S') \leq \bar{\sigma}(S)\bar{\sigma}((I+E_O T)^{-1}) \tag{2.17}$$

$$\bar{\sigma}(S') \leq \gamma(P)\bar{\sigma}(S)\bar{\sigma}((I+E_I T_I)^{-1}) \tag{2.18}$$

2.3.3 Time Domain Metrics

Plant Range

The range of the plant is the set of all signals achievable by a plant subject to input constraints. Input signal constraints include saturations, rate limitations, and stability requirements (i.e. the signal must stabilize the system).

Non-minimum phase zeros restrict the plant range irrespective of inputs constraints [44]. Feasibility of norm bounded trajectory specifications can be quickly verified using vector space or convex optimization techniques [43].

Input constraints can be handled using a finite basis to approximate the input. While continuous time optimal control ideas can be used, they often require stronger constraints

(such as differentiability) which are only applicable to some of the metrics. If we use an input basis, the L_1 and L_∞ optimization can be transformed into a finite dimensional linear program, while the L_2 norm minimization becomes a finite dimensional convex (quadratic) optimization problem.

Example 2.3.1 *Consider* $P_{toy,\,1} = \frac{p(z-s)}{z(s+p)}$*, and a trajectory* $Y = \frac{\tau}{s(s+\tau)}$*. Table 2.1 shows the minimum output error achievable (in absence of input constraints).*

Norm	Minimum error (norm)	Minimum error (signal)	Optimal Input (signal)
L_1	$\frac{\tau}{z(z+\tau)}$	$\frac{\tau}{z(z+\tau)}$	$\frac{\tau^2(s+p)(s+z+\tau)}{p(z+\tau)s(s+\tau)}$
L_∞	$\frac{\tau}{z+\tau}$	$\frac{\tau}{zs(z+\tau)}$	$\frac{z\tau(s+p)}{ps(s+\tau)}$

Table 2.1: Limit of tracking accuracy for $P_{toy,\,1}$

L_2 error minimization results in finite L_1 and L_∞ norm errors. The L_1 error minimizer has an impulse, and the L_∞ optimization results in non-zero steady state error (it is possible to get arbitrarily close to the optimal L_∞ norm error with zero steady state error [60]).

Figure 2 illustrates the minimum pole location required to meet various (lower) saturation constraints based on the plant zero and desired settling time. The sign of the lower saturation bound is assumed to be negative.

From Table 2.1 and Figure 2:

- The optimal control signals are stable (i.e. the NMP zero is not canceled).
- The control signal must cancel the RHP pole - an internally stabilizing feedback controller achieves this.

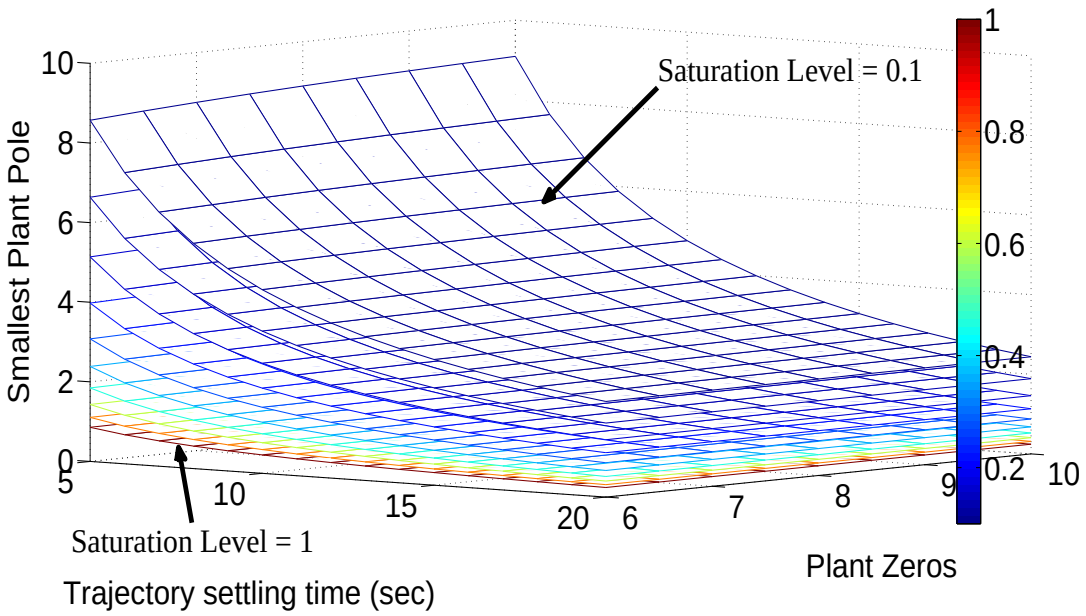

Figure 2: Variation in peak undershoot for optimal control signal

- Smaller plant instabilities result in greater control undershoot.

This analysis suggests that greater instability is desirable to reduce undershoot in the controls; some drawbacks of large instabilities include frequency domain waterbed effects, smaller null controllability regions, etc. The null controllability region is examined next.

Null-Controllability Region

The Null-Controllability Region (NCR) represents a fundamental performance limitation of unstable systems with actuator saturation constraints[61].

Definition 2.3.1 (Null-Controllability Region) *A state x_o is said to be null controllable if there exists a $T \in [0, \infty)$ and an admissible control u such that the state trajectory of the*

system satisfies $x(0) = x_o$ and $x(T) = 0$. The set of all null controllable states is called the null controllability region of the system.

We assume that the control saturation bounds are closed, convex, and include the origin. The NCR is nonempty (it contains the origin). For stable systems, the entire space is in the NCR. For unstable systems with finite saturation bounds, the NCR is not the entire space [62].

Example 2.3.2 *Consider the plant $P_{toy,\,2} = \frac{1}{s-1}$. A state space representation is $\dot{x} = x + u$. Let the input saturation bounds be ± 1. The NCR is $-1 \leq x \leq 1$.*

However, tracking a command $x = 1$ might be unachievable for the example above (modeling errors affecting DC gain), or the system might be pushed out of the NC region (due to disturbances). The NCR computation has been examined for continuous/discrete systems (with input and state constraints) [63]. In this chapter, a saturation constraint is also included in the formulation. Clearly, the null controllability region is bounded only along the direction of the anti-stable modes (since any excitation of the stable modes would decay without any control action).

Let our system be described by the state space representation $(A, b, C, 0)$, and have only one unstable mode. If we have a symmetric saturation bound on our system of $\pm\bar{u}$, then the limit of the null controllability region along q can be expressed as:

$$\lambda = \frac{\|p * b\|}{\|p * q\|}\bar{u} \tag{2.19}$$

where p and q are the left and right eigenvectors of A associated with this unstable mode. If the system reaches a state whose component along q is greater than λ, then the system

will go unstable.

Computing the NCR for non-symmetric saturation bounds is explored in [61]. For multi-input systems, the NC sets of each input considered independently and combined [61, 64].

We observe the following from equation (2.19):

- The larger the instability (keeping the directionality constant), the smaller the NCR.
- The smaller the saturation bound, the smaller the NCR.
- If the system enters a state outside the NCR, its trajectory will be unstable.

The directionality of the trajectory and trajectory-robustness (as related to the NCR) is examined next.

The NCR is limited in the direction of the unstable right-eigenvector. It is desirable to maximize the gap between the vehicle trajectory from the NC boundary due to disturbance robustness, and stickiness [61]. The vehicle can be designed to maximize the trajectory-boundary gap.

Example 2.3.3 *Consider two plants $P_{toy,3}$ and $P_{toy,4}$, whose state space representations are given below:*

$$P_{toy,3} = \left(\begin{bmatrix} 1 & 1 \\ 0 & -1 \end{bmatrix}, \begin{bmatrix} 1 \\ 1 \end{bmatrix}, \begin{bmatrix} 1 & 0 \end{bmatrix}, 0 \right) \tag{2.20}$$

$$P_{toy,4} = \left(\begin{bmatrix} 1 & 1 \\ 0 & -0.9 \end{bmatrix}, \begin{bmatrix} 1 \\ 1 \end{bmatrix}, \begin{bmatrix} 1 & 0 \end{bmatrix}, 0 \right) \tag{2.21}$$

Both plans have the same unstable right-eigenvector $[1,\ 0]^T$, and are assumed to have the same input saturation bound (± 0.5). The desired trajectory has a steady state output of 1. In the absence of disturbances, both plants can achieve the desired output. The NCR region for each plant is given by:

$$S_{NC,3} = Co \left\{ \begin{bmatrix} 0.75 \\ 0 \end{bmatrix}, \begin{bmatrix} -0.75 \\ 0 \end{bmatrix} \right\} \cup span \left\{ \begin{bmatrix} -0.4472 \\ 0.8944 \end{bmatrix} \right\} \tag{2.22}$$

$$S_{NC,4} = Co \left\{ \begin{bmatrix} 0.763 \\ 0 \end{bmatrix}, \begin{bmatrix} -0.763 \\ 0 \end{bmatrix} \right\} \cup span \left\{ \begin{bmatrix} -0.4657 \\ 0.8849 \end{bmatrix} \right\} \tag{2.23}$$

where Co denotes the convex hull of the vectors.

Based on steady state analysis, the terminal conditions are:

$$u_{ss,3} = -0.5, \qquad x_{ss,3} = \begin{bmatrix} 1 \\ -0.5 \end{bmatrix}, \qquad g_{ss,3} = 0.75 \tag{2.24}$$

$$u_{ss,4} = -0.4737, \qquad x_{ss,3} = \begin{bmatrix} 1 \\ -0.5263 \end{bmatrix}, \qquad g_{ss,4} = 0.7230 \tag{2.25}$$

$g_{ss,i}$ denotes the component of the steady-state vector along the unstable mode for the i^{th} plant.

We observe the following:

- $P_{toy,3}$ has no control margin for uncertainty.
- $P_{toy,3}$ has a smaller state disturbance rejection margin ("closer" to its NCR boundary).

The above example only considered the steady state - a complete approach must consider the distance of the entire trajectory from the NCR boundary. Additionally, the minimum gap at steady state must be computed over all states that have the desired output.

The robustness analysis is performed for a specific state space representation. In general, linear plants can be expressed in several equivalent forms. Under an invertible linear transformation $\hat{x} = Sx$, a state x_o is null-controllable (for the original state space model) iff $\hat{x_o} = Sx_o$ is null-controllable using the transformed state space model i.e. the NCR undergoes the same transformation as the states, and state disturbances. However, any metric on the robustness of the trajectory must be invariant to state/control transformations.

Robust Null-Controllability Region

The above definition of NCR only requires the existence of a admissible control signal to bring the system to the origin. However, the control signal might have discontinuities that are not realizable by an actual controller. To address this issue, we can restrict our attention

to control signals that come from a state feedback controller. An additional drawback is that the NCR does not have a notion of robust states. To address this, we define a new region called the Robust Null Controllability Region (RNCR) informally below.

Definition 2.3.2 (Robust Null-Controllability Region) *A state x_o is said to be in the Robust Null-Controllability Region if there exists a "robust controller K such that the resulting control signal is admissible and the state trajectory follows the following boundary conditions: $x(0) = x_o$, and $\lim_{t\to\infty} x(t) = 0$.*

The exact specifications of a robust controller depends on the system designer. Due to the difficulties in addressing the existence of such a robust controller, we limit our attention to state-feedback controllers (which can be found via LMIs). The RNCR is the union of all regions of attraction over all robust controllers.

The size of the (Robust) Null-Controllability region (along the unstable eigenvector direction p) under a state-feedback law is given by the following optimization (excluding stability constraints from Equation (2.9)):

$$\max_{Q,Y,\lambda} \lambda \quad \text{subject to} \tag{2.26}$$

$$\begin{aligned} Q &> 0 \\ \lambda &> 0 \\ \begin{bmatrix} 1 & \lambda p^T \\ \lambda p & Q \end{bmatrix} &\geq 0 \end{aligned} \tag{2.27}$$

It should be noted that while the NCR is not limited along stable eigenvector directions, the state-feedback NCR conditions can be violated by moving too far along stable eigenvectors (due to a violation of Equation (2.27)).

The RNCR (computed using state-feedback) has the following advantages:

- Easy to compute using LMIs.
- Guarantees the existence of robust controllers to stabilize the system.

We also have the following ordering of the above regions:

$$\text{RNCR (using state feedback)} \subset \text{NCR (using state feedback)} \subset \text{NCR}$$

2.4 Summary

In this chapter we presented several mathematical results that will be used in the rest of this dissertation. Several common control design problems were formulated as convex optimization problems using Linear Matrix Inequalities. These LMIs (and similar BMI problems) are revisited throughout this dissertation, as they are of interest to control system designers.

Fundamental performance metrics (such as lowest tracking error achievable, smallest peak sensitivity, and null-controllability regions) were also examined. While these results presented in this chapter are optimistic (i.e. they neglect certain 'real-world limitations), they can be quickly computed and thus represent an important tool in evaluating system designs.

The metrics presented in this chapter are used in the integrated design framework considered in the next chapter.

3

INTEGRATED DESIGN AND CONTROL OF DYNAMICAL SYSTEMS

3.1 Overview

In this chapter we present the main focus of this dissertation: a multidisciplinary optimization framework to integrate system and control design metrics using BMIs (Algorithm 1 presents the pseudocode for the algorithm). In later chapters we shall examine the computation time associated with finding equilibriums and linearizing models from nonlinear differential equations (see Table 4.5 for a quick summary). Due to the high computation cost associated with evaluating different designs, we use approximations to reduce the number of exact function evaluations required.

Any algorithm used for multidisciplinary optimization must be capable of including system and control constraints - the methodology presented in this chapter can handle multivariate polynomial constraints (representing system design constraints), as well as control constraints that are traditionally formulated using linear matrix inequalities. This is done by using affine approximations for the plant model, and BMI solvers for numerical optimization.

The rest of this chapter is organized as follows: a framework to perform integrated system and control design is presented in Section 3.2, followed by a discussion of its capabilities and limitations. Section 3.3 summarizes the work done in this chapter.

3.2 Integrated System-Controller Design

In this section we examine an integrated system-controller design problem. We present a description of the system and the controller, follow by the formulation of the exact problem. Due to the complexity involved in solving the exact problem, we solve an approximation to the original problem using bilinear matrix inequalities (a discussion on LMIs and BMIs can be found in Section 2.2). By iteratively restricting the search space and improving the approximation, we attempt to solve the system-control design problem.

Multidisciplinary optimization can be computationally complex, with non-convex objectives and constraints that can be expensive to evaluate. In order to improve the computation time required, we approximate the plant using an affine model, and constraints are approximated by multivariate polynomials. Once a design for the approximate problem is found, the exact plant (at the ‘optimal design parameters) is computed. If the exact system satisfies the design requirements, a feasible solution has been found. If it is not feasible, we use the new model to improve the approximations and repeat the optimization. This procedure is repeated till we get a feasible solution, or no feasible solution is believed to exist (i.e. some termination condition is satisfied).

This algorithm is used in later chapters in order to improve the vehicle design procedure for an air-breathing hypersonic vehicle. Since the initial objective is to obtain a set of feasible designs (rather than an optimal design - which can involve metrics that are hard to quantify), the optimization problems are formulated as tests for feasibility. They can be easily modified to optimize a particular objective function, if desired.

3.2.1 System Description

Consider a nonlinear system described by the following differential equations in the standard state-space form:

$$\dot{x} = A(p(t), \rho(t))x(t) + B_u(p(t), \rho(t))u(t) + B_w(p(t), \rho(t))w(t) \tag{3.1}$$

$$z(t) = C_z(p(t), \rho(t))x(t) + D_{z,u}(p(t), \rho(t))u(t) + D_{z,w}(p(t), \rho(t))w(t) \tag{3.2}$$

where t denotes time, $x \in \mathbb{R}^{N_s}$ is the vector of states (N_s is the number of states), $u \in \mathbb{R}^{N_u}$ is the vector of N_u control signals, $w \in \mathbb{R}^{N_w}$ denotes the vector of N_w exogenous inputs (such as reference commands, disturbances, etc). $A,\ B_*,\ C_*,\ D_*$ are the state space matrices, ρ is a vector denoting the operating conditions, and p is the vector of design parameters (of dimension N_p). z are the performance signals of interest. We also assume that Θ denotes the operating conditions of interest (i.e. $\rho(t) \in \Theta\ \forall t \in [0, \infty)$), and $\Phi \subset \mathbb{R}^{N_p}$ denotes the set of all acceptable plant parameters.

The constraint set Φ can be specified explicitly (such as a bounding box for the set of acceptable designs) and/or through constraint equations. When the design parameters lie in a closed convex polytope, the constraints on the plant parameters can be expressed as a linear inequalities (intersection of half-spaces) [65].

While there are infinitely many possible operating points, we sample the space to get a finite set of operating conditions i.e. $\rho \in [\rho_1,\ \rho_2,\ \ldots,\ \rho_{N_\rho}]$, where N_ρ is the number of operating point samples. We refer to the set of sample points as $\mathcal{S}_\rho$

In this dissertation, we use an affine approximation for the state space model of the plant as shown here:

$$A_j(p) \stackrel{\text{def}}{=} A_{j,0} + \sum_{i=1}^{N_p} A_{j,i} p_i \tag{3.3}$$

$$B_{u,j}(p) \stackrel{\text{def}}{=} B_{u,j,0} + \sum_{i=1}^{N_p} B_{u,j,i} p_i \tag{3.4}$$

$$B_{w,j}(p) \stackrel{\text{def}}{=} B_{w,j,0} + \sum_{i=1}^{N_p} B_{w,j,i} p_i \tag{3.5}$$

$$\dot{x}_j = A_j(p) x_j(t) + B_{u,j}(p) u(t) + B_{w,j}(p) w(t) \tag{3.6}$$

$$z_j(t) = C_z x_j(t) + D_{z,u} u(t) + D_{z,w} w(t) \tag{3.7}$$

where N_p is the number of plant parameters, and $j \in [1,\ 2,\ \ldots,\ N_\rho]$ is an index for the operating point. Therefore, we consider one affine model for the plant at each operating point.

We make the following assumptions about the system:

Assumption 3.2.1 (Controllability and Observability) *We assume that the system is observable and controllable for all operating conditions of interest, and all vehicle designs being considered.*

Assumption 3.2.2 (Dimensions of the System) *We assume that the dimensions of the linearized system does not change based on the operating conditions.*

3.2.2 Controller Description

Since this is a preliminary design phase, where we are interested in computing the limits of performance, we use a static full-state feedback control law. Such a control law assumes that all states are measurable (in practice, some states might be estimated using an observer, which requires the system to be observable). For a single plant staying 'close' to one

operating point, we parameterize the control law as follows:

$$u = Kx \tag{3.8}$$

$$= YQ^{-1} \tag{3.9}$$

$$Q \geq 0 \tag{3.10}$$

where $u \in \mathbb{R}^{N_u}$ is the control vector, $x \in \mathbb{R}^{N_s}$ is the state vector, $K \in \mathbb{R}^{N_u \times N_s}$ is the static control law parameterized by $K = YQ^{-1}$, $Q \in \mathbb{R}^{N_s \times N_s}$ is a positive definite matrix.

In Section 2.2.3 several controller design problems were presented as LMIs. These design problems involved the state-space matrices of the plant, and hence depend on the system design parameter p, and the operating condition ρ. However, we are not interested in finding a control law for every possible design parameter p, but only for the final/optimal design parameter p^*.

For a plant specified by a design vector p, the control law depends on the operating point ρ. The nonlinear control law is given by $K_p(\rho) : \Theta \rightarrow \mathbb{R}^{N_u \times N_s}$. Since the plant is approximated as an affine function of the plant parameter at a set of fixed operating points (see equation (3.3) above), we design the controller at the same operating points as well; instead of obtaining a nonlinear control law $K(\rho)$ directly, we compute one controller for each sample operating point $K_{p,\rho_j},\ j \in [1,\ 2,\ \ldots,\ N_\rho]$ and schedule the controller to obtain a nonlinear control law. Several methods for interpolating controllers between the operating points have been discussed in [66].

While the parameterization of the controllers (in terms of Y and Q) allows us to formulate common control constraints as BMIs, the computational complexity of the problem is not reduced (BMIs are NP-hard - see Section 2.2.4). However, a non-parameterized controller would result in the control metrics being Polynomial Matrix Inequalities (PMIs) of order at least three. While PMIs can be reduced to BMIs with augmented variables and equality constraints, this would increase the dimensionality of the problem significantly.

By parameterizing the controller, however, we cannot manipulate the structure of the controller directly. Additional constraints are needed to limit the control design to a decentralized architecture, for example.

3.2.3 Exact Problem Formulation

The general integrated system-control design problem addressed in this dissertation can be formulated as given below:

$$\min_{p, K_p(\rho)} 1 \tag{3.11a}$$

subject to

$$G(p, \rho, K_p(\rho), P(p, \rho)) \leq 0 \tag{3.11b}$$

where p is the design parameter vector, $K_p(\rho)$ is a operating point dependent control law, $P(p, \rho)$ is the nonlinear plant model that depends on the design parameters and operating condition, and G is the constraint equations.

3.2.4 Approximate Problem Formulation

The exact problem formulation above can be quite difficult to solve. The plant, controller, and constraints can be nonlinear functions of the plant parameterization and operating points. As a first step, we approximate the plant and constraints at the chosen operating points in order to simplify the problem.

Based on the approximations to the plant in Equation (3.3), the problem described in Equation (3.11) can be modified as follows:

$$\min_{p, K_{p,j}} 1 \tag{3.12a}$$

subject to

$$\hat{G}_j(p, K_{p,j}, \hat{P}_j(p)) \leq 0 \tag{3.12b}$$

where $j \in [1, 2, \ldots, N_\rho]$, $\hat{P}_j$ denotes the affine approximation to the state space representation of the plant at operating point ρ_j, and $\hat{G}_j$ is an approximation to the constraint G at the operating point ρ_j. Clearly, we have one approximation for P at each operating point; however, the parameter p is the same across all operating points.

The cost and constraint functions can include both control-relevant metrics as well as system design metrics. In this dissertation, we use BMIs and multivariate polynomials to approximate $\hat{G}_{\rho_j}$. Using a BMI solver, we attempt to solve the approximate optimization problem (and compare the result with other solvers). This solution to an approximate optimization problem forms the core of the iterative optimization approach.

Some common control constraints can be formulated as LMIs (using the parameterization in Equation (3.8)) as shown in Section 2.2.3. However, since the state space matrices for the plants are approximated as affine functions of the parameters (as in Equation (3.3)), the control constraints are now BMIs (see Section 2.2.4).

3.2.5 Iterative Solution

In order to obtain a solution to the exact problem in Equation (3.11), we solve a series of approximate optimization problems (described by Equation 3.12) in an iterative process, as described below in Algorithm 1. The following notation is used:

- $\mathcal{S}_\rho$: The set of sample points of the operating space Θ.
- p: $\mathbb{R}^{N_p}$ vector parameterization of the plant
- Φ: The set of acceptable plant designs, $\Phi \subset \mathbb{R}^{N_p}$.
- Ω_0: A N dimensional simplex; $\Omega_0 \subset \Phi$.
- $\mathcal{S}_\rho$: Set of N_ρ operating point samples.
- $P(p, \rho)$: Nonlinear plant.
- $\hat{P}(p, \mathcal{S}_\rho)$: Approximation to the plant P.
- $G(p, \rho)$: Inequality constraint (denoted by G for brevity).
- $\hat{G}(p, \mathcal{S}_\rho, \hat{\mathcal{P}})$: Approximation to G in a restricted set (denoted by $\hat{G}$ for brevity).
- ϵ: Branching termination criteria.
- Q: A queue of simplices still to be evaluated.

Algorithm 1 Iterative Multidisciplinary Optimization: Feasibility

Require: $\mathcal{S}_\rho$, Ω_0, G, $P(p, \rho)$, ϵ

1: $Q \leftarrow \Omega_0$ ▷ Q: queue of simplexes
2: **while** Q is not empty **do**
3: Pick $\mathbb{P}$ (vertices $V_{\mathbb{P},i}$) from Q ($i \in [1, \ \ldots, \ N_p + 1]$)
4: Obtain approximations $\hat{G}$, $\hat{P}$ using values at $V_{\mathbb{P},i}$
5: Find $p^* \in int(\mathbb{P})$ such that $\hat{G}(p^*) < 0$ ▷ Solve approximate problem feasibility
6: **if** p^* exists **then**
7: **if** $G(p^*) \leq 0$ **then** ▷ Test feasibility for exact problem
8: Clear Q, **return** p^* ▷ Feasible solution found
9: **else**
10: **if** $size(\mathbb{P}) < \epsilon$ **then**
11: **continue** with Q ▷ Polytope too small, don't branch further
12: **end if**
13: **end if**
14: **else** ▷ Approximate problem not feasible
15: **if** $size(\mathbb{P}) < \epsilon$ **then**
16: **continue** with Q ▷ Polytope too small, don't branch further
17: **else**
18: Set $p^* = centroid(\mathbb{P})$ ▷ Polytope large, branch
19: **end if**
20: **end if**
21: Split up $\mathbb{P}$ into sub-simplexes using p^* as a fixed vertex of all sub-simplexes.
22: Push each sub-simplex into Q
23: **end while**

The use of a queue in Algorithm 1 makes the algorithm a breadth first search (BFS) type of algorithm. If we wish to use a depth-first-search algorithm, a stack can be used instead. Alternatively, the elements of the list of simplexes to evaluate can be reordered based on a ranking function (such as 'distance' to feasibility) to improve the speed of the algorithm.

Tthe approximate feasibility problem (Line 5 of Algorithm 1) can be solved using several optimization algorithms. In this dissertation, we can express the constraints as BMIs and multivariate polynomials; these problems can be addressed using a BMI solver. Alternatively, we can use a pattern search or direct search based algorithm, or using a

(approximate) gradient based approach (such as NPSOL); in both cases, the approximate constraint evaluations are fast, since the controller design problem is an LMI (for a given plant configuration, the controller design problem is an LMI).

3.2.6 Properties

We shall now examine the advantages and limitations of Algorithm 1. Some of the advantages of the algorithm include:

Initialization : The algorithm does not require the initial vertices of the polytope to be feasible.

Parallelization : The algorithm can easily be parallelized since the optimization on each element in the queue is independent.

The algorithm has several limitations, however, as listed below:

Complexity : In each iteration of the algorithm, a BMI problem (NP-hard) must be solved. While efficient branch-and-bound techniques exist, such problems are hard to solve.

Controller Structure : The parameterization of the controller prevents us from directly imposing structure on the control law.

Problem size : Since we parameterize the controller, the problem size grows non-linearly (at least quadratic) with the model size.

Two approaches to improve the spped of the algorithm are: (1) the termination factor ϵ can be increased (at the cost of accuracy of the solution), (2) if a non-feasible p^* is too close to the existing vertices of the polytope, it can be moved to the centroid of the polytope.

3.3 Summary

In this chapter we considered a multidisciplinary optimization capable of handling system, specification, and control metrics. Such problems are often computationally expensive; we would like to reduce the number of function evaluations required to compute feasible designs. This is achieved through approximating the objective and constraints

In later chapters, we consider the design of air-breathing hypersonic vehicles. We examine the impact different vehicle configurations have on the static and dynamic properties of the vehicle. The results of the trade studies are used in the multidisciplinary optimization framework to include metrics of interest to control and aerospace designers while designing the vehicle.

4

MODELING OF AIR-BREATHING HYPERSONIC VEHICLES.

4.1 Overview

In this chapter, we examine the model of a 3-DoF air-breathing hypersonic vehicle. A nonlinear model is presented, and the impact of certain modeling assumptions (specifically with regards to the vehicle exhaust plume) are examined. An alternative approach to computing pressures in the plume is presented, and the numerical properties are evaluated. The model is used in the next chapter to design controllers and examine the limits of performance.

Since the historic 2004 scramjet-powered Mach 7 and 10 flights of the X-43A [67–70] , hypersonics research has seen a resurgence. Air-breathing hypersonic propulsion is viewed as the next critical step toward achieving (1) reliable, affordable, routine access to space, as well as (2) global reach vehicles. There are commercial and as military implications to both objectives. Rocket-based (combined cycle) propulsion systems [71] are much more expensive to operate because they must carry oxygen. This is particularly costly when traveling at lower altitudes through the troposphere (i.e. below 36,152 ft). They do not exhibit the desired levels of reliability and flexibility (e.g. airplane like takeoff and landing options) either. As a result, much emphasis has been placed on two-stage-to-orbit (TSTO) designs that involve a turbo-ram-scramjet combined cycle first stage and a rocket second stage. This research focuses on control challenges associated with scramjet-powered hypersonic vehicles [71–76].

There main modeling contributions of this dissertation are:

- Engine: The original engine dimensions were inconsistent with the mold line of the vehicle. We rectify this mismatch by changing the nozzle and diffuser area ratios.
- Plume: We develop an algorithm to compute the pressures in the vehicle exhaust (plume) to bring it closer to results obtained from a numerical procedure, while still significantly improving computation time.
- Plume Impact: We also examine the impact of the plume on the vehicle design and control algorithm, in order to highlight the need for accurate plume modeling.

In Section 4.2, we examine a first principles-based model of the hypersonic vehicle, and discuss the trimming and linearization of the model in Section 4.3. An alternative to the conventional plume model is examined in section 4.4, where a speed-fidelity trade-off is examined. Section 4.5 investigates the importance of the accuracy of the plume model on the system and controller design problems through simple examples.

4.2 Description of Nonlinear Model

In this section, we consider a first principles nonlinear 3-DOF dynamical model for the longitudinal dynamics of a generic scramjet-powered hypersonic vehicle [72, 73, 77–87]. The vehicle is 100 ft long with weight (density) 6,139 lb per foot of depth and has a bending mode at about 20 rad/sec. The controls include: elevator, stoichiometrically normalized fuel equivalency ratio (FER), diffuser area ratio (not considered in our work), and a canard (not considered in our work). The vehicle may be visualized as shown in Figure 3 [77, 88].

Modeling Approach. The following summarizes the modeling approach that has been used.

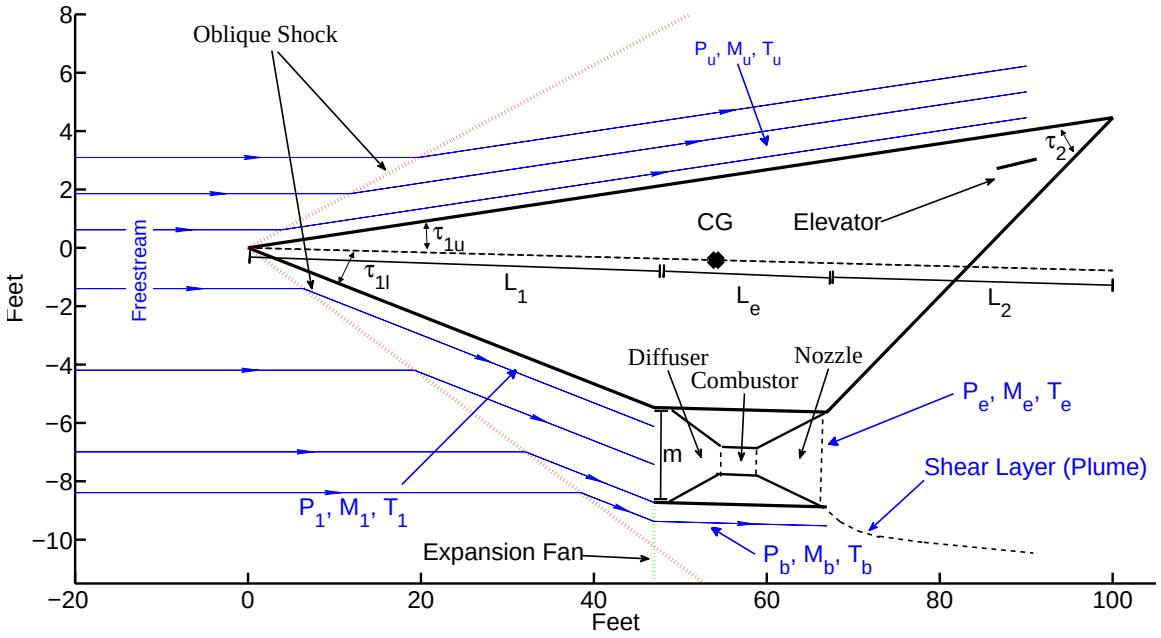

Figure 3: Schematic of Hypersonic Scramjet Vehicle

- *Aerodynamics.* Pressure distributions are computed using inviscid compressible oblique-shock and Prandtl-Meyer expansion theory [74, 87, 89, 90]. Air is assumed to be calorically perfect; i.e. constant specific heats and specific heat ratio $\gamma \stackrel{\text{def}}{=} \frac{c_p}{c_v} = 1.4$ [74, 89]. A standard atmosphere is used to calculate freestream properties [88].

  Viscous drag effects (i.e. an analytical skin friction model) are captured using Eckerts temperature reference method [74, 77]. This relies on using the incompressible turbulent skin friction coefficient formula for a flat plate. Of central importance to this method is the so-called wall temperature used. The model assumes a nominal wall temperature of $2500^\circ R$ [77].

  Unsteady effects (e.g. due to rotation and flexing) are captured using linear piston theory [77, 91]. The idea here is that flow velocities induce pressures just as the

pressure exerted by a piston on a fluid induces a velocity.

- *Propulsion.* A single (long) forebody compression ramp provides conditions to the rear-shifted scramjet inlet. The inlet is a variable geometry inlet (variable geometry is not exploited in our work). The model assumes the presence of an (infinitely fast) cowl door which uses AOA to achieve shock-on-lip conditions (assuming no forebody flexing). Forebody flexing, however, results in air mass flow spillage [87]. At the design cruise condition, the bow shock impinges on the engine inlet (assuming no flexing). At speeds below the design-flight condition and/or larger flow turning angles, the cowl moves forward to capture the shock. At larger speeds and/or smaller flow turning angles, the bow shock is swallowed by the engine. In either case, there is a shock reflected from the cowl or within the inlet (i.e. we have a bow shock reflection). This reflected shock further slows down the flow and steers it into the engine. It should be noted that shock-shock interactions are not modeled [88].

  The model uses liquid hydrogen (LH2) as the fuel. It is assumed that fuel mass flow is negligible compared to the air mass flow. Thrust is linearly related to FER for all expected FER values. For large FER values, the thrust levels off. In practice, when FER > 1, the result is decreased thrust. This phenomena [87] is not captured in the model. As such, control designs based on this nonlinear model (or derived linear models) should try to maintain FER below unity.

  The model also captures thermal choking. A (state dependent) saturation level - associated with FER (e.g. thermal choking and unity FER) - and a useful FER

margin definition (one that can be used for the design of control systems for scramjet-powered hypersonic vehicles) was addressed in [3]. Finally, it should be noted that the model offers the capability for addressing linear fuel depletion.

- *Structural.* A single free-free Euler-Bernoulli beam partial differential equation (infinite dimensional pde) model is used to capture vehicle elasticity. As such, out-of-plane loading, torsion, and Timoshenko effects are neglected. The assumed modes method (based on a global basis) is used to obtain natural frequencies, mode shapes, and finite-dimensional approximants. This results in a model whereby the rigid body dynamics influence the flexible dynamics through generalized forces. Within the current model, forebody deflections influence the rigid body dynamics via the bow shock which influences engine inlet conditions, thrust, lift, drag, and moment [83]. Aftbody deflections influence the AOA seen by the elevator. As such, flexible modes influence the rigid body dynamics.

- *Actuator Dynamics.* Simple first order actuator models (contained within the original model) were used in each of the control channels: elevator - $\frac{20}{s+20}$, FER - $\frac{10}{s+10}$, canard - $\frac{20}{s+20}$ (Note: canard not used in our study). Elevator position and rate saturation become very important given the vehicle's (open loop) unstable dynamics [88].

Generally speaking, the vehicle exhibits unstable non-minimum phase dynamics with nonlinear aero-elastic-propulsion coupling and critical (state dependent) FER constraints.

The model contains 11 states: 5 rigid body states (speed, pitch, pitch rate, AOA, altitude) and 6 flexible states.

Unmodeled Phenomena/Effects. All models possess fundamental limitations. Realizing model limitations is crucial in order to avoid model misuse. Given this, we now provide a (somewhat lengthy) list of phenomena/effects that are not captured within the above nonlinear model. (For reference purposes, flow physics effects and modeling requirements for the X-43A are summarized within [92].)

- *Dynamics.* The above model does not capture longitudinal-lateral coupling and dynamics [93] and the associated 6DOF effects.

- *Aerodynamics.* Aerodynamic phenomena/effects not captured in the model include the following: boundary layer growth, displacement thickness, viscous interaction, entropy and vorticity effects, laminar versus turbulent flow, flow separation, high temperature and real gas effects (e.g. caloric imperfection, electronic excitation, thermal imperfection, chemical reactions such as 0_2 dissociation) [74], non-standard atmosphere (e.g. troposphere, stratosphere), unsteady atmospheric effects [94], 3D effects, aerodynamic load limits. Many of these effects will be most severe along the aftbody of the vehicle [88].

- *Propulsion.* Propulsion phenomena/effects not captured in the model include the following: cowl door dynamics, multiple forebody compression ramps (e.g. three on X-43A [95, 96]), forebody boundary layer transition and turbulent flow to inlet [95, 96], diffuser losses, shock interactions, internal shock effects, diffuser-combustor interactions, fuel injection and mixing, flame holding, engine ignition via pyrophoric silane [69] (requires finite-rate chemistry; cannot be predicted via equilibrium methods [97], finite-rate chemistry and the associated thrust-AOA-Mach-FER sensitivity

effects [98], internal and external nozzle losses, thermal choking induced phenomena (2D and 3D) and unstart, exhaust plume characteristics, cowl door dynamics, combined cycle issues [71].

Within [98], a higher fidelity propulsion model is presented which addresses internal shock effects, diffuser-combustor interaction, finite-rate chemistry and the associated thrust-AOA-Mach-FER sensitivity effects. While the nominal Rayleigh-based model (considered here) exhibits increasing thrust-AOA sensitivity with increasing AOA, the more complex model in [98] exhibits reduced thrust-AOA sensitivity with increasing AOA - a behavior attributed to finite-chemistry effects. Future work will examine the impact of internal engine losses, and high temperature gas effect.

- *Structures.* Structural phenomena/effects not captured in the model include the following: out of plane and torsional effects, internal structural layout, unsteady thermoelastic heating effects, aerodynamic heating due to shock impingement, distinct material properties [99], and aero-servo-elasticity [100, 101].

  – *Heating-Flexibility Issues.* Finally, it should be noted that Bolender and Doman have addressed a variety of effects in their publications. For example, within [73, 83] the authors address the impact of heating on (longitudinal) structural mode frequencies and mode shapes. Comprehensive heating-mass-flexibility-control studies will be examined further in a subsequent publication.

It should be emphasized that the above list is only a partial list. If one needs fidelity at high Mach numbers, then many other phenomena become important; e.g. O_2 dissociation [74].

Longitudinal Dynamics. The equations of motion for the 3DOF flexible vehicle are given as follows:

$$\dot{v} = \left[\frac{T\cos\alpha - D}{m}\right] - g\sin\gamma \tag{4.1a}$$

$$\dot{\gamma} = \left[\frac{L + T\sin\alpha}{mv}\right] - \left[\frac{g}{v} - \frac{v}{R_E + h}\right]\cos\gamma \tag{4.1b}$$

$$\dot{q} = \frac{\mathcal{M}}{I_{yy}} \tag{4.1c}$$

$$\dot{h} = v\sin\gamma \tag{4.1d}$$

$$\dot{\theta} = q \tag{4.1e}$$

$$\ddot{\eta}_i = -2\zeta\omega_i\dot{\eta}_i - \omega_i^2\eta_i + N_i \qquad i = 1, 2, 3 \tag{4.1f}$$

$$\alpha \stackrel{\text{def}}{=} \theta - \gamma \tag{4.1g}$$

$$g = g_0\left[\frac{R_E}{R_E + h}\right]^2 \tag{4.1h}$$

where L denotes lift, T denotes engine thrust, D denotes drag, $\mathcal{M}$ is the pitching moment, N_i denotes generalized forces, ζ demotes flexible mode damping factor, ω_i denotes flexible mode undamped natural frequencies, m denotes the vehicle's total mass, I_{yy} is the pitch axis moment of inertia, g_0 is the acceleration due to gravity at sea level, and R_E is the radius of the Earth [88].

- *States.* Vehicle states include: velocity v, FPA γ, altitude h, pitch rate q, pitch angle θ, and the flexible body states $\eta_1, \dot{\eta}_1, \eta_2, \dot{\eta}_2, \eta_3, \dot{\eta}_3$. These eleven (11) states are summarized in Table 4.1.

♯	Symbol	Description	Units
1	v	speed	kft/sec
2	γ	flight path angle	deg
3	θ	pitch	deg
4	q	pitch rate	deg/sec
5	h	altitude	ft
6	η_1	1^{st} flex mode	-
7	$\dot{\eta_1}$	1^{st} flex mode rate	-
8	η_2	2^{nd} flex mode	-
9	$\dot{\eta_2}$	2^{nd} flex mode rate	-
10	η_3	3^{rd} flex mode	-
11	$\dot{\eta_3}$	3^{rd} flex mode rate	-

Table 4.1: States for Hypersonic Vehicle Model

- *Controls.* The vehicle has three (3) control inputs: a rearward situated elevator δ_e, a forward situated canard δ_c [1] , and stoichiometrically normalized fuel equivalence ratio (FER). These control inputs are summarized in Table 4.2.

♯	Symbol	Description	Units
1	FER	stoichiometrically normalized fuel equivalence ratio	-
2	δ_e	elevator deflection	deg
3	δ_c	canard deflection	deg

Table 4.2: Controls for Hypersonic Vehicle Model

In the above model, we note that the rigid body motion impacts the flexible dynamics through the generalized forces. As discussed earlier, the flexible dynamics impact the rigid body motion through thrust, lift, drag, and moment. Nominal model parameter values for the vehicle under consideration are given in Table 4.3. Additional details about the model may be found within the following references [72, 73, 77–88].

[1] In this work, we have removed the canard. Future work will examine the potential utility of a canard as well as its viability.

Parameter	Nominal Value	Parameter	Nominal Value
Total Length (L)	100 ft	Engine Length	20 ft
Forebody Length (L_1)	47 ft	Aftbody Length (L_2)	33 ft
Elevator position	(-85,-3.5) ft	Elevator Area	17 ft^2
Engine inlet height h_i	3 ft	Engine exhaust height h_e	3 ft
Diffuser area ratio	0.1	Nozzle area ratio	10
Upper forebody angle (τ_{1U})	3^o	Lower forebody angle (τ_{1L})	6.2^o
Tail angle (τ_2)	14.342^o	Mean Elasticity Modulus	8.65×10^7 psi
Center of gravity	(-55,0) ft	Weight per unit width	6.14×10^3 lbs/ft
Titanium Thickness	9.6 in	Moment of Inertia I_{yy}	8.67×10^4 slugs ft^2/ft
First Flex. Mode (ω_{n_1})	19.76 rad/s	Second Flex. Mode (ω_{n_2})	47.84 rad/s
Third Flex. Mode (ω_{n_3})	94.91 rad/s	Flex. Mode Damping (ζ)	0.02

Table 4.3: Vehicle Nominal Parameter Values

In the next section, the impact of the plume model is demonstrated. Speed-fidelity tradeoffs are addressed. A widely used plume approximation was introduced within [102] and used in [72, 87]. The next section will outline an alternative approximation method and compare it to the previous methods.

4.3 Trim and Linearization

In this section we examine the trimming and linearization of the model. Trimming the vehicle refers to finding an equilibrium point of the nonlinear model presented in Equation (4.1). Linearization is used to obtain a linear model (small signal approximation) to the nonlinear differential equations of the vehicle dynamics. The work presented in this section has appeared in [6].

4.3.1 Trimming

For a general nonlinear system, we have the following state space representation:

$$\dot{x}(t) = f(x(t), u(t)) \qquad x(0) = x_o \tag{4.2}$$

where

- $f = [\ f_1(x_1, \ldots, x_n, u_1, \ldots, u_m), \ldots, f_n(x_1, \ldots, x_n, u_1, \ldots, u_m)\ ]^T \in \mathcal{R}^n$ - vector of n functions
- $u = [\ u_1, \ldots, u_m\ ]^T \in \mathcal{R}^m$ - vector of m input variables
- $x = [\ x_1, \ldots, x_n\ ]^T \in \mathcal{R}^n$ - vector of n state variables
- $x_o = [\ x_{1_o}, \ldots, x_{n_o}\ ]^T \in \mathcal{R}^n$ - vector of n initial conditions

(x_e, u_e) is an *equilibrium* or *trim* of the nonlinear system at t = 0 if

$$f(x, u) = 0 \qquad \text{for all } t \geq 0 \tag{4.3}$$

Trimming refers to finding system equilibria; i.e. state-control vector pairs (x_e, u_e) such that $f(x_e, u_e) = 0$.

- The trimmable region limited by 3 effects:
  - Structural loading due to high dynamic pressure q = 2000 psf.
  - Thermal choking within engine ([1]).
  - FER = 1 ([1]).

- Many static properties are constant (or fairly constant) along lines of constant dynamic pressure ([6]).

The general procedure for trimming the vehicle is given below; an optimization based approach to execute those steps is examined next.

1. Choose Mach and altitude (within trimmable region).
2. Set pitch rate, flexible state derivatives to zero.
3. Set $\theta = \alpha$ (level flight or $\gamma = \theta - \alpha = 0°$).
4. Solve $f(x, u) = 0$ for AOA, flexible states, controls (elevator, FER).

In order to obtain the equilibrium numerically, we solve the following optimization problem:

$$\min_{x,u} \|\dot{x}\|_\infty \tag{4.4}$$

where $\dot{x}$ is the derivatives of the state (we want them to be small at trim), x is the states vector, u are the controls. This minimax optimization is solved using the *fmincon* MATLAB routine.

Once a trim of the nonlinear differential equation is found, we can linearize the vehicle about the equilibrium point. This is examined next.

4.3.2 Linearization

For a general nonlinear system, we have the following state space representation:

$$\dot{x}(t) = f(x(t), u(t)) \qquad x(0) = x_o \tag{4.5}$$

$$Y(t) = g(x(t), u(t)) \tag{4.6}$$

where

- $f = [\ f_1(x_1, \ldots, x_n, u_1, \ldots, u_m), \ldots, f_n(x_1, \ldots, x_n, u_1, \ldots, u_m)\ ]^T \in \mathcal{R}^n$ - vector of n functions
- $g = [\ g_1(x_1, \ldots, x_n, u_1, \ldots, u_m), \ldots, g_p(x_1, \ldots, x_n, u_1, \ldots, u_m)\ ]^T \in \mathcal{R}^p$ - vector of p functions
- $u = [\ u_1, \ldots, u_m\ ]^T \in \mathcal{R}^m$ - vector of m input variables
- $x = [\ x_1, \ldots, x_n\ ]^T \in \mathcal{R}^n$ - vector of n state variables
- $x_o = [\ x_{1_o}, \ldots, x_{n_o}\ ]^T \in \mathcal{R}^n$ - vector of n initial conditions.
- $y = [\ y_1, \ldots, y_n\ ]^T \in \mathcal{R}^p$ - vector of p outputs

Let (x_e, u_e) be an *equilibrium* of the nonlinear system. A linear state space representation (ssr) which approximates the nonlinear system near (x_e, u_e) is obtained:

$$\delta\dot{x}(t) = A\delta x(t) + B\delta u(t) \qquad \delta x(0) = \delta x_o \tag{4.7}$$

$$\delta y(t) = C\delta x(t) + D\delta u(t) \tag{4.8}$$

where

$$A = \left[\begin{array}{ccc} \frac{\partial f_1}{\partial x_1} & \cdots & \frac{\partial f_1}{\partial x_n} \\ \vdots & \vdots & \vdots \\ \frac{\partial f_n}{\partial x_1} & \cdots & \frac{\partial f_n}{\partial x_n} \end{array} \right]_{(x_e,u_e)} \qquad B = \left[\begin{array}{ccc} \frac{\partial f_1}{\partial u_1} & \cdots & \frac{\partial f_1}{\partial u_m} \\ \vdots & \vdots & \vdots \\ \frac{\partial f_n}{\partial u_1} & \cdots & \frac{\partial f_n}{\partial u_m} \end{array} \right]_{(x_e,u_e)} \tag{4.9}$$

$$C = \left[\begin{array}{ccc} \frac{\partial g_1}{\partial x_1} & \cdots & \frac{\partial g_1}{\partial x_n} \\ \vdots & \vdots & \vdots \\ \frac{\partial g_p}{\partial x_1} & \cdots & \frac{\partial g_p}{\partial x_n} \end{array} \right]_{(x_e,u_e)} \qquad D = \left[\begin{array}{ccc} \frac{\partial g_1}{\partial u_1} & \cdots & \frac{\partial g_1}{\partial u_m} \\ \vdots & \vdots & \vdots \\ \frac{\partial g_p}{\partial u_1} & \cdots & \frac{\partial g_p}{\partial u_m} \end{array} \right]_{(x_e,u_e)} \tag{4.10}$$

$$\delta u(t) \stackrel{\text{def}}{=} u(t) - u_e \qquad \delta x(t) \stackrel{\text{def}}{=} x(t) - x_e \qquad \delta x_o \stackrel{\text{def}}{=} x_o - x_e$$

$$\delta y(t) \stackrel{\text{def}}{=} y(t) - y_e \qquad y_e \stackrel{\text{def}}{=} g(x_e, u_e)$$

Since analytic expressions for the partial derivatives listed in equation 4.9 are not available, they must be approximated numerically using finite differences.

The standard centralized finite difference has been implemented:

$$\frac{df}{dx} = \frac{f(x + \Delta x) - f(x - \Delta x)}{2\Delta x} \tag{4.11}$$

Consider the simple example where

$$f = sin(x) \tag{4.12}$$

- For the simple example, step size bounds must be between $[10^{-13}\ 10^{-2}]$
- In general, for the complex nonlinear model the bounds are small: $[10^{-5}\ 10^{-3}]$

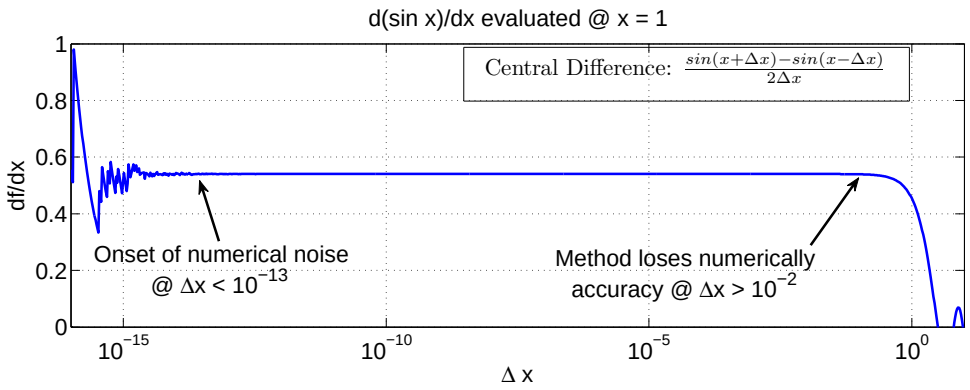

Figure 4: Simple Linearization Example

- Bounds may vary for each element of equation 4.9.
- Bounds may vary based on operating point.
- Blind implementation of MATLAB *linmod* command will not take this into account.

Based on the equations of motion (4.1a-4.1f), we define the following accelerations:

$$X = \frac{T\cos(\alpha) - D}{m} \tag{4.13}$$

$$Z = -\frac{T\sin(\alpha) + L}{m} \tag{4.14}$$

$$\mathscr{M} = \frac{M}{I_{yy}} \tag{4.15}$$

where L is the lift, D is the drag, T is the thrust, M is the moment, α is the angle of attack, m is the mass of the vehicle and I_{yy} is the moment of inertia.

We construct a model with the following states and controls

- $\mathbf{x} = [V_t \;\; \alpha \;\; Q \;\; h \;\; \theta \;\; \eta \;\; \dot{\eta} \;\; \cdots]^T$ (we may extend the vector x to include as many flexible modes as required. Below we use three flexible states and their derivatives)
- $\mathbf{u} = [\delta_e \;\; \delta_\phi]^T$ (we are considering a two control model with only the elevator and the FER as inputs)

Below, we provide a ssr for the linearized model [83]

$$\mathbf{A} = \begin{bmatrix} X_v & X_\alpha & 0 & X_h & -g & X_{\eta_1} & 0 & ... & X_{\eta_3} & 0 \\ \frac{Z_v}{V_{T_0}} & \frac{Z_\alpha}{V_{T_0}} & 1-\frac{Z_Q}{V_{T_0}} & \frac{Z_h}{V_{T_0}} & 0 & \frac{Z_{\eta_1}}{V_{T_0}} & 0 & ... & \frac{Z_{\eta_3}}{V_{T_0}} & 0 \\ \mathscr{M}_v & \mathscr{M}_\alpha & \mathscr{M}_Q & \mathscr{M}_h & 0 & \mathscr{M}_{\eta_h} & 0 & ... & \mathscr{M}_{\eta_h} & 0 \\ 0 & -V_0 & 0 & 0 & V_0 & 0 & 0 & ... & 0 & 0 \\ 0 & 0 & 1 & 0 & 0 & 0 & 0 & ... & 0 & 0 \\ 0 & 0 & 0 & 0 & 0 & 0 & 1 & ... & 0 & 0 \\ N_{1,v} & N_{1,\alpha} & 0 & N_{1,h} & 0 & -\omega_1^2+N_{1,\eta_1} & -2\zeta\omega_1+N_{1,\dot{\eta_1}} & ... & N_{1,\eta_3} & 0 \\ 0 & 0 & 0 & 0 & 0 & 0 & 0 & ... & 0 & 0 \\ N_{2,v} & N_{2,\alpha} & 0 & N_{2,h} & 0 & N_{2,\eta_1} & 0 & ... & N_{1,\eta_3} & 0 \\ 0 & 0 & 0 & 0 & 0 & 0 & 0 & ... & 0 & 1 \\ N_{3,v} & N_{3,\alpha} & 0 & N_{3,h} & 0 & N_{3,\eta_1} & 0 & ... & -\omega_3^2+N_{3,\eta_3} & -2\zeta\omega_3+N_{3,\dot{\eta_3}} \end{bmatrix} \tag{4.16}$$

$$\mathbf{B} = \begin{bmatrix} X_{\delta_e} & X_{\delta_\phi} \\ \frac{Z_{\delta_e}}{V_{T_0}} & \frac{Z_{\delta_\phi}}{V_{T_0}} \\ \mathscr{M}_{\delta_e} & \mathscr{M}_{\delta_\phi} \\ 0 & 0 \\ 0 & 0 \\ 0 & 0 \\ N_{1,\delta_e} & N_{1,\delta_\phi} \\ 0 & 0 \\ N_{2,\delta_e} & N_{2,\delta_\phi} \\ 0 & 0 \\ N_{3,\delta_e} & N_{3,\delta_\phi} \end{bmatrix} \tag{4.17}$$

For completeness, the dimensional derivatives equations for the rigid body modes are given below.

$$X_v = \frac{1}{m}\left(\frac{\partial T}{\partial V_T}\cos(\alpha_0) + \frac{\partial D}{\partial V_T}\right) \tag{4.18}$$

$$X_\alpha = \frac{1}{m}\left(\frac{\partial T}{\partial \alpha}\cos(\alpha_0) + \frac{\partial D}{\partial \alpha} + L_0\right) \tag{4.19}$$

$$X_h = \frac{1}{m}\left(\frac{\partial T}{\partial h}\cos(\alpha_0) + \frac{\partial D}{\partial h}\right) \tag{4.20}$$

$$Z_v = -\frac{1}{m}\left(\frac{\partial T}{\partial V_T}\sin(\alpha_0) + \frac{\partial L}{\partial V_T}\right) \tag{4.21}$$

$$Z_\alpha = -\frac{1}{m}\left(\frac{\partial T}{\partial \alpha}\sin(\alpha_0) + \frac{\partial L}{\partial \alpha} + D_0\right) \tag{4.22}$$

$$Z_Q = -\frac{1}{m}\left(\frac{\partial T}{\partial h}\sin(\alpha_0) + \frac{\partial L}{\partial h}\right) \tag{4.23}$$

$$Z_h = -\frac{1}{m}\left(\frac{\partial T}{\partial h}\sin(\alpha_0) + \frac{\partial L}{\partial h}\right) \tag{4.24}$$

$$\mathscr{M}_{V_T} = \frac{1}{I_{yy}}\frac{\partial M}{\partial V_T} \tag{4.25}$$

$$\mathscr{M}_\alpha = \frac{1}{I_{yy}}\frac{\partial M}{\partial \alpha} \tag{4.26}$$

$$\mathscr{M}_Q = \frac{1}{I_{yy}}\frac{\partial M}{\partial Q} \tag{4.27}$$

$$\mathscr{M}_h = \frac{1}{I_{yy}}\frac{\partial M}{\partial h} \tag{4.28}$$

$$X_{\delta_e} = \frac{1}{m}\left(\frac{\partial T}{\partial \delta_e}\cos(\alpha_0) + \frac{\partial D}{\partial \delta_e}\right) \tag{4.29}$$

$$Z_{\delta_e} = -\frac{1}{m}\left(\frac{\partial T}{\partial \delta_e}\sin(\alpha_0) + \frac{\partial L}{\partial \delta_e}\right) \tag{4.30}$$

$$\mathscr{M}_{\delta_e} = \frac{1}{I_{yy}}\frac{\partial M}{\partial \delta_e} \tag{4.31}$$

$$X_{\delta_\phi} = \frac{1}{m}\left(\frac{\partial T}{\partial \delta_\phi}\cos(\alpha_0) + \frac{\partial D}{\partial \delta_\phi}\right) \tag{4.32}$$

$$Z_{\delta_\phi} = -\frac{1}{m}\left(\frac{\partial T}{\partial \delta_\phi}\sin(\alpha_0) + \frac{\partial L}{\partial \delta_\phi}\right) \tag{4.33}$$

$$\mathscr{M}_{\delta_\phi} = \frac{1}{I_{yy}}\frac{\partial M}{\partial \delta_\phi} \tag{4.34}$$

4.4 Plume Modeling and Analysis

Plume modeling refers to the method of calculating the pressures along the aftbody of the vehicle [102]. The aftbody pressure distribution is primarily due to the external expansion of the exhaust from the scramjet. The aftbody forms the upper portion of the nozzle. The

lower portion of the exhaust plume (shear layer) forms the lower portion of the nozzle. In general, the determination of the shear layer involves a nonlinear iteration - equating the exhaust pressure with a suitable pressure (e.g. engine base pressure, pressure across bow shock, or free stream pressure) upstream of the shear layer. Within [103], a numerical discretization procedure for a plume calculation is described. This calculation can be very time consuming, but is generally considered the most accurate method short of CFD modeling [102]. To address the computational complexity issue, the authors within [72], [102, page 1315] make a simplifying assumption - hereafter referred to as "simple approximation". This simplifying assumption significantly speeds up the calculation of the aft body pressure distribution. However, it will be shown that several of the assumptions leading to this approximation may result in large error when compared to the numerical discretization. This section will then describe a new method that will yield a more "high-fidelity" approximation which trades-off computational time in favor of accuracy. Static and dynamics results for all three methods will be compared. The work presented here has appeared in [8]

4.4.1 Modeling Techniques

Method #1: Simple Plume Approximation. To reduce the computation complexity of the plume calculation, the authors of [102] made the following assumptions:

1. The pressure at the aft most tip of the vehicle will be equal to the freestream pressure (p_∞)
2. The aftbody pressure varies inversely with the distance along the aftbody
3. For a fixed exhaust pressure, the aftbody pressure does not change with respect to change in angle of attack.

Based on these three assumptions, the following equation is used to calculate the pressure along the aftbody of the vehicle:

$$P_a(x) \approx \frac{P_e}{1 + \left(\frac{x}{L_2}\right)\left(\frac{P_e}{P_\infty} - 1\right)} \tag{4.35}$$

where:

- P_a - Aftbody pressure.
- x - Location along the aftbody where pressure is computed ($x \in 0$, L_2).
- P_∞ - Free stream pressure.
- P_e - Pressure at the internal nozzle exit.
- L_2 - Length of the aftbody.

One benefit to equation 4.35 is that it can be quickly computed and does not require discretization of the aftbody into segments. It must be noted, however, that the assumptions it is based on are not true in general (see Figure 6). This fact has implication on vehicle's static and dynamic properties as well as control.

Additionally, we have the pressure at the end of the aftbody must equal the freestream pressure (from equation (4.35)) i.e. it is assumed that the external nozzle suffers from neither under-expansion nor over-expansion.

Method #2: Numerical Discretization Plume Calculation. The aftbody and shear-layer are discretized into N segment. The flow within each section (bounded by the aftbody and the 'linearized' segment of the shear layer) is modeled as an isentropic nozzle (Figure 5 illustrates one such segment).

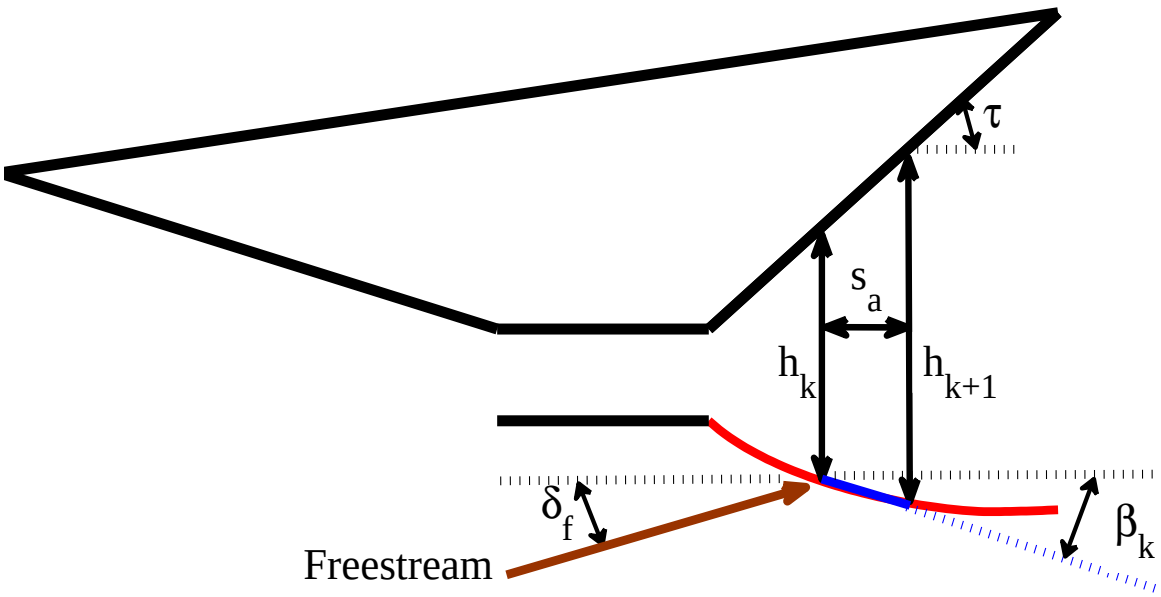

Figure 5: Segmentation of plume

The pressure in segment k ($k \in$ [0, N]) is obtained by solving the following equations numerically [103]:

$$h_{k+1} = h_k + s_a \tan(\tau) + s_a \tan(\beta_k) \tag{4.36a}$$

$$A_k = \frac{h_{k+1}}{h_k} \tag{4.36b}$$

$$f(M_k) = 1 + \frac{1}{2}(\gamma - 1) M_k^2 \tag{4.36c}$$

$$\frac{f(M_k)^{\frac{\gamma+1}{\gamma-1}}}{M_k^2} = A_k^2 \frac{f(M_{k-1})^{\frac{\gamma+1}{\gamma-1}}}{M_{k-1}^2} \tag{4.36d}$$

$$P_k = P_{k-1}\left[\frac{f(M_{k-1})}{f(M_k)}\right]^{\frac{\gamma}{\gamma-1}} \tag{4.36e}$$

$$\overline{P_k} = \overline{\rho_e}\overline{V_e}^2 \sin^2(\beta_k - \delta_f) + \overline{P_e} \tag{4.36f}$$

subject to the following constraints:

$$0 \leq \beta_k < \frac{\pi}{2} \tag{4.37}$$

where:

- A_k - Nozzle area ratio of segment k of aftbody.
- P_k - Nozzle pressure in segment k of the aftbody.
- $\overline{P_k}$ - External stream pressure in segment k of the aftbody.
- $\overline{\rho_e}$ - Density of stream under the shear layer.
- τ - Inclination of aftbody to the body axis.
- δ_f - Inclination of external flow to body axis.
- s_a - Width of each segment of the aftbody.
- M_0, P_0 - conditions at internal nozzle exit.
- M_k - Nozzle Mach at segment k of aftbody.
- $\overline{M_k}$ - External stream Mach at segment k of aftbody.
- $\overline{P_e}$ - Pressure of stream under the shear layer.
- $\overline{V_e}$ - Velocity of stream under the shear layer.
- β_k - Inclination of kth segment of the shear layer to the body axis.
- γ - Ratio of specific heats (=1.4).
- h_k - Height of segment k of aftbody nozzle.
- h_0 - exit height of engine.

By substituting equation (4.36c) into (4.36d) we obtain the equation relating the Mach in an isentropic nozzle with an area ratio of A_k. Similarly, equation (4.36e) is the equation for the pressure across an isentropic nozzle. Furthermore, the freestream impacts the shear layer at an angle of β - δ_f, and this is modeled using Newtonian impact theory (i.e. equation (4.36f)).

Equations (4.36a) – (4.36e) provide an iterative procedure to calculating the pressure across the entire plume. Central to this procedure is obtaining β_k such that P_k from equations (4.36e) matches $\overline{P_k}$ from equation (4.36f). The solution for each segment of the aftbody must be found through numeric iteration. Also, each segment must be calculated sequentially (since it depends on the conditions from the segment prior to it), and therefore the algorithm cannot be well parallelized. In practice, bounds on β_k can be used to speed up its estimation (we know that $\{\beta_i, i \in \{0, 1, 2, \ldots, N\}\}$ is a monotonically decreasing sequence), but the computation time is still significant.

It is clear that there exists a solution to system of equations (4.36), (4.37) so long as the pressure within the plume is greater than the pressure of the stream under the shear layer (i.e. the plume is under-expanded). In case this is not true, there does not exist a positive β solution, and equation (4.36f) can no longer be used (however, equations (4.36a) - (4.36e) are still valid as long as $\beta \leq -\tau$). In case the plume is over-expanded, we replace the Newtonian impact equation (4.36f) by a Prandtl-Meyer expansion relation:

$$\nu\left(\overline{M}\right) = \sqrt{\frac{\gamma+1}{\gamma-1}}\arctan\left(\sqrt{\frac{\gamma-1}{\gamma+1}(\overline{M}^2-1)}\right) - \sqrt{\overline{M}^2-1} \tag{4.38a}$$

$$\nu\left(\overline{M_{k+1}}\right) = \nu\left(\overline{M_k}\right) + \delta_{f,k} - \beta_k \tag{4.38b}$$

$$\overline{P_k} = \overline{P_{k-1}}\left[\frac{f(\overline{M_{k-1}})}{f(\overline{M_k})}\right]^{\frac{\gamma}{\gamma-1}} \tag{4.38c}$$

where

- $\overline{P}$, $\overline{M}$ are conditions of external stream.
- $\delta_{f,k}$ is external flow orientation to body axis before segment k.

Since an expansion fan turns the flow parallel to the surface, we assume $\delta_{f,k} = \beta_{k-1}$. The initial conditions are approximated using the last segment where the pressure inside the plume is greater than the pressure beneath the shear layer.

As in the over-expanded case, we use an iterative procedure wherein each β_k is calculated such that $\overline{P_k}$ (from equation (4.38c)) equals P_k (from equation (4.36e)).

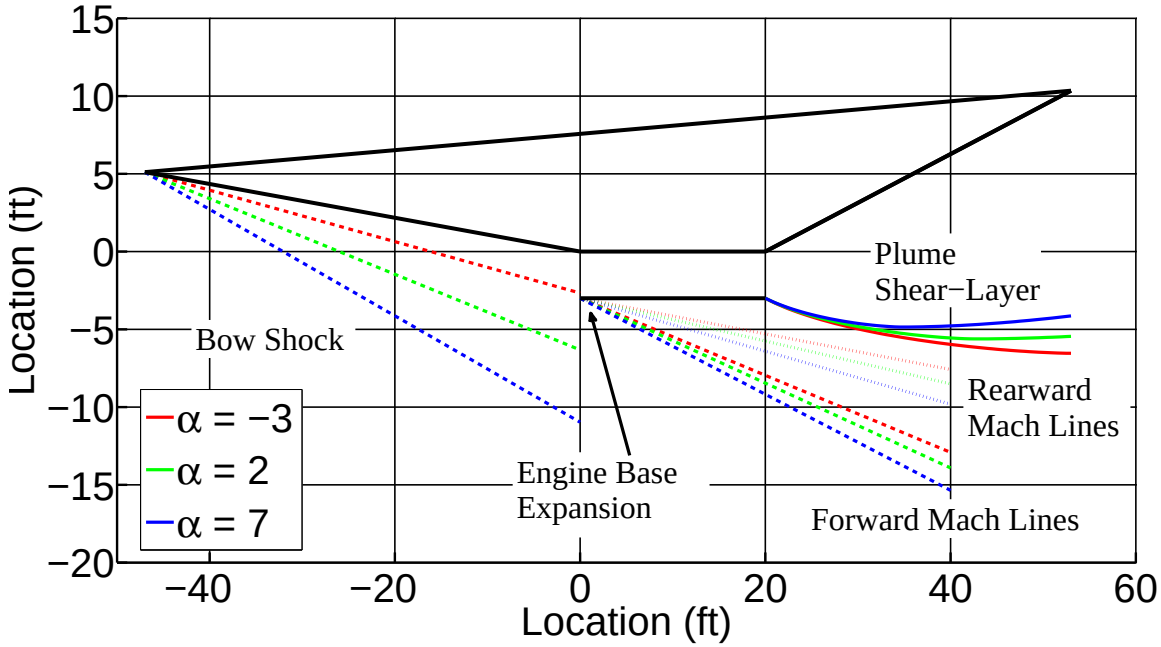

Figure 6: Plume Shape w.r.t. AOA

Figure 6 shows the plume shear-layer for several different angles of attack at Mach 8, 85,000 ft. It is important to note that:

- α = 2 represents the trim value for this flight condition.
- The plume shear layer will interact with the pressure due to the flow expansion that occurs at the engine base for most flight scenarios. Only for large negative angles of attack will part of the plume shear-layer interact with the free stream flow. This situation would not occur for trimming of the vehicle, or typical control maneuvers.

Method #3: High Fidelity Plume Approximation. Due to the computation time required for the previous method (see Table 4.5), an approximation to this method is useful. The approximation method outlined below that will attempt to exploit the following from equation (4.36d):

$$\frac{(M_k)^2}{(M_{k-1})^2} \downarrow 1 \; as \; (A_k)^2 = \frac{(h_{k+1})^2}{(h_k)^2} \downarrow 1 \tag{4.39}$$

This allows for equation (4.36e) to be approximated as:

$$\hat{P}_k = P_{k-1} A_k^{\frac{-2\gamma}{\gamma+1}} \tag{4.40}$$

$$= P_{k-1} \left[\left(1 + \frac{s_a \tan(\tau)}{h_k} \right) + \frac{s_a}{h_k} \tan(\beta_k) \right]^{\frac{-2\gamma}{\gamma+1}} \tag{4.41}$$

where $\hat{P}_k$ is an approximation to P_k of equation (4.36e).

Since s_a in equation (4.36a) is an adjustable parameter that can be made arbitrarily small, and $\beta_k \leq 90°$, A_k (equivalently $\frac{M_k}{M_{k-1}}$) can be made arbitrarily close to 1. However, the number of iterations is inversely proportional to s_a. Hence there is a computational tradeoff between accuracy and computation time. The error between the approximated pressure ($\hat{P}_k$) and the original pressure (P_k) is calculated by subtraction equation (4.36e)

from equation (4.41):

$$|\hat{P}_k - P_k| = \left| P_{k-1} A_k^{\frac{-2\gamma}{\gamma+1}} \right| \left| 1 - \left(\frac{M_k}{M_{k-1}} \right)^{\frac{-2\gamma}{\gamma+1}} \right| \tag{4.42}$$

$$\leq P_{k-1} \left| 1 - \left(\frac{M_k}{M_{k-1}} \right)^{\frac{-2\gamma}{\gamma+1}} \right| \tag{4.43}$$

Equation (4.43) shows us that $|\hat{P}_k - P_k| \to 0$ as $s_a \downarrow 0$. Thus we can achieve accurate approximations to the pressure in equation (4.36e). This approximation is further simplified to improve the computational speed. Consider the following Maclaurin expansion to equation (4.41):

$$\tilde{P}_k = P_{k-1} \left[\left(\frac{c_1}{c_2} \right)^{\kappa} + \kappa \left(\frac{c_1}{c_2} \right)^{\kappa-1} \Delta_k + \frac{\kappa(\kappa-1)}{2!} \left(\frac{c_1}{c_2} \right)^{\kappa-2} \Delta_k^2 + \ldots + \frac{\kappa(\kappa-1)\ldots(\kappa-n-1)}{n!} \left(\frac{c_1}{c_2} \right)^{\kappa-n} \Delta_k^n \right] c_2^{\kappa} \tag{4.44}$$

where

- $c_1 = \left(1 + \frac{s_a \tan(\tau)}{h_k}\right)$.
- $c_2 = \frac{s_a}{h_k}$.
- $\kappa = \frac{-2\gamma}{\gamma+1}$.
- $\Delta_k = \tan(\beta_k)$.

We can calculate the error between this polynomial approximation $\tilde{P}_k$ and the original approximation $\hat{P}_k$ by using the remainder term for a truncated Maclaurin series [104]:

$$|\hat{P}_k - \tilde{P}_k| = P_{k-1} \left| \left[\frac{\kappa(\kappa-1)\ldots(\kappa-n)}{(n+1)!} \left(\frac{c_1}{c_2} + t_k \right)^{\kappa-n-1} \Delta_k^{n+1} \right] c_2^{\kappa} \right| \tag{4.45}$$

where t_k is some number between 0 and Δ_k.

In order to obtain bounds on the error between the original pressure (P_k, equation (4.36e)) and the pressure from the truncated Maclaurin series ($\tilde{P}_k$, equation (4.44)), we use the triangle inequality to combine equation (4.43) and equation (4.45) as follows:

$$|\tilde{P}_k - P_k| \leq P_{k-1} \left(\left| \left[\frac{\kappa\,(\kappa-1)\ldots(\kappa-n)}{(n+1)!} \left(\frac{c_1}{c_2} + t_k \right)^{\kappa-n-1} \Delta_k^{n+1} \right] c_2^{\kappa} \right| + \left| 1 - \left(\frac{M_k}{M_{k-1}} \right)^{\frac{-2\gamma}{\gamma+1}} \right| \right) \quad (4.46)$$

From equation (4.46) we see that $|\tilde{P}_k - P_k|$ can be made arbitrarily close to zero (irrespective of t_k) by choosing s_a sufficiently small (since $\kappa < 0$, $\frac{c_1}{c_2} \geq 1$, and $c_2 \downarrow 0$ as $s_a \downarrow 0$). Specifically, if the order of the approximation is fixed across all segments of the plume, we observe the following:

- For a fixed order, $|\tilde{P}_k - \hat{P}_k| \downarrow 0$ (exponentially) as $s_a \downarrow 0$.
- For a fixed nozzle area ratio (A_k), $\frac{M_k}{M_{k-1}} \downarrow 1$ as M_{k-1} increases; for a fixed M_{k-1}, $\frac{M_k}{M_{k-1}} \downarrow 1$ as the nozzle area ratio (A_k) decreases.

Hence, when the order of the approximation is fixed, a fixed s_a can be chosen to bound $|\tilde{P}_k - P_k|$ irrespective of k: P_k (M_k) is bounded above (below) by the engine exhaust pressure (Mach), and Δ_k (equivalently A_k) is bounded above by the value of Δ_0 of the first step. A second order approximation was found to be sufficiently accurate (refer Table 4.7).

Moreover, equation (4.36f) can also be expanded as a polynomial in $\tan(\beta_k)$, and we can equate the two polynomials. Since the restriction of the tangent function to the open interval (0, $\frac{\pi}{2}$) is bijective from its domain to the positive reals, we can obtain β_k by solving the polynomial expression and choosing the appropriate solution. For the case

of an under-expanded plume, a similar polynomial expression for a function of β_k can be easily obtained by using an approximation to the Prandtl-Meyer expansion [105] and equations (4.38).

The objective of the method is find β_k s.t. $\hat{P}_k$ from equations (4.44) matches $\overline{P_k}$ from equation (4.36f) (or the equivalent under-expanded approximation, assuming the base pressure for P_e). While this method still require's an iterative solution to discretized of the aftbody segments, β_k is can now be written in as a polynomial equation (through a Maclaurin expansion) as opposed to a general nonlinear equation. This will result in a significant computation speedup as shown in Table 4.5. Using a lookup table for calculating the polynomial roots can result in further savings to the computation time.

Computation Times. Table 4.5 shows the computation time necessary to make a single call to the model and the time to calculate the trim inputs/states at a single flight condition. The simple approximation is approximately two order of magnitude faster than the numerical discretization. the high fidelity approximation is one order of magnitude faster than the numerical discretization.

Method	Computation Time (Single point)	Computation Time (Trim)
Numerical Discretization	1.4 s	510.3 s
Simple Approximation	0.010 s	3.4 s
High Fidelity Approximation	0.17 s	65.1 s

Table 4.5: Computational Time for Each Method on 2.66 GHz Processor

4.4.2 Developing Bounds

Due to the large amount of uncertainty and time varying nature, obtaining an accurate "truth model" for the aftbody pressure may not be achievable. Formulating uncertainty bounds can be useful for both estimating static performance capabilities as well as developing robust controls laws. The following candidate uncertainty bounds can be categorized in order in decreasing conservativeness.

Conservative Bounds Conservative bounds can be formulated by assuming a constant pressure profile along the aftbody. An upper bound for the aftbody pressure is given by the exhaust pressure from the engine (p_e). A lower bound for the pressure is given by the freestream pressure of air (p_∞).

Non-conservative bounds Non-conservative bound can be formulated through piece-wise linear segments as seen in Figure 7. The more aggressive the bound become, the more likely it is they are to violated through higher fidelity modeling methods. However, these aggressive bound can be useful for trim specifications and potential controller robustness.

4.4.3 Static and Dynamic Comparisons

Within [4] a feasibility condition for the engine parameter's was given, namely that $A_n = A_d^{-1}$ was necessary to have a "flat engine base" as shown in Figures 3 and 6. Previous results in the literature [72] have used a nominal engine configuration ($A_d = 1,\ A_n = 6.35$) that does not satisfy this condition. This dissertation will use a "new engine" with parameters of $A_d = 0.1,\ A_n = 10$ so that the feasibility condition is satisfied.

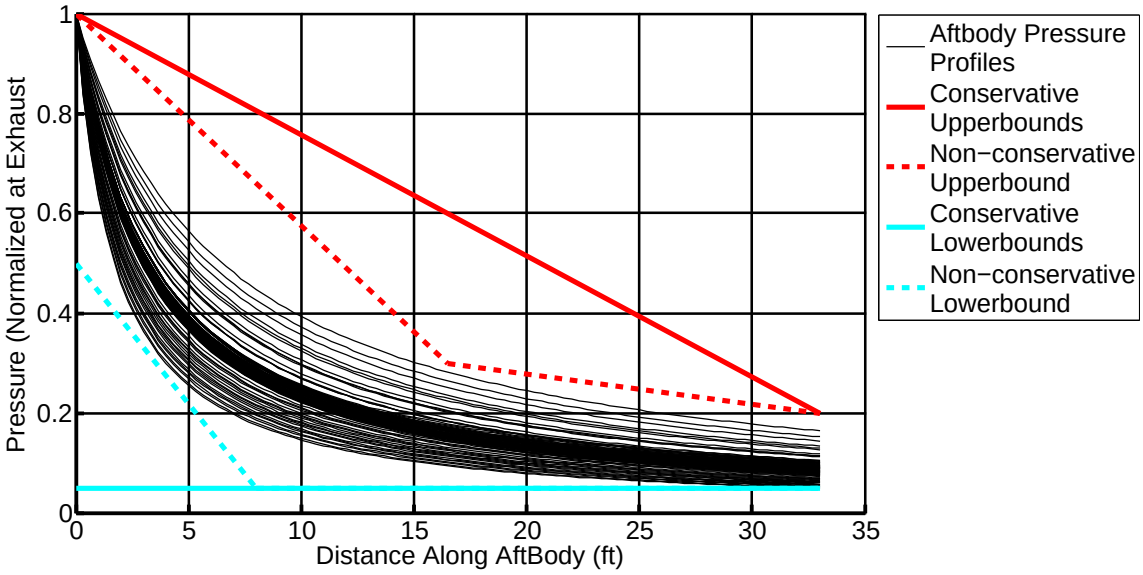

Figure 7: Aftbody Pressure Bounds

Static Properties: Mach 8, 85 kft. Table 4.6 shows the trim properties for the different modeling methodologies as well as the bounds.

	Elevator	FER	AOA	RHP Pole	RHP Zero
Conservative L.B.	10.67	0.25	2.50	2.81	7.45
Non-conservative L.B.	8.90	0.20	2.01	2.79	7.50
Numerical Discretization	6.58	0.14	1.83	2.20	7.60
Simple Approximation	6.84	0.15	1.83	2.98	7.57
High Fidelity Approx.	6.60	0.14	1.83	2.20	7.60
Non-conservative U.B.	-1.87	0.05	0.02	2.16	8.33
Conservative U.B.	-3.64	0.03	1.43	2.85	8.45

Table 4.6: Trim Properties

From Table 4.6 the following observations can be made:

- For trim, all three methods yield similar properties at Mach 8, 85kft. This is not the case as the angle of attack starts to vary (shown in the next section).
- The non-conservative lower bounds and upper bounds do a good job of bounding the trim elevator and FER.

- The simple approximation model gives a dramatically more unstable linear model than the numerical and high fidelity approximation (34 %).
- The non-conservative lower bounds and upper bounds #2 do a good job of bounding the trim dynamic properties of the model.

Dynamic Properties: Mach 8, 85 kft. Figure 8 shows the frequency responses for the plant inputs to the plant outputs. The FER frequency responses exhibit the following properties:

- The High Fidelity Approximation tracks the numerical discretization accurately in all channels at all frequencies. item There are significant discrepancies between the simple approximation and the numerical discretization at low frequencies (0.01 rad/s and smaller).
- For frequencies of 0.1 rad/s and larger, the simple approximation tracks the numerical discretization method fairly well in the velocity channels.
- For frequencies of 0.1 rad/s and larger, the simple approximation tracks the numerical discretization method fairly well in the elevator-to-FPA channel, but not the FER-to-FPA channel.
- Conclusion: The simple approximation may still be useful for characterizing the dynamics properties of the system at frequencies of interest (roughly 1 rad/s), but it will not be useful for predicating the steady state behaviors.

4.4.4 Angle of Attack Variation

Figure 9 shows the aftbody pressure distribution for angles of attack of -3, 2 and 5 degrees. For the trim angle of attack (2 degree) both the simple approximation and the high fidelity

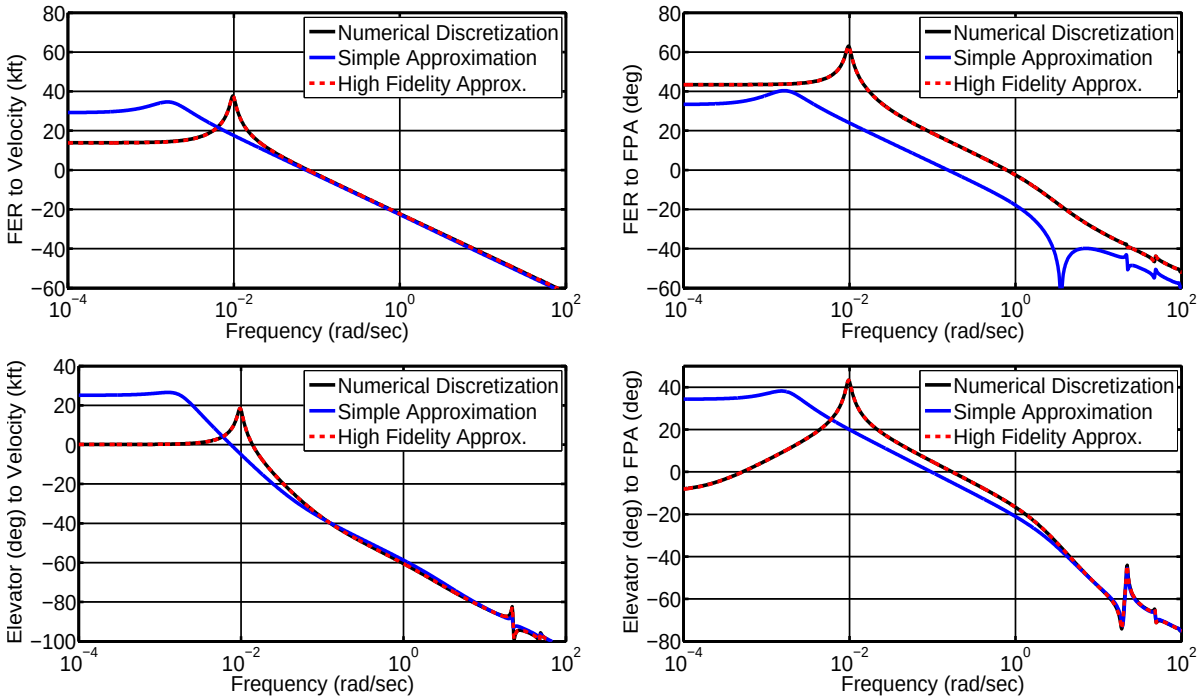

Figure 8: Plant Frequency Response

approximation correspond nicely to the numerical discretization method. As the angle of attack deviates from trim, the simple approximation no longer converges to the numerical discretization method. Table 4.7 shows the forces and moments generated by the aft body for each case, as well as the error of the approximations w.r.t. the numerical discretization. The high-fidelity approximation is invariant w.r.t. angle of attack, the maximum error is less that 0.4 %. The simple approximation can show errors as large as 50 % w.r.t. angle of attack variation.

4.5 Impact of Plume Models

In this section we examine the impact of the plume model on the vehicle design process. We look at how the control structure is impacted by using the new plume model (as compared to the Bolender model), as well as the impact of the plume model on a vehicle design optimizations. Through these examples, we illustrate the importance of the plume

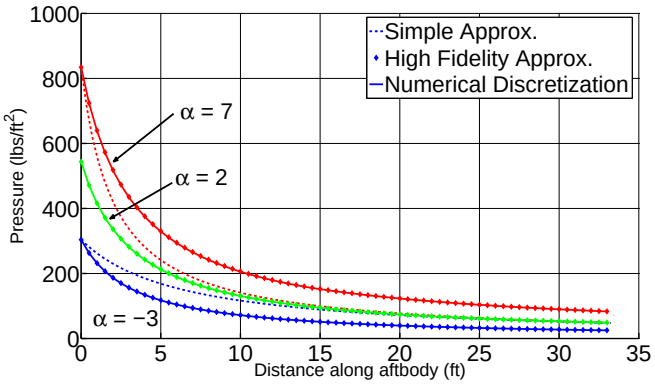

Figure 9: Plume Pressure Distribution Along Aftbody

Method (α=2 degrees)	F_x (lbf)	% Error	F_z (lbf)	% Error	M (lbf·ft)	% Error
Numerical Discretization	1295	-	4098	-	93,513	-
Simple Approx.	1300	0.4 %	4114	0.4 %	93,116	0.4 %
High Fidelity Approx.	1292	0.2 %	4089	0.2 %	9 3,319	0.2 %
Method (α=7 degrees)	F_x (lbf)	F_z (lbf)	M (lbf·ft)			
Numerical Discretization	2059	-	6517	-	151,011	-
Simple Approx.	1479	28.2 %	4682	28.2 %	101,555	28.2 %
High Fidelity Approx.	2052	0.3 %	6497	0.3 %	150,578	0.3 %
Method (α=-3 degrees)	F_x (lbf)	F_z (lbf)	M (lbf·ft)			
Numerical Discretization	707	-	2238	-	50,604	-
Simple Approx.	1072	51.3 %	3395	51.3 %	81,577	51.3 %
High Fidelity Approx.	705	0.3 %	2233	0.3 %	50478	0.3 %

Table 4.7: Approximation Forces and Moments

on vehicle and control design problems.

4.5.1 Impact of Plume - Controller Design

We first examine the impact of the plume on the controller structure. When the vehicle is modeled with the Bolender plume, a hierarchical PI-PD controller provides satisfactory performance [3].

With our (more accurate) plume model, however, such a simple controller is no longer sufficient to guarantee good properties. Since the velocity loop is much slower that the FPA channel, and is approximately first order, we close the velocity channel loop with a

PI controller. We then design a controller to minimize the peak sensitivity at the input (a convex control design problem) through the elevator channel. The results of this design procedure are shown in Figure 10.

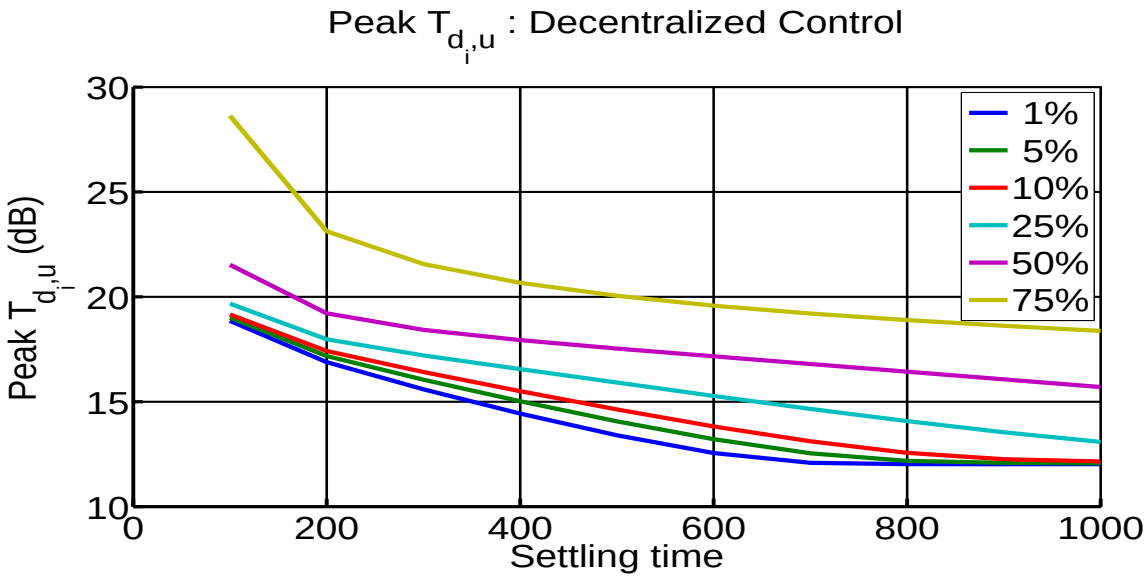

Figure 10: Decentralized Control Performance

From Figure 10, we observe the following:

- The peak sensitivity is no less than 10dB using a decentralized control with PI Velocity controller.
- Varying the bandwidth of the velocity channel impacts the achievable performance significantly.

Structured $\mathcal{H}^\infty$ controller design can also be done using several tools such as HiFOO [106] and Matlab [107]. Imposing structure, however, is often a non-convex optimization problem and difficult to solve in general.

Thus we see that a higher fidelity plume model significantly impacts the control architecture, requiring a more complex (centralized) controller structure as compared to the Bolender plume.

4.5.2 Impact of Plume - Vehicle Design Optimization

In Table 4.7 we observed how the plume model impacts the instantaneous forces and moments on the aircraft at different operating conditions. In this section, we examine the impact of the plume on achievable performance when the vehicle is in trim (for example, a cruising condition), and the design to achieve such performance. We use the simple approximation (S.A) and the high fidelity approximation (H.A) as two models for the plume, and compare the variation in achievable performance based on the plume model used. Additionally, we examine the effect of the plume model on the design of the vehicle - specifically we examine how the optimal design (for a particular objective) varies as the model of the plume changes. The material presented in this section has appeared in [8].

Objectives

We consider the following objectives for our vehicle design (at Mach 8, 85kft).

- Trim Fuel-rate - We attempt to minimize the fuel-rate at trim. This translates to lower fuel requirements, and mass reduction/increased payload capacities.
- Trim Lift-to-Drag Ratio (L/D) - We try to maximize the lift-to-drag ratio at trim.

Parameter Space

The space of vehicles over which we optimize the cost function is parameterized by the following vehicle attributes:

- Elevator area (S_{elev}): [8.5, 34] ft^2 (Nominal: 17 ft^2)
- Engine inlet height (h_i): [1, 5] ft (Nominal: 3.25)
- Lower forebody inclination (τ_L): [4.2^o, 8.2^o] (Nominal: 6.2^o)

The optimization algorithm attempts to find the best elevator area, engine dimension, and nose shape to optimize performance of the vehicle (measured by the objectives specified above). For each design considered, the vehicle was trimmed [6] and the cost calculated. As a result each iteration is computationally expensive (especially when the H.A. plume model is used - see Table 4.5). Since some designs may fail to trim, the cost function may be discontinuous in the space of vehicles. Therefore, gradient free optimization methods are considered, even though they often require more function calls to reach a local minima than gradient-descent methods. Moreover the problem is nonlinear with several local minima, and a multistart methods must be used.

Optimization Algorithm

For the problem of vehicle optimization, we use a genetic algorithm based approach. In [108] the author considers several advantages and disadvantages of evolutionary designs in aeronautical applications. Several other gradient-free algorithms (such as the Nelder-Mead nonlinear simplex algorithm) have also been used for vehicle design problems [4, 109]. In the nonlinear simplex approach each iteration requires just $(n + 1)$ vertices (where n is the dimension of the parameter space), and the choice of the initial simplex is important. In contrast, a large initial population can be used in an evolutionary algorithm (thereby allowing for a good representation of the search space). While this requires more function evaluations, we can distribute the evaluation of the function in each generation across

several processors. As a result, significant speedup in computation is obtained. Once the genetic algorithm solution is obtained, local optimality conditions can be used to test the validity of the solution.

The optimizations in this section were run on the Arizona State University (ASU) High Performance Computing (HPC) cluster, which consists of 570 dual quadcore Intel Xeon EM64T nodes each with 16 gigabytes of RAM. For each optimization, an initial population of a 100 is used (random population with a uniform distribution in the compact parameter space).

Results

Table 4.8 compares the static properties obtained by optimizing the vehicle for several metrics, using both the S.A. and H.A. plume models; the corresponding vehicle parameters are presented in Table 4.9. The optimal designs are visualized in Figure 11.

Objective	Trim Lift/Drag		Trim FER		Fuel Rate (slg/sec)		Trim Elev. (deg)		Trim AOA (deg)	
	S.A	H.A	S.A	H.A	S.A	H.A	S.A	H.A	S.A	H.A
Min. Fuel Rate	4.08	8.79	0.46	0.067	0.016	0.017	5.57	4.40	1.39	2.53
Max. L/D	4.14	9.06	0.48	0.067	0.016	0.017	5.38	3.98	1.82	2.56

Table 4.8: Vehicle Optimization - Trim Properties

Objective	S_{elev} (ft^2)		h_i (ft)		τ_L (deg)	
	S.A	H.A	S.A	H.A	S.A	H.A
Min. Fuel Rate	14.31	22.82	$\underline{1.00}$	4.96	5.20	$\overline{8.20}$
Max. L/D	11.50	24.51	$\underline{1.00}$	$\overline{5.00}$	$\underline{4.20}$	$\overline{8.20}$

Table 4.9: Vehicle Optimization - Vehicle parameters

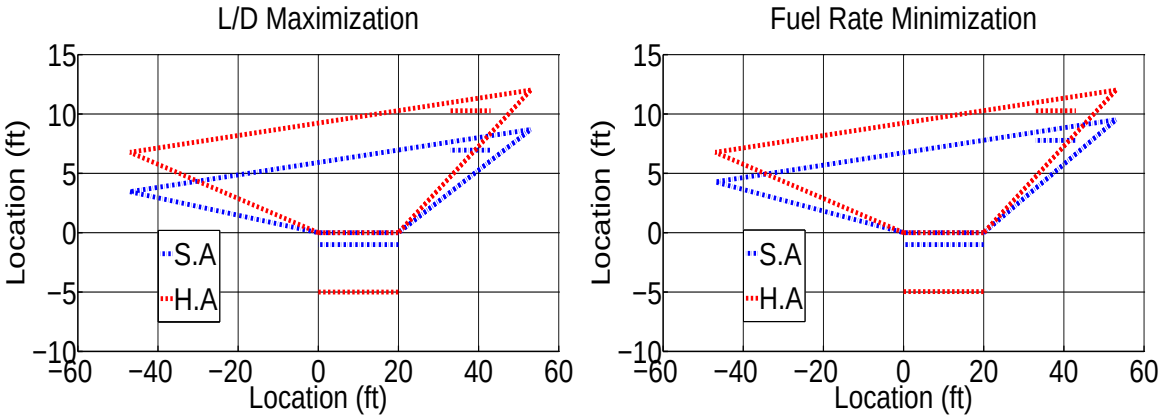

Maximize L/D Ratio Minimizing Fuel Consumption

Figure 11: Impact of Plume: Vehicle Optimization

Consider the objective of maximizing the peak lift-to-drag ratio (see Table 4.8). The plume model drastically impacts achievable performance: the vehicle with a H.A. plume model exceeds double the peak lift-to-drag ratio obtained from the S.A. model (the H.A. model often results in higher pressures along the aftbody compared to the S.A. model: the S.A. model requires the plume pressure to match the freestream pressure at the end of the aftbody).

Even when the achievable performance is similar for both plume models, the optimal vehicle designs can be significantly different. Table 4.8 shows us that the minimum fuel rate (at trim) is similar for both the S.A. and H.A. plume models. However, from Table 4.9, we observe that the vehicle configuration that achieves this minimum fuel rate varies significantly with the plume model. In the case of the S.A. plume, the optimal engine has the smallest inlet allowed, but the optimal engine inlet is close to the largest possible value when we use the H.A. plume model.

4.6 Summary

In this chapter, we presented the nonlinear equations for the hypersonic model. Some of the important features of the model are: (1) the plant is open-loop unstable, (2) the plant

exhibits non-minimum phase characteristics, (3) low frequency flexible modes also limit the available bandwidth, and (4) actuator saturation can result in instabilities.

We also observed how the exhaust impacted the vehicle static and dynamic properties. A modified numerical procedure was developed in order to model the plume more effectively than previous methods, albeit at an increase in the computational costs. This new approach enables us to effectively model the plume with high accuracy, while still being computationally tractable.

The impact of the plume model on the control architecture was presented. While a simple PI-PD control structure was sufficient for a model based on the simple plume model, a more accurate model could not be effectively controlled with such a decentralized architecture.

We considered sample vehicle design problems using two different plumes. It was observed that the achievable objectives and the vehicle designs varied significantly based on the plume models.

In the next chapter we examine the dependence of achievable performance on the linearized model of the system. We consider several control-relevant metrics and problems of interest to control designers. The impact of the vehicle design choices on these metrics is evaluated through trade studies presented in Chapter 6, helping us incorporate these metrics in an integrated design framework in Chapter 7.

5

PERFORMANCE AND CONTROL OF AIR-BREATHING HYPERSONIC VEHICLES

5.1 Overview

In this chapter, we consider several aspects of the specification-system-controller design problem. We examine how vehicle design impacts the set of achievable specifications, as well as the impact on the control design problem.

Aircraft designers often use stability derivatives to design vehicles [110]; hence we first express the linear models for the system in terms of the stability derivatives. We tie these stability derivatives directly to system performance, enabling us to obtain constraints of the stability derivatives directly in terms of the desired specifications.

In order to use the integrated system-control design framework presented in Algorithm 1, we present several common control design problems parameterized by the vehicle design parameters. These control problems are BMIs, and are included in the design problems presented in Chapter 7. In addition, the control design problems presented here are solved for various vehicle configurations in Chapter 6; we observe the following: (1) the impact of vehicle design on achievable performance, (2) the need for an integrated vehicle-control design framework for air-breathing hypersonic vehicles, (3) how vehicle design choices can be influenced early in the design stage using such analysis.

The rest of this chapter is organized as follows: we first present the linearized model of the rigid system in terms of stability derivatives in Section 5.2. In Section 5.3 we

examine how the achievable tracking performance is limited by the non-minimum phase zero of the plant. Section 5.4 we examine the impact of stability derivatives on the Null-Controllability Region. A summary and discussion of how these results are used later in this dissertation can be found in 8.1. The material presented in this chapter has appeared in [9, 11].

5.2 Model Analysis

We consider the analysis of the model in terms of its stability derivatives. In order to obtain analytic expressions for the model, we omit the flexible states, and focus on the rigid states instead. The state space representation is provided in Equation (5.1), and analytical expressions of the poles and zeros are derived from this. These are related to the control metrics in the rest of the chapter.

5.2.1 Rigid SSR

$$A = \begin{bmatrix} X_v & 0 & 0 & 0 \\ 0 & -\frac{Z_\alpha}{V_o} & \frac{Z_\alpha}{V_o} & 0 \\ 0 & 0 & 0 & 1 \\ 0 & -M_\alpha & M_\alpha & 0 \end{bmatrix}_{(x_e,\delta_e)} \qquad B = \begin{bmatrix} X_\phi & 0 \\ 0 & \gamma_\delta \\ 0 & 0 \\ 0 & M_\delta \end{bmatrix}_{(x_e,\delta_e)} \tag{5.1}$$

5.2.2 Analytical Expressions

The RHP pole can be approximated by the following expression [6]:

$$p^2 = M_\alpha \tag{5.2}$$

The NMP zero can be approximated using the following expression [6]:

$$Z_{\delta_e} z^2 - \mathscr{M}_\alpha Z_{\delta_e} + Z_\alpha \mathscr{M}_{\delta_e} X_{\delta_\phi} = 0 \tag{5.3}$$

The pole and zero have significant impact on the several closed loop metrics. The impact on the null-controllability region is examined in Section 5.4. The alignment between the pole and zero limits the achievable sensitivity, and the pole influences the bode integral 2.3. The achievable tracking performance also significantly depends on the NMP zero location. Restricting the zero location can thus be an important method to influence the performance of the vehicle.

5.3 Tracking Performance

In this section we present results showing the impact of the non-minimum phase zero on achievable tracking performance for the system. In section 5.2 we showed the relationship between the RHP zero of the system and the stability derivatives. Based on the results presented here, we can obtain constraints on the achievable performance directly in terms of the stability derivatives.

The achievable tracking performance is presented in two different frameworks: (1) a centralized optimization that attempts to design a controller and a reference, and (2) a decentralized approach that exploits ideas from vector space optimizations. The centralized approach is capable of handling complex constraints on the control law (through Youla-parameterization, for example), while being harder to solve. The vector space optimization approach, however, enables us to quickly compute the limits of achievable tracking performance but does not involve control considerations.

5.3.1 Target Tracking: Centralized

The centralized optimization for tracking a target trajectory $R(s)$ can be expressed as follows:

$$\begin{aligned} &\min_{P,K,r} 1 \\ &\text{subject to} \\ &\|R - \frac{PK}{1+PK} r\|_p \leq \delta \end{aligned} \tag{5.4}$$

where p is the norm of interest, δ is the tolerance on trajectory matching, P is the plant, K is the controller, and r is the reference signal. The constraint is nonlinear in P and K. For a fixed plant and r, we can use the Youla parameterization to formulate a convex optimization problem to minimize the tracking error.

5.3.2 Target Tracking: Decentralized

Since the constraint is on the plant output, a necessary condition for Equation (5.4) to be feasible is $d(R, P) \leq \delta$, where $d(x, T)$ represents the minimum distance between a signal x and the range of a linear operator T.

The complete decentralized optimization can be formulated as:

$$\begin{aligned} &\min_{r} 1 \\ &\text{subject to} \\ &d(R, Pr) \leq \delta \end{aligned} \tag{5.5}$$

If P is a SISO sytems with a single NMP zero at $z > 0$, we can compute the minimum achievable error from Table 5.1.

Norm	Minimum error
$\mathcal{L}^1$	$\lvert R(z)\rvert$
$\mathcal{L}^2$	$\lvert 2\sqrt{z}R(z)\rvert$
$\mathcal{L}^\infty$	$\lvert zR(z)\rvert$

Table 5.1: Limit of tracking accuracy

Consider the case of placing the elevator such that the error in tracking a signal $R(s) = 1/s/(s+1)$ is less than $\delta = 0.125^o$. The impact on the elevator location on the zero can be seen in Figure 12. Using the results in Table 5.1, we find that an zero greater than 7 is required i.e. the elevator must be atleast 87 feet from the nose.

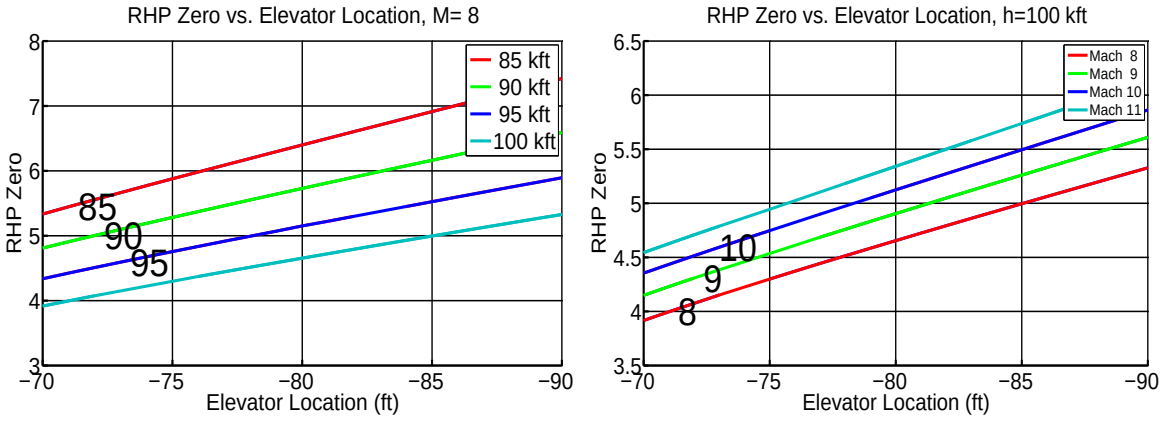

Figure 12: Right Half Plane Zero vs Elevator Location

The figures below show results from a plant, controller, and reference designed with the decentralized optimization. Based on Figure 12, a plant with an elevator 90 feet behind the nose was chosen. A controller was designed using $\mathcal{H}^\infty$ synthesis, and the reference calculated by inversion. Figure 13 shows the reference signal after model order reduction, and the resulting trajectory (with the acceptable bounds). It should be noted that the control signal is extremely large for this optimal input.

The centralized approach is capable of handling additional constraints (such as the existence of a robust controller capable of achieving specifications). If signal constraints,

such as bounds on the input signal, are incorporated, the problem can be solved by including convex constraints on the reference signal. Such an optimization is solved below using a basis for the reference.

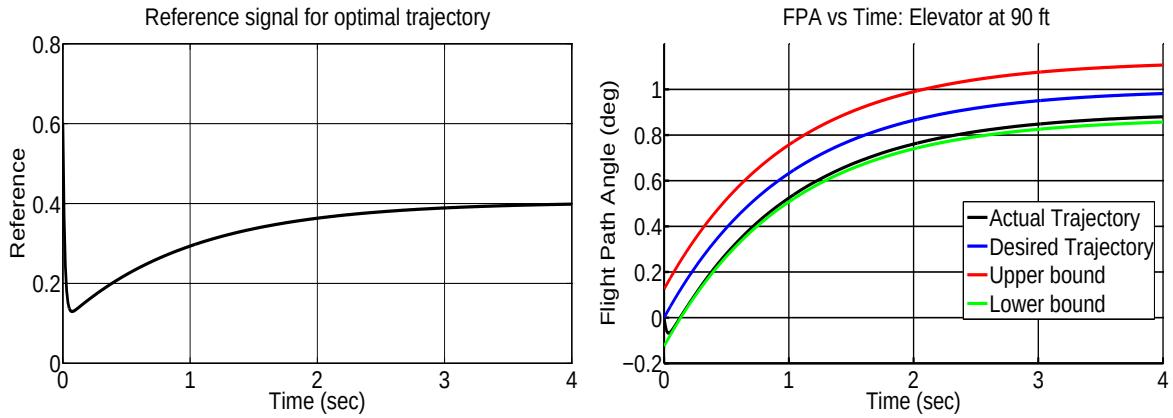

Figure 13: Reference and Achievable Trajectory ($x_{Elevator} = 90$).

5.3.3 Input constraints

Consider a desired FPA trajectory of $\frac{0.2}{s(s+0.2)}$ deg, and a maximum acceptable deviation of 0.1 deg. In addition, the elevator saturates at ± 5 degrees.

Table 5.1 lists errors for the unconstrained scenario; the zero computed from the table only serves as a lower bound. Time domain specifications on the plant output or input can be incorporated in the first stage of the centralized optimization framework. $L_1/L_2/L_\infty$ constraints can be solved efficiently using finite dimensional linear/convex programming (after an input basis is chosen).

The input basis used is $U\{k\} = \frac{(s-p)e^{-sk\Delta}}{s}$, where ($k \in \{0,\ 1,\ 2,\ \ldots,\ N\}$, and p is the unstable pole of the plant. Since all actuators possess rate limitations, such an input basis can approximate the "optimal" (continuous, infinite dimensional) input accurately

(by choice of Δ and N) due to Lipschitz (and therefore uniform continuity) constraints.

Table 5.1 indicates that the tracking error decreases with increasing NMP zeros while the optimal control increases. Reducing the NMP zero also reduces the zero-pole ratio (which is undesirable [34]). The figures below shows the achievable performance for various elevator locations in the presence of actuator limitations, and a feasible trajectory for an elevator at 90 ft.

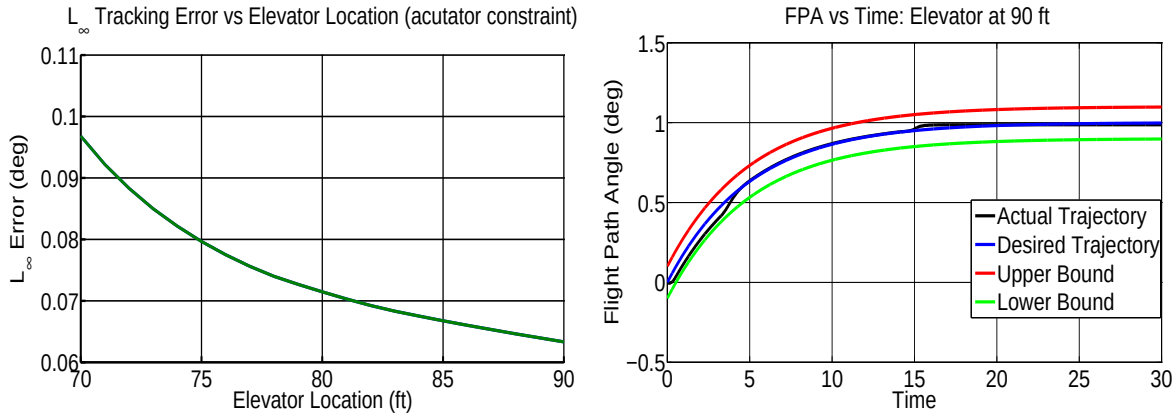

Figure 14: Tracking performance in presence of constraints.

Figure 14 shows that all elevator locations would meet the constraints, and the minimum error achievable is several times greater than the unconstrained error. Finally, the optimal error signal is not constant (unlike the unconstrained case).

5.4 Null-Controllability Regions

In this section we consider the impact of the stability derivatives on the Null-Controllability Region. The boundary of the NCR in terms of the system eigenvalues has already been explored in section 2.3. In this section the dependence of the NCR in terms of the stability derivatives is explicitly presented. The (Robust) Null Controllability Region using a

state-feedback control law (defined in Section 2.3) does not have a closed form solution; in Chapter 6 we present the results obtain numerically. The material presented in this section has appeared in several publications [11].

Robustness is defined in terms of input disturbance to output gains ($\mathcal{H}^\infty$ bounds). Additional constraints that can be formulated in our framework include: expanding holdable ellipsoids, state-to-output gains, and observer based control for nonlinear systems [46].

The trade studies in Chapter 6 include the impact of vehicle configurations on the (R)NCR with state feedback, allowing us to examine the need of incorporating control considerations early in the design phase.

5.4.1 NCR: Stability Derivatives

In order to obtain analytical expressions in terms of the stability derivatives, we ignore the flexible modes, and restrict our attention to the flight path angle states (FPA, Pitch and Pitch Rate) i.e. we consider a third order system approximated by the matrices:

$$A = \begin{bmatrix} -\frac{Z_\alpha}{V_o} & \frac{Z_\alpha}{V_o} & 0 \\ 0 & 0 & 1 \\ -M_\alpha & M_\alpha & 0 \end{bmatrix}_{(x_e,\delta_e)} \qquad B = \begin{bmatrix} \gamma_\delta \\ 0 \\ M_\delta \end{bmatrix}_{(x_e,\delta_e)} \tag{5.6}$$

The left and right eigenvectors corresponding to the unstable mode (eigenvalue = $\sqrt{M_\alpha}$) of the above A matrix are given by $v = [-\sqrt{M_\alpha}, \sqrt{M_\alpha}, 1]^T$ and $w = [0, 1, \sqrt{M_\alpha}]^T$.

We compared the resulting eigenvalues and eigenvectors against a fourth order rigid system and found the results accurate for the computations of the null controllability re-

gion. Using Equation (2.19) and given an actuator saturation level of $\bar{u}$, we have (using the notation of Section 2.3) (p represent the unstable pole of the system):

$$\lambda = \frac{M_\delta - \sqrt{M_\alpha}\gamma_\delta}{2\sqrt{M_\alpha}}\bar{u} \tag{5.7}$$

$$= \frac{M_\delta}{2p}\bar{u} - \gamma_\delta\bar{u} \tag{5.8}$$

From the above expression we see that the larger the unstable pole, the smaller the NCR; larger saturation bounds increase the NCR. In choosing the design parameters, the effect on stability derivatives can be directly related to the effect on the NCR based on the relationships above.

5.4.2 NCR: State feedback controller

The state feedback controller is parameterized as $K = YQ^{-1}$ (where Q is a symmetric positive definite matrix, and Y is a matrix), and the saturation constraint is given by $\|u(t)\|_\infty \leq \bar{u}$. If we denote the right eigenvector corresponding to the unstable mode as p, we can formulate the optimization as:

$$\max_{Q,Y,\lambda} \lambda$$
$$\text{subject to} \tag{5.9}$$

$$\begin{aligned} Q &> 0 \\ \lambda &> 0 \\ AQ + QA' + BY + Y'B' &< 0 \end{aligned} \tag{5.10}$$

$$\begin{bmatrix} 1 & \lambda p^T \\ \lambda p & Q \end{bmatrix} \geq 0$$
$$\begin{bmatrix} Q & Y^T \\ Y & \bar{u}^2 I \end{bmatrix} \geq 0 \tag{5.11}$$

Equation (5.10) is used to ensure quadratic stability of the closed loop system, while Equation (5.11) is used to ensure that the saturation constraint is not violated for the trajectory starting at λp [50].

It should be noted that the saturation bound would be violated if we move sufficiently far in the stable eigenvector directions (moving farther in the unstable eigenvector would result in the system going unstable). However, it is sufficient for stability if the unstable component of the initial state is brought to zero.

5.4.3 Robust NCR: State-Feedback Controller

In what follows, we measure robustness by the induced two-norm (from input disturbance to output). If we wish the peak not to exceed Γ, we have the following LMI (in addition to Equations (5.9), (5.10), and (5.11)):

$$\begin{bmatrix} AQ + QA^T + BY + Y^T B^T + B_w B_w^T & CQ^T \\ CQ & -\Gamma^2 I \end{bmatrix} \geq 0 \tag{5.12}$$

From the results presented in the trade studies in Chapter 6 we can observe the importance of including control considerations early in the design phase. In several cases the optimal design (from a NCR perspective) varies significantly based on whether control constraints are incorporated in the system - a larger elevator is always better when sensitivity constraints are not included; however, when sensitivity constraints are included,

the NCR is concave in the elevator size. In the next section we consider several other control metrics and their relationship to the stability derivatives.

5.5 Control Metrics

In this section we examine several metrics of interest to control designers. While these metrics were initially presented in Sections 2.2 and 2.3, we revisit the results using the model presented in Section 5.2. The impact of vehicle design choices on these metrics are considered in Chapter 6, which guides us in formulating the multidisciplinary optimization problem in Chapter 7.

5.5.1 Bode Integral

Let the sensitivity be bounded from above by the following:

$$|S(j\omega)| \quad \leq \quad -\ln s_m \qquad 0 \;<\; \omega \;\leq\; \omega_1 \tag{5.13}$$

$$|S(j\omega)| \quad \leq \quad \ln s_p \qquad \omega_1 \;<\; \omega \;\leq\; \omega_p \tag{5.14}$$

where $s_m > 1$ represents a sensitivity attenuation factor, $s_p \geq 1$ represents the peak sensitivity, ω_1 represents an effective bandwidth over which sensitivity attenuation is desired, and ω_p represents the available bandwidth [13].

Given the above, the following relationship can be derived from Equation (2.16) [18]:

$$\ln s_p \;=\; \frac{\frac{\pi}{2}\ln\left|\frac{p+z}{p-z}\right| \;+\; \ln s_m \tan^{-1}\left(\frac{\omega_1}{z}\right)}{\tan^{-1}\left(\frac{\omega_p}{z}\right) \;-\; \tan^{-1}\left(\frac{\omega_1}{z}\right)} \tag{5.15}$$

Using the expression above, we can relate the desired performance (ω_1, s_m, s_p) with system dynamics (ω_p, p, z). ω_p depends on the flexible mode frequency (we wish to avoid exciting the flexible modes; i.e. $\omega_p < \omega_{\eta,1}/2$).

5.6 Robust Control

In this section we address the issue of robustness of the control law with respect to the plume. In Section 4.5.1 we examined the impact of the plume model on control architecture. In this section, we examine how the control specifications on closed loop performance (specifically, $\mathcal{H}^\infty$ performance) impacts robustness.

In order for the plant to be robust to uncertainty, two approaches can be used:

1. Simultaneous stabilization (explicit uncertainty, additional LMI).
2. Bandwidth constraints.

In method (1), we formulate a control design problem that simultaneously stabilizes multiple plants (for example, using additional stability constraints in a state-feedback control design problem). However, this approach requires us to have explicit models for other plants that we wish to stabilize. As an alternative, we can shape the closed loop requirements and observe the impact on robustness. This is examined further below.

In Figure 15 we provide sensitivity constraints on the closed loop at the error/output of the plant through weights. As the bandwidth at the error/output is increased, the robustness properties are observed to decrease. The nominal plant is computed using the high fidelity (H.F.) approximations. The plant model using the Bolender plume is used as another model. By varying the plume between these extremes (H.F. and Bolender model), we get a

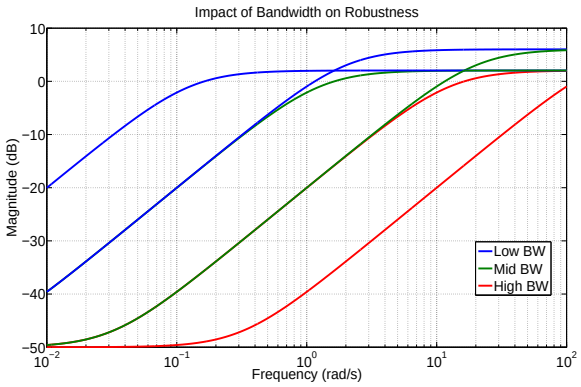

Figure 15: Sensitivity Bounds

family of plants.

It is observed that the using the low bandwidth weighting function for designing the controller for the nominal system results in a full-state feedback control law that stabilizes all plants (including the Bolender plume plant). The medium bandwidth control law only stabilizes plants midway between the H.F. and the Bolender models, while the high bandwidth design only stabilizes plants close to the H.F. model.

Such bandwidth constraints can be included in the control design formulation using Linear Matrix Inequalities.

5.7 Summary

In this chapter, we examined the limitations of performance of air-breathing hypersonic vehicles in terms of the system dynamics, as well as in terms of the stability derivatives. It was observed that design decisions can significantly impact achievable performance. A decentralized design approach illustrates how the analysis of performance limitations can influence early design decisions.

We also presented several metrics of interest to control system designers. In the next chapter we examine several vehicle configurations and the impact they have on these

control metrics. These results are used in the multidisciplinary optimization framework (presented in Chapter 3) in order to design a vehicle to execute a pull up maneuver in Chapter 7.

6

TRADE STUDIES FOR HYPERSONIC VEHICLES

6.1 Overview

In this chapter we conduct several trade studies in order to examine the impact of vehicle design choices on static and dynamic properties. The nonlinear model was presented in Section 4, and default parameter values were presented in Table 4.3. In these trade studies we vary a single parameter of the vehicle, trim and linearize the model (as described in Section 4.3), and plot the resulting properties for different operating conditions. The parameters we conduct trade studies on are:

- Elevator location (Section 6.2) and elevator size (Section 6.3).
- Engine inlet height (Section 6.4) and location (Section 6.5).
- Upper and lower nose angles (Section 6.6).
- Stiffness of the vehicle (Section 6.7).

Table 4.5 presents the time taken to trim and linearize a single vehicle configuration at a single operating point. From the table we conclude that performing a vehicle optimization using the complete nonlinear model is computationally expensive; the optimization can require hundreds or thousands of function evaluations - and each function evaluation involves trimming and linearizing the model at different operating conditions, followed by a controller design. Hence, we wish to minimize the number of function evaluations; this is achieved by approximating the vehicle properties of interest using simple polynomial

expressions. The form of the approximation is chosen based on the results of the studies presented in this chapter.

The approximations developed in this chapter are used in the integrated vehicle-control framework presented in Chapter 3 (Algorithm 1). The approximations depend on the operating condition; we use one approximation per function at each operating condition. Together with a control design optimization, we solve an integrated system-control design problem in order to address system and control considerations simultaneously.

Since the final objective of the vehicle design is to execute a pull-up maneuver, the results in this chapter focus on operating points along the expected vehicle trajectory. We focus on the properties of interest that are significantly impacted by the parameter - the complete set of figures can be found in Appendix A

The aerodynamic properties that we examine in the trade studies are:

- Drag.
- Trim controls (FER and Elevator).
- Trim angle-of-attack.

The control relevant properties that we examine in the trade studies (based on the results from Chapter 5) are:

- RHP pole, zero, and zero-pole ratio.
- Flexible mode frequencies.

- Size of the (Robust) Null Controllability Region ($\Gamma \leq 10$ in Equation (5.12)).
- RHP pole-zero alignment.

A summary of the impact of various vehicle design parameters on these properties can be found in Tables 6.1 and 6.2.

6.2 Elevator Location Trade Studies

6.2.1 Overview

In this section, we examine the impact of the elevator location on various system properties. The trade study has the following features:

- Elevator location $L_{elev} \in [65, 85]$ feet behind the nose.
- Flow separation by elevator not modeled.
- Elevator assumed to operate on free stream (no downwash).
- Changes in mass distribution neglected.

6.2.2 Results

- Figure 16: Trim AOA increases (approximately linearly), and trim drag decreases monotonically with rearward elevator.
- Figure 17: Trim FER and elevator decrease monotonically with rearward elevator.
- Figure 18: The RHP pole decreases linearly (approximately) with rearward elevator, while the NMP zero increases linearly.

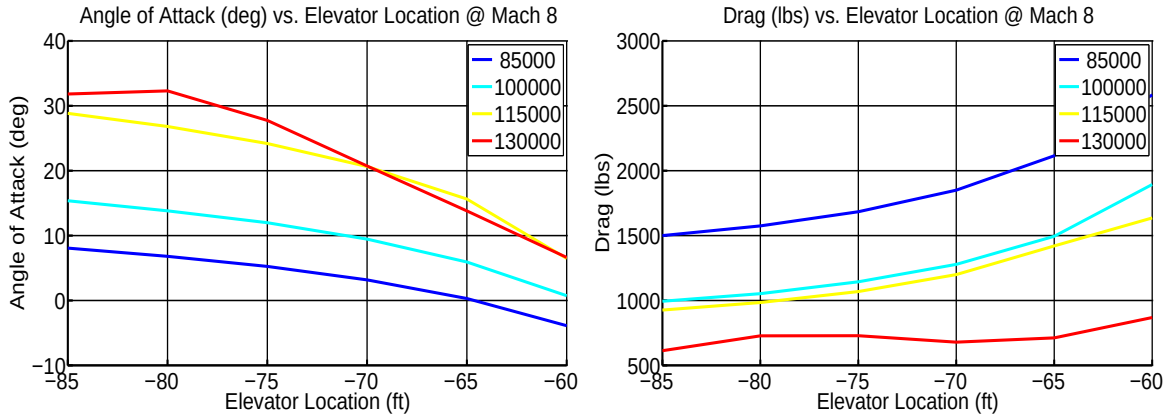

Trim AOA Trim Elevator

Figure 16: Trim AOA, Drag with Elevator Area

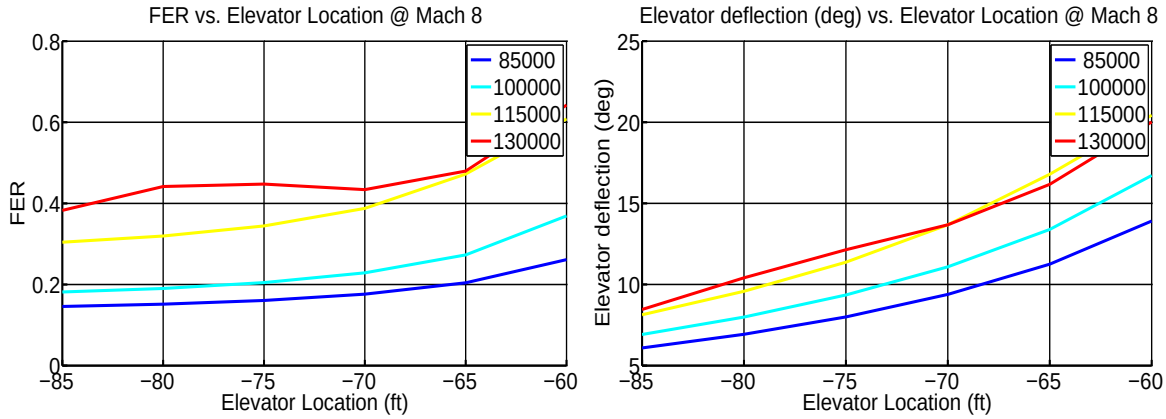

Trim AOA Trim Elevator

Figure 17: Trim FER, Elevator with Elevator Location

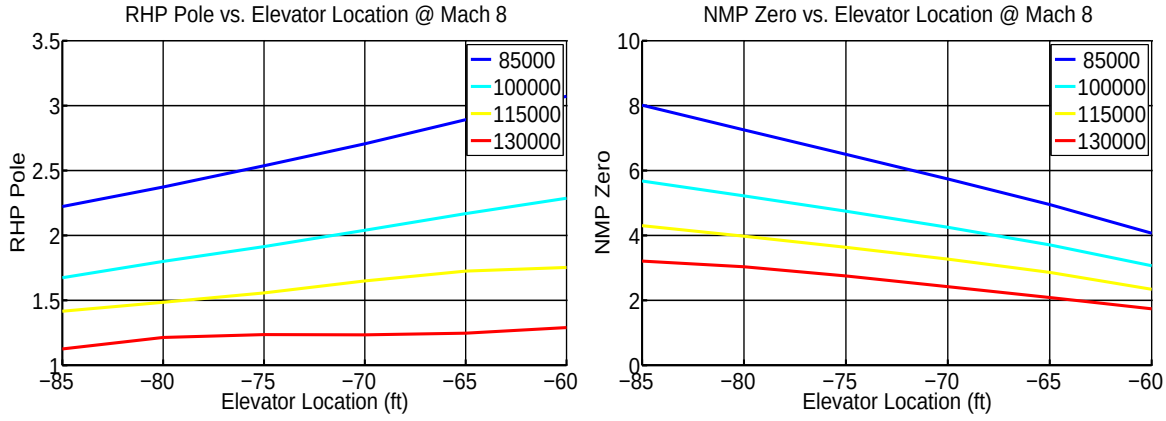

RHP Pole NMP Zero

Figure 18: Trim Pole, Zero with Elevator Location

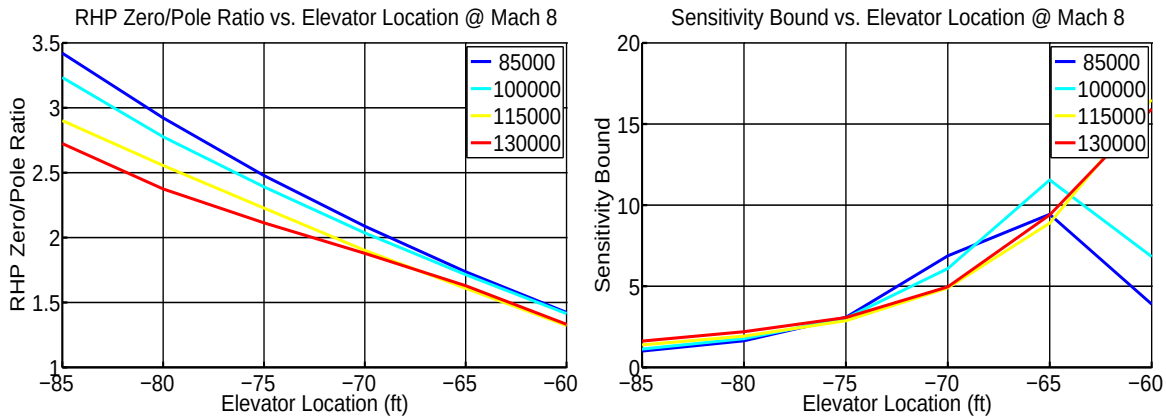

Zero-Pole Ratio Zero-Pole Ratio

Figure 19: Trim Pole, Zero with Elevator Location

- Figure 19: The Zero-Pole Ratio decreases linearly (approximately) with rearward elevator, while the minimum sensitivity achievable decreases monotonically.

6.3 Elevator Sizing Trade Studies

6.3.1 Overview

In this section, we examine the impact of the elevator area on various system properties. The trade study has the following features:

- Elevator area varied: $S_{elev} \in [8.5,\ 34]$ ft^2.
- Elevator modeled as flat plate - flow separation not captured.
- Changes in mass neglected.

6.3.2 Results

- Figure 20: Trim drag is nonlinear with elevator area, while the trim elevator deflection monotonically decreases.

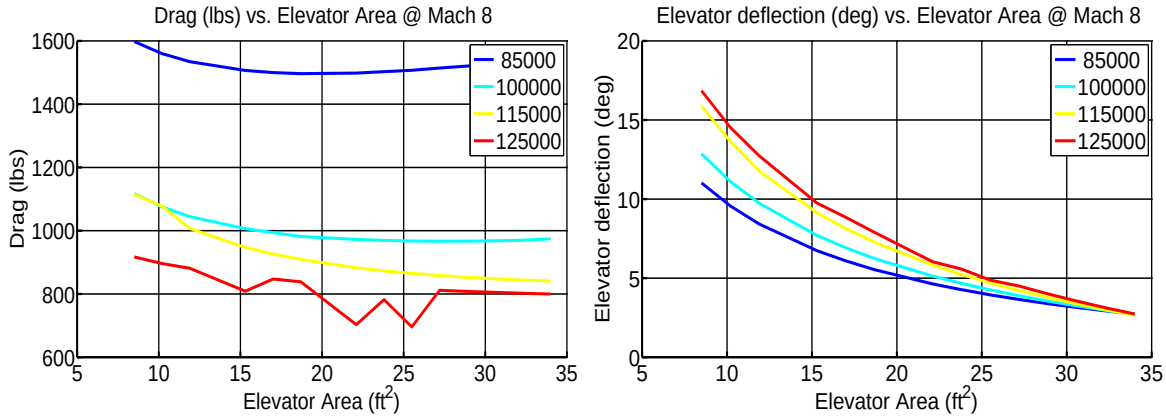

Trim Drag Trim Elevator

Figure 20: Trim Drag, Elevator with Elevator Area

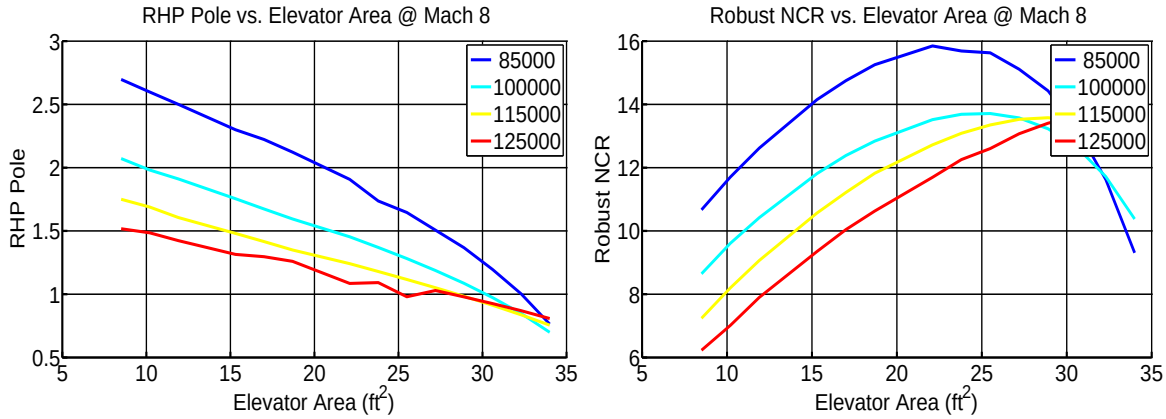

RHP Pole RNCR

Figure 21: Trim Drag, RNCR with Elevator Area

- Figure 21: The RHP pole decreases linearly (approximately) with elevator, while the RNCR is concave.

6.4 Engine Inlet Trade Studies

6.4.1 Overview

In this section, we examine the impact of increasing the engine inlet height. The trade study has the following features:

- Engine inlet $h_i \in [2, 5]$ feet.
- Shock-on-lip condition assumed.
- Engine mass assumed to scale linearly with height.

6.4.2 Results

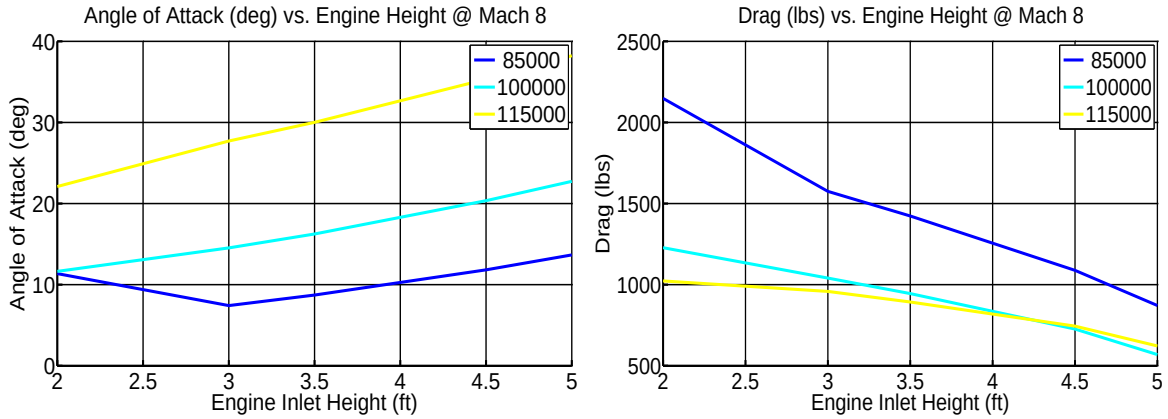

Trim AOA Trim Drag

Figure 22: Trim AOA, Drag with Engine height

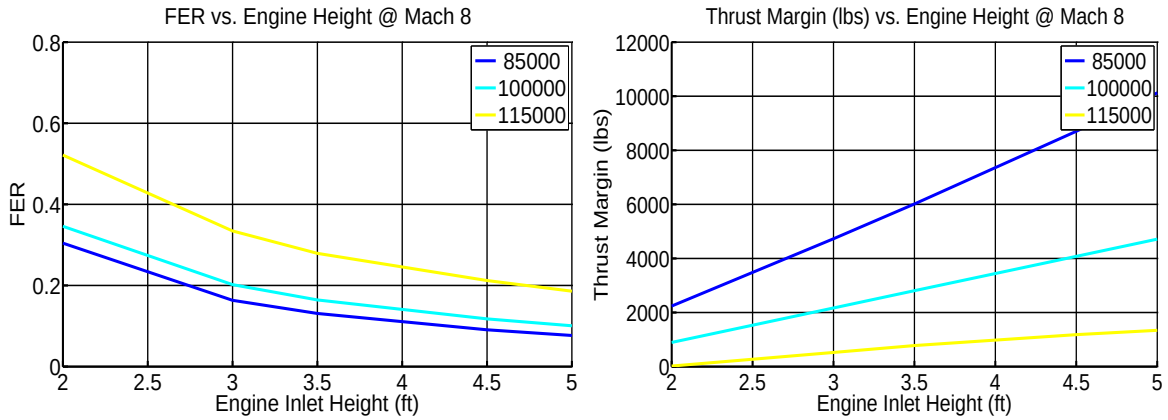

FER Thrust Margin

Figure 23: Trim FER, Thrust Margin with Engine height

- Figure 22: Trim AOA increases with larger inlets, but the drag decreases.

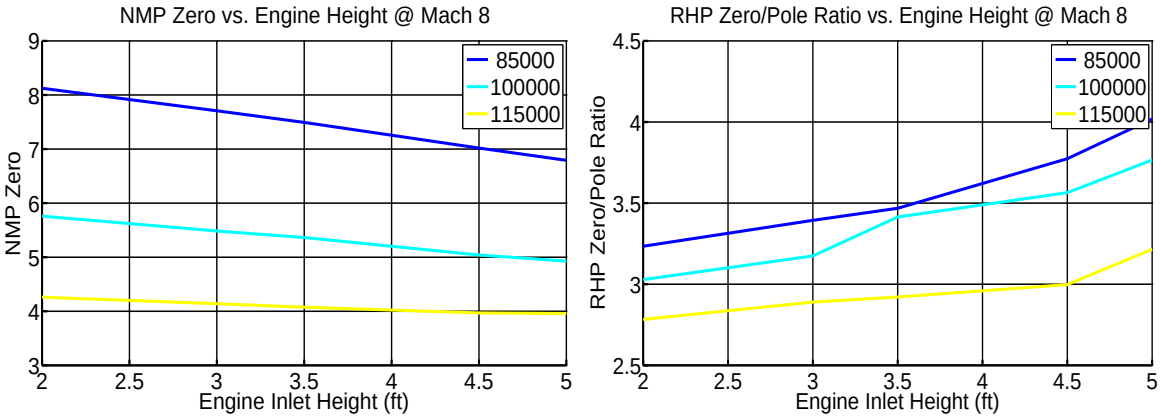

NMP Zero Zero Pole Ratio

Figure 24: NMP Zero, Zero-Pole Ratio with Engine height

- Figure 23: Trim FER decreases monotonically, Thrust Margin increases linearly with increasing inlet height.
- Figure 24: NMP Zero decreases linearly, Zero pole ratio increases with bigger inlet.

6.5 Engine Location Trade Studies

6.5.1 Overview

In this section, we examine the impact of changing the engine position. The trade study has the following features:

- Engine location $L_{eng} \in [35, 55]$ feet.
- CG shifts with change in engine.
- Two cases - fixed vehicle height (variable lower nose inclination) and variable vehicle height (constant lower nose inclination) considered.

6.5.2 Results

- Figure 25: Trim FER, Elevator increase with rearward engine.

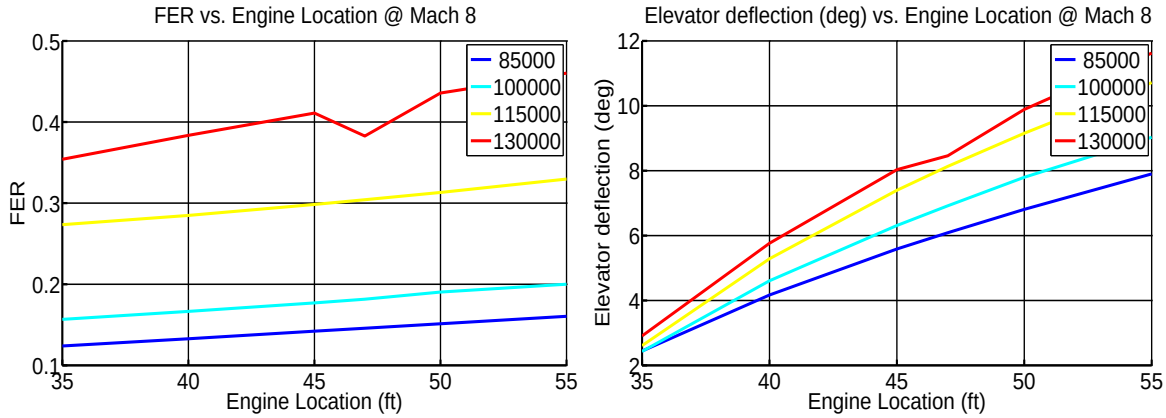

Trim FER Trim Elevator

Figure 25: Trim FER, Elevator with Engine Location

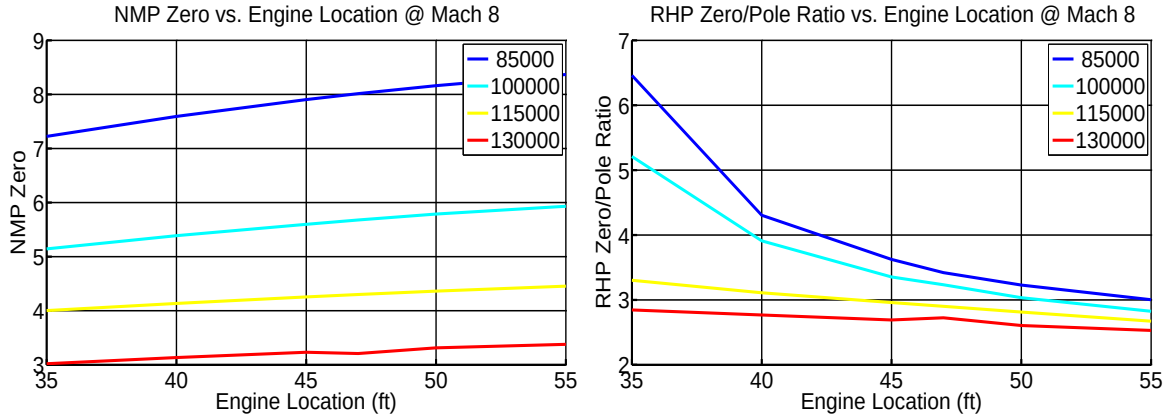

NMP Zero Zero-Pole Ratio

Figure 26: NMP Zero, Zero-Pole Ratio with Engine Location

- Figure 26: NMP zero increases, but Zero Pole Ratio decreases with rearward engine.

6.6 Nose Inclination Trade Studies

6.6.1 Overview

In this section, we examine the impact of changing the upper nose inclination. The trade study has the following features:

- Upper nose inclination $\tau_U \in [1, 5]$ deg.
- Lower nose inclination $\tau_L \in [3.2, 8.2]$ deg.

- Heating changes not considered.

- Forebody, aftbody, and engine lengths maintained; height of vehicle changes.

6.6.2 Results

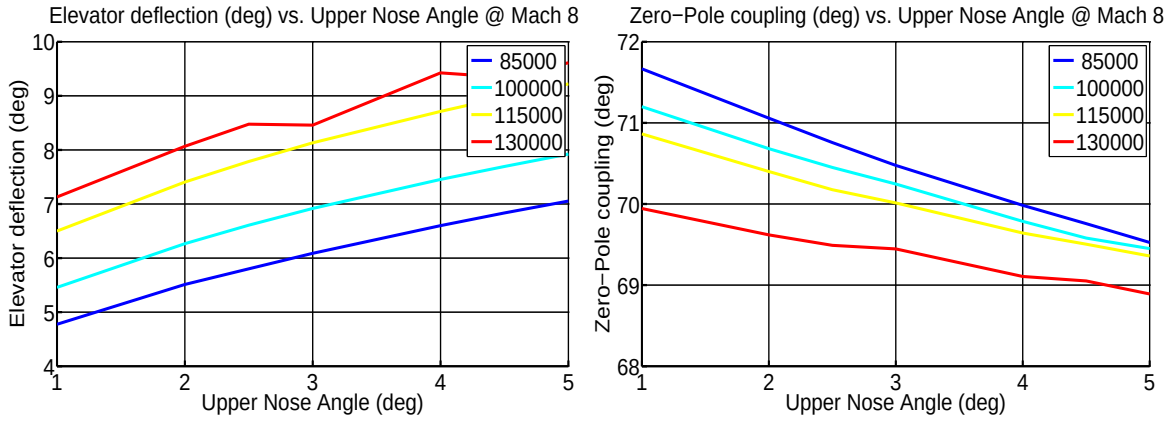

Trim Elev Pole-Zero Coupling

Figure 27: Trim Elevator, Coupling with τ_U

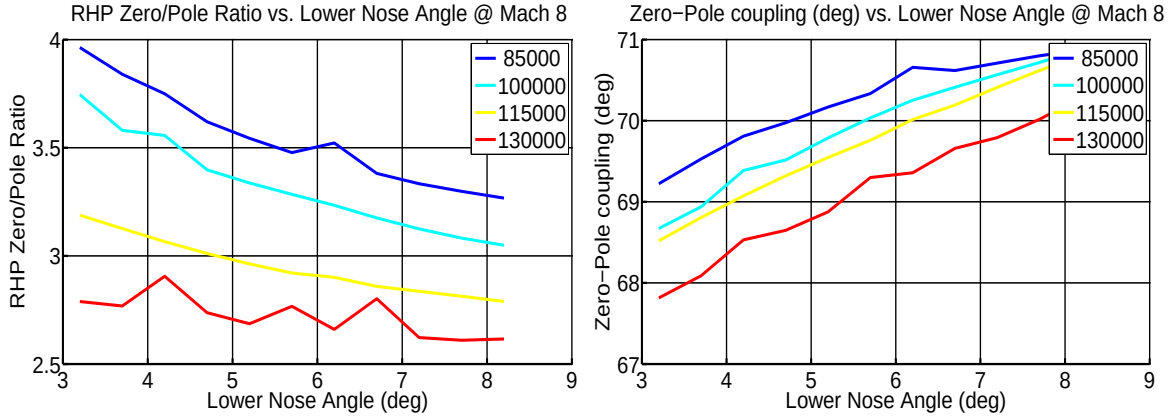

Zero-Pole Ratio Pole-Zero Coupling

Figure 28: Zero-Pole Ratio, Coupling with τ_L

- Figure 27: Trim elevator increases with τ_U, and the pole-zero coupling increases.

- Figure 28: The Zero-Pole Ratio decreases with increasing τ_L, but the coupling angle is better.

6.7 Stiffness Trade Studies

6.7.1 Overview

In this section, we examine the impact of changing the vehicle stiffness. The trade study has the following features:

- Stiffness scaling $k_{EI} \in [0.5, 2]$.

6.7.2 Results

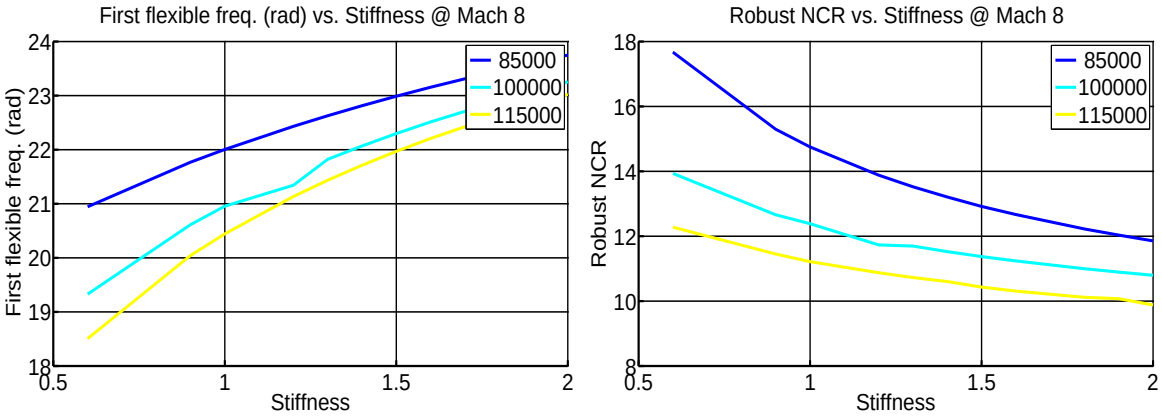

First Flexible freq. RNCR

Figure 29: Flexibility, RNCR with Stiffness

- Figure 29: Flexibility improves but RNCR decreases with increasing stiffness.

6.8 Table of Results

We summarize the results of the trade studies using the tables below. Some of the properties were not shown in this chapter for brevity - they can be found in the Appendix

A.

We summarize the results of the trade studies using the tables below. The parameters considered were:

- Elevator Location (L_{elev}) and Size (k_{Elev}).
- Engine location (L_{eng}) and inlet height (h_i).
- Upper nose inclination (τ_U) and lower nose inclination (τ_L).
- Stiffness EI.

The legend for the table is given below:

- $\uparrow$: Increases.
- $\nearrow$: Increases (almost) linearly.
- $\downarrow$: decreases.
- $\searrow$: Decreases (almost) linearly.
- $\cap$: Concave (and attains maximum).
- $\cup$: Convex (and attains minimum).
- $-$: No significant impact.

Property	AOA	Drag	FER	Elevator	FER Margin	Thrust Margin
Rearward L_{elev}	$\uparrow$	$\downarrow$	$\downarrow$	$\downarrow$	$\uparrow$	$\uparrow$
Increasing S_e	$-$	$\cup$	$\cup$	$\downarrow$	$-$	$-$
Increasing h_i	$\nearrow$	$\searrow$	$\downarrow$	$\searrow$	$\uparrow$	$\nearrow$
Rearward L_{eng}	$\searrow$	$\nearrow$	$\nearrow$	$\uparrow$	$-$	$-$
τ_U	$\nearrow$	$\uparrow$	$-$	$\nearrow$	$-$	$-$
τ_L	$\searrow$	$-$	$\searrow$	$\nearrow$	$\searrow$	$-$
Increasing EI	$\nearrow$	$-$	$-$	$-$	$-$	$-$

Table 6.1: Impact of parameters on static vehicle properties

Property	RHP Pole	NMP Zero	Z/P Ratio	Sensitivity Bound Bound	Zero-Pole Coupling
Rearward L_{elev}	$\searrow$	$\nearrow$	$\nearrow$	$\downarrow$	$\downarrow$
Increasing S_e	$\searrow$	$-$	$\uparrow$	$\downarrow$	$\downarrow$
Increasing h_i	$\searrow$	$\searrow$	$\uparrow$	$\downarrow$	$\downarrow$
Rearward L_{eng}	$\uparrow$	$\nearrow$	$\downarrow$	$\uparrow$	$\uparrow$
Increasing τ_U	$\nearrow$	$\nearrow$	$\downarrow$	$\nearrow$	$\nearrow$
Increasing τ_L	$\nearrow$	$\nearrow$	$\downarrow$	$\nearrow$	$\searrow$
Increasing EI	$\uparrow$	$-$	$\downarrow$	$\uparrow$	$\downarrow$

Table 6.2: Impact of parameters on dynamic vehicle properties

6.8.1 Static Properties

Table 6.1 lists the impact of vehicle design decisions on the static properties of the vehicle. The trends are listed at trim.

The first flexible mode frequency increases linearly with EI; the other parameters do not significantly impact it.

6.8.2 Dynamic Properties

The dynamic properties of the trade studies is given in Table 6.2. It should be noted that a decrease in coupling between the pole and zero is achieved through an increase in the angle between the pole and zero directionality.

6.9 Summary

In this chapter, we examined several trade studies in order to explore the impact of design configurations on the static and dynamic properties of the system. These allow us to examine which parameters to include in the vehicle optimization, as well as how to obtain approximate expressions for the analytical models.

The results of these trade studies are incorporated in the multidisciplinary optimization framework presented in the next chapter.

7

MULTIDISCIPLINARY OPTIMIZATION OF AN AIR-BREATHING HYPERSONIC VEHICLE

7.1 Overview

In this chapter we examine an integrated vehicle-control design problem based on the methodology presented in Chapter 3. The objective is to design a vehicle to perform a pull-up maneuver as illustrated by Figure 30. Towards this goal, we would like to incorporate both control-relevant and system design metrics into the design procedure in order to reduce the design time and improve the properties of the system.

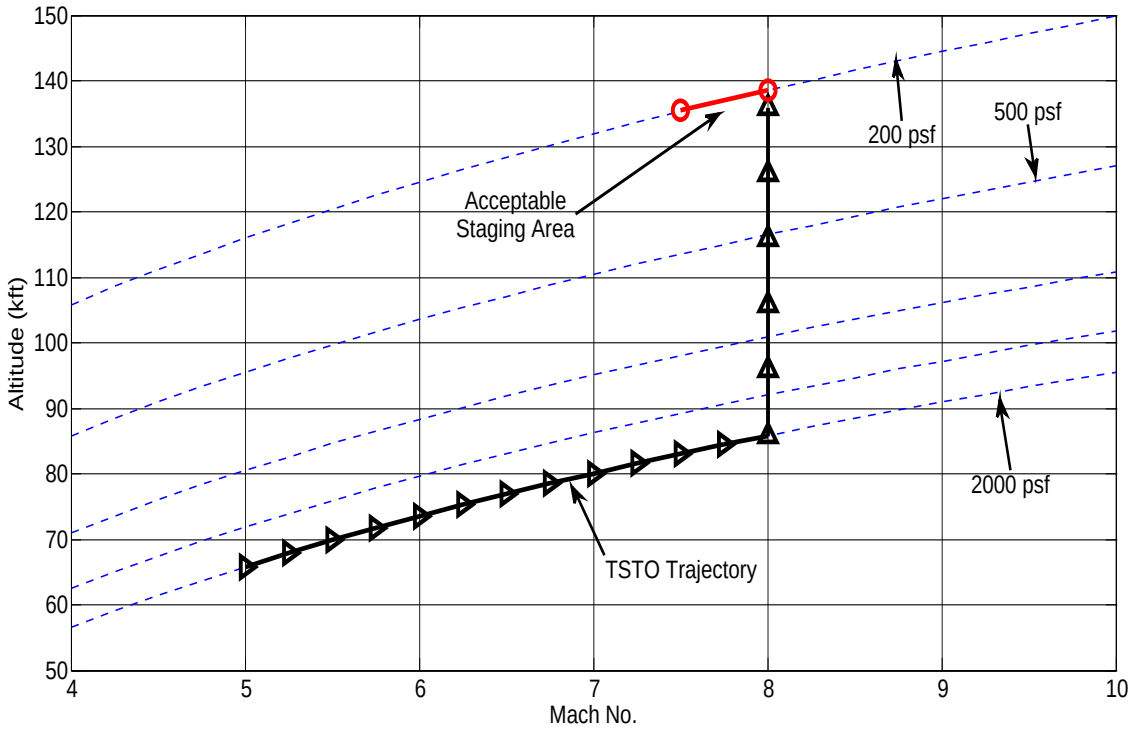

Figure 30: Pull-Up Maneuver

In chapter 4 a nonlinear model of an airbreathing hypersonic vehicle was presented. There are significant trade-offs associated with vehicle design choices, as shown in chapter 6. Based on the result of the trade studies, we obtain approximations for the vehicle static and dynamic properties in terms of the vehicle design parameters. These approximations are used in the integrated design framework to guide the optimization to a desirable vehicle design. We also include system-dependent control constraints through Bilinear Matrix Inequalities (BMIs), as described in Section 2.2.4.

The rest of this chapter is organized as follows: in Section 7.2 we consider the conventional vehicle design approach. An overview of the type of problems that can be addressed (along with numerical algorithms) in the multidisciplinary optimization framework is considered in Section 7.3. Several vehicle design problems are considered next, and the results of this chapter are summarized in Section 7.6.

7.2 Conventional Vehicle Design Process

In [111] the author lists the stages involved in the design of an aircraft. The stage of interest in this dissertation is the conceptual design phase. The main objectives of this phase can be summarized by the following questions:

- Does the vehicle design meet specifications?
- Is this design the optimal design for meeting specifications?

The objective of the conceptual design phase is to come up with a design that is close to the optimal vehicle configuration. In the next phase (known as the preliminary design phase), the conceptual design is tested with advanced simulation methodologies (such as computational fluid dynamics) in order to improve the design. Since these advanced

methods are computationally intensive, we would like to come close to the optimal design in the conceptual phase - if a major redesign is required in the preliminary design phase, it is considered to be a failure of the conceptual design [111].

The conceptual phase can be broken down into the following (iterative) process, considered to be the ”intellectual pivot points” [111] of the design procedure.

1. Formulate requirements such as range, cost, maximum load factor, and size.
2. Obtain a preliminary estimate of the vehicle weight.
3. Identify critical performance metrics such as peak lift coefficient, lift-to-drag ratio, thrust-to-weight ratio.
4. Plan the vehicle layout based on the performance metrics, weight, and requirements.
5. Obtain a more accurate weight estimate from the layout.
6. Analyze the vehicle performance (if it is not satisfactory, go back to step 3).
7. Optimize the design while maintaining (or improving) performance.

In this work, we include several control relevant metrics into the design process. Due to the complex design and stringent constraints involved in designing air-breathing hypersonic vehicles, excluding these metrics can lead to solutions that are optimal (from an aerodynamic point of view), while being difficult or impossible to control to specifications. The objective of the multidisciplinary optimization process is to (a) incorporate several different performance metrics into the system design, (b) reduce the number of iterations before converging to an acceptable design.

We make use of the trade studies performed in Chapter 6 to obtain approximate expressions relating design variables to the pivot points listed above. These approximate expressions are used in a the integrated system-control design framework. We now examine several vehicle optimization problems.

7.3 Design Formulation

In this section we consider the components of the vehicle design problems. Since the final objective of the mission is based on the trajectory in Figure 30, we must include several different operating points in the design formulation. In addition, we bound aero-centric and control-centric properties based on the intellectual pivot points listed in the previous section.

7.3.1 Operating Points

We execute a pull-up maneuver at Mach 8 from an altitude of 85,000 feet to 120,000 feet; we linearize at a subset of the dynamic pressures. Specifically, we use five dynamic pressures in the interval [2000, 200] psf.

7.3.2 System Specifications

We can include the following aero-centric specifications in the framework:

- Weight.
- Drag.
- Range.
- Volumetric specifications.

- Trim fuel and elevator.

The system specifications are included through polynomial approximations based on the results of the trade studies. For example, the drag is assumed to vary quadratically with the elevator area (based on Figure 20).

7.3.3 Control Metrics

We include the following control-relevant specifications in the framework:

- Weighted Sensitivity bounds.
- Saturation bounds.
- Tracking metrics.
- Bandwidth (pole to flexible mode).
- Zero-Pole ratio and coupling.

We use a state-feedback control law (parameterized as described in Chapter 2) to compute several of the metrics listed above. These parameterizations allow us to formulate the bounds as convex optimization problems (for a fixed vehicle configuration). When the state space model of the plant is affine in the design parameters, the metrics are computed through BMIs.

7.3.4 Design parameters

We include the following design parameters in our vehicle design optimization:

- Elevator area S_e.
- Engine inlet height h_i.
- Upper (τ_U) and lower (τ_L) nose angles.
- Stiffness factor EI.

7.3.5 Coupling

We briefly discuss how each of the aero/control metrics are significantly impacted by the design variables. This illustrates the coupling between the parameter choices. The impact considered here are approximations, since they are based on single-parameter trade studies. However, they might help simplify the optimization in a decentralized MDO framework by highlighting the coupling between constraints.

- Flexibility: Stiffness
- Volume: Nose angles
- Weight: Stiffness, Engine height
- Drag: Elevator area, Nose inclination

7.3.6 Problem Formulation

We attempt to find a vehicle design that satisfies the specifications across the entire flight trajectory. Some of the specifications are specified at each operating point (such as drag, trim elevator and fuel, tracking metrics), since these properties are strongly dependent on the operating point.

Since we are using several fixed operating points to design the vehicle, each operating point must lie in the null controllability region of its neighbor; if this condition was violated, the linearized vehicle would not complete the trajectory due to saturation constraints.

7.3.7 Numerical Procedures

In Table 4.5 we observed that the time to trim the vehicle at a single operating point is extremely high. As a result we would like to minimize the number of function evaluations. In Algorithm 1, an inner optimization is solved using approximations to the plant properties (Line 5). The approximants are constructed using the exact plant properties (computed on the vertices of a simplex). In each successive iteration, the approximations are refined based on the solution of the inner optimization. We discuss several approaches to solving the inner optimization below:

Bilinear Matrix Inequalities (BMI)

The inner approximation is formulated as a constrained optimization over the design parameters using polynomial inequalities and control relevant BMIs. A BMI solver, such as PenBMI, is capable of handling such problems. Details of the BMI algorithm can be found in [112]. Global optimization can be performed using a branch-and-bound approach.

Sequential Quadratic Programming (SQP)

The inner optimization can also be solved using a SQP solver like NPSOL. In this case, the gradients are computed using the approximations to the system (since the exact function evaluations are slow).

Pattern Search (PS)

A derivative free approach to solving the inner optimization is to use a pattern search or direct search methodology. Such an approach can involve several evaluations of the approximate function at each step in order to find the best direction.

For each algorithm, we compare the solution, the time for computation, and the number of iterations required. The number of iterations refer to the number of times the original simplex was partitioned due to the original approximation being inadequate to obtain a solution to the exact problem. Since we are using an approximation to the actual system, the solution from the optimization procedure must be verified; the computation times listed in this chapter includes the verification (involving the linearization of the model for the design values).

In the next section we present several optimization problems of the hypersonic vehicle. We compare the results obtained from the various optimization procedures.

7.4 Illustrative Design Examples

In this section we consider several different vehicle optimization problems and present the results of the design process and resulting vehicle. These problems serve to highlight the capabilities of Algorithm 1, while still being fairly simple.

7.4.1 Elevator Area: RHP Pole

We first consider a vehicle design problem attempting to constrain a single dynamic property of the vehicle using one design parameter. This example is used to examine the performance of various optimization procedures used to solve the inner optimization problem in Algorithm 1 at a single operating point.

Problem Statement

In this example, we consider a RHP pole (p) constraint of $1 \leq p \leq 2$ at Mach 8, 85kft. We use a single design parameter (the elevator area $S_e \in [8.5,\ 34]$ ft^2) to modify the pole location. From Figure 21 we observe that any elevator area greater than 20.5 ft^2 and less than 32.3 ft^2 is an acceptable solution.

Problem Formulation

The initial plant simplex consists of two plants computed at the vertices of the design set i.e. at the elevator area of 8.5 ft^2 and 34 ft^2. It should be noted that neither vertex is a feasible solution of the optimization problem. We use a linear approximation for the plant at the two vertices, and a linear approximation to the pole (based on the trade studies). If we denote the linear approximation to the pole location by $\hat{p}(x) = 3.668 - 1.3339x$, and affine approximation to the plant by $\hat{P}(x) = [\hat{A}(x),\ \hat{B}(x),\ \hat{C}(x),\ \hat{D}(x)]$ (where x is the elevator area), we have the following optimization problem:

$$\min_x \delta(x) \tag{7.1a}$$

subject to

$$\delta \leq 0 \tag{7.1b}$$

$$\delta \geq 1 - \hat{p}(x) \tag{7.1c}$$

$$\delta \geq \hat{p}(x) - 2 \tag{7.1d}$$

$$\hat{A}Q + Q\hat{A}^T + \hat{B}Y + Y^T\hat{B}^T < \epsilon I \tag{7.1e}$$

$$Q > 0 \tag{7.1f}$$

$$\epsilon \leq 0 \tag{7.1g}$$

where Q is a symmetric matrix. The dependence of $\hat{A}$ and $\hat{B}$ on the parameter x was omitted in the equations above for brevity.

Equations (7.1c) and (7.1d) are used to provide robustness to errors in the linear approximation, while Equations (7.1e)-(7.1g) are constraints to ensure that the closed loop is stabilizable. If we only considered Equations (7.1a)-(7.1d), we have a linear programming problem. For a fixed x, Equations (7.1e)-(7.1g) are LMIs (convex constraints).

When optimizing using NPSOL, we do not need to use $\hat{p}(x)$ as an approximation to the plant pole; the RHP pole of the approximate plant could be computed using the eigenvalue of $\hat{A}(x)$. It is observed that this is a better approximation to the pole; the results are presented as NPSOL(b) in Table 7.1.

Results

Table 7.1 shows the solution and computation time for the problem above using the three optimization approaches considered in this work (the BMI, SQP, and PS algorithms). In Table 7.1 the BMI, SQP, PS optimizations refer to the optimization in Equations (7.1) (based on the linear approximation to the plant pole $\hat{p}(x)$), while SQP(b) computes the RHP Pole using eigenvalue of the affine plant matrix $\hat{A}(x)$.

Property	BMI	SQP	SQP(b)	PS
Solution S_e (ft^2)	27.63	27.63	29.94	30.05
Cost (approximate)	-0.5	-0.5	-0.5	-0.5
Cost (actual)	-0.27	-0.27	-0.49	-0.51
Time (sec)	37.48	102.17	146.95	213
Iterations	1	1	1	1

Table 7.1: Solution: Elevator area design with RHP pole bounds

- The BMI optimization performs better than the alternatives in this example.
- SQP(b) is more robust (as it is computing the eigenvalues directly) to errors in approximation.

Since SQP(b) is more robust to approximation errors, it tends to converge to a solution in fewer simplex partitions than the MDO approach.

7.4.2 Elevator Area, Engine Height: Multidisciplinary Optimization

We next consider a multidisciplinary optimization problem involving multiple operating conditions, multidisciplinary requirements (guidance, aerodynamic, and control constraints), and multiple design parameters.

Problem Statement

In this example we attempt to design the elevator area and engine inlet of the vehicle to address the following aero and control objectives:

- Operating points: Mach 8, 85 and 95 kft.
- Drag less than 1500 lbs. at cruise (Mach 8, 85kft).
- $\mathcal{L}^\infty$ tracking error of no more than 1^o when tracking a FPA command of $\frac{0.6}{s+0.6}$.
- Elevator deflection less than 15^o for a FPA command of 1^o deg.
- Design variables: Engine height ($h_i \in [2,\ 5]$ ft)and elevator area ($S_e \in [8.5,\ 34]$ ft^2).

Problem Formulation

The constraint on the $\mathcal{L}^\infty$ tracking error of no more than 0.1^o when tracking a reference signal $\frac{0.6}{(s+0.6)}$ translates to a zero of (approximately) no less than 6 (using results from Table 5.1). Since the zero varies with the flight condition, this constraint must be verified at all operating points. Since we would like to move from one operating point to the next while satisfying saturation constraints, we use Equation 2.12 to meet saturation bounds ($x_o = [-0.531, -1, 0, 0]^T$ which represents the climb to 95 kft using a FPA of 1^o). The drag is modeled as a quadratic function of the elevator area, and linear function of the engine inlet height.

Results

Table 7.2 shows us the results of the vehicle design optimization. While the SQP approach used less iterations overall (i.e. less trimming of the vehicles), it took approximately 30% more time to arrive at a feasible solution compared to the BMI approach. The pattern search method was the slowest, but still required one less iteration than the BMI approach.

Property	BMI	SQP	PS
Solution S_e (ft^2)	32.74	22.84	32.74
Solution h_i (ft^2)	4.07	3.83	4.07
Time (min)	24.38	31.27	91.12
Iterations	22	18	21

Table 7.2: Solution: Elevator Area and Engine Height design with Multidisciplinary constraints

7.4.3 Elevator Area: Control-Relevant Design

In this design problem we consider a variation on a classical control design problem - generating an LPV $\mathcal{H}^\infty$ control system design using a weighted $\mathcal{H}^\infty$ mixed sensitivity criteria. We consider two different scenarios: (1) No saturation constraints, and (2) Saturation constraints included. The saturation conditions allow us to ensure that each

operating point is in the Robust Null-Controllability Region of its neighbor. In the absence of saturation conditions, a high gain control can be used to improve the $\mathcal{H}^\infty$ norm, while being infeasible due to actuator limitations. The saturation constraints help us examine the performance achievable with more conservative control laws.

The weighted $\mathcal{H}^\infty$ suboptimal mixed sensitivity problem is to find a real-rational (finite-dimensional) proper internally stabilizing controller K that satisfies

$$\|T_{wz}\|_{\mathcal{H}^\infty} = \left\| \begin{bmatrix} W_1 S \\ W_2 K S \\ W_3 T \end{bmatrix} \right\|_{\mathcal{H}^\infty} < \gamma. \tag{7.2}$$

where S and T are the sensitivity and complementary sensitivity transfer functions of the closed loop system respectively.

As the order of the weighting functions increase, the number of variables required to parameterize the controller increases. In order to keep the number of variables within reasonable bounds, we use a static gain for the weights on the control and the complementary sensitivity.

Problem Statement

We consider a vehicle moving through four different operating points at Mach 8: 85kft, 95kft, 105kft, and 115kft. We use the same weight functions for all operating conditions. The objective is to find an elevator location so that $\|T_{wz}\|_{\mathcal{H}^\infty}$ is small, while meeting saturation constraints (if any). While the NMP zero is not impacted by the elevator area (i.e.

the achievable norm of T_{wz} is not significantly impacted by the choice of elevator size in the unconstrained case), the elevator effectiveness increases with area.

Problem Formulation

The weighting functions for $\mathcal{H}^\infty$ design are given as follows:

$$W_1^{i,j} = \begin{cases} \frac{s/\sqrt{M_{e_i}}+\omega_{e_i}}{s+\omega_{e_i}\sqrt{\epsilon_{e_i}}} & i=j \\ 0 & i\neq j \end{cases} \tag{7.3}$$

$$W_2^{i,j} = \begin{cases} \frac{1}{M_2^{i,j}} & i=j \\ 0 & i\neq j \end{cases} \tag{7.4}$$

$$W_3^{i,j} = \begin{cases} \frac{1}{M_3^{i,j}} & i=j \\ 0 & i\neq j \end{cases} \tag{7.5}$$

$$\tag{7.6}$$

Weighting function parameters are selected as given in Table 7.3.

	W_1		W_2		W_3	
	1	2	1	2	1	2
ϵ	10^{-5}	10^{-5}	-	-	-	-
M	1.6	4	20	20	2	2
ω	.0395	0.25	-	-	-	-

Table 7.3: Weight transfer function parameters for $\mathcal{H}^\infty$ mixed-sensitivty optimization

In order to impose saturation constraints (1 on the FER, and 15^o on the elevator deflection), we use Equation (2.12). The initial state $x_o = [-\Delta V, -1, 0, 0]$ represents the change in velocity between the equilibriums, while climbing at an FPA of 1^o.

Results

For this example we examine the difference in the solution due to the introduction of saturation constraints. Figure 31 shows the different in sensitivity transfer function without and

with the saturation constraint (for all four operating points). Table 7.4 lists the corresponding design solutions as well.

Property	Without Saturation	With Saturation
Solution S_e (ft^2)	22.44	34
Computation Time (sec)	125.04	182.24
Peak γ (dB)	-2.04	5.22

Table 7.4: Solution: Elevator area design with RHP pole bounds

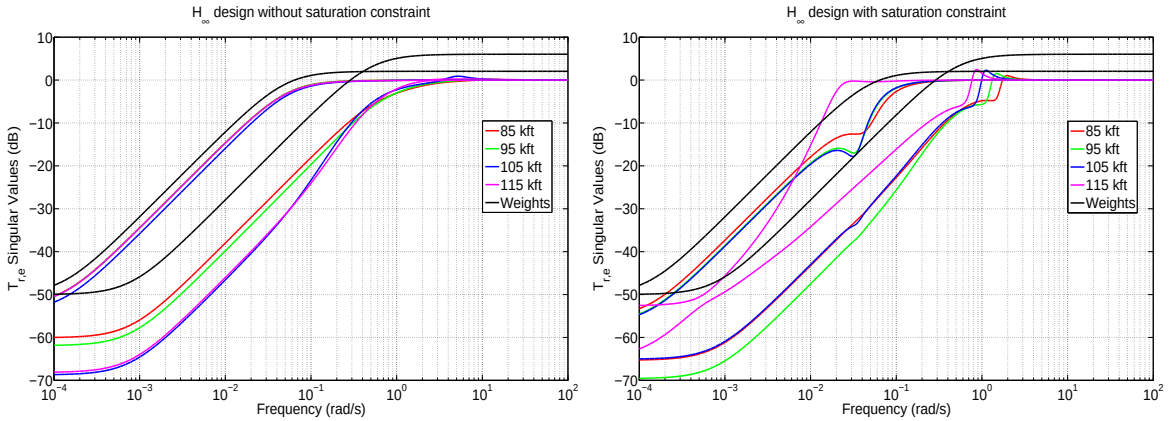

No Saturation Saturation Constraint

Figure 31: $\mathcal{H}^\infty$ design without and with saturation

7.5 Pull-Up Maneuver Design: Multidiscplinary Optimization

In this section we look at a comprehensive example problem involving the design of the vehicle to execute a pull up maneuver from 85kft to 120kft at Mach 8. We use multiple aero and control relevant constraints in this design problem. Once a satisfactory vehicle design is obtained, we utilize

7.5.1 Design Parameters

We use the following design variables for this problem:

- Elevator area.
- Engine height.

- Stiffness.
- Lower nose angle.

7.5.2 Constraints

We have the following aero constraints on the system design:

- Mass: Less than 1.3 times nominal design.
- Drag: Less than 1500 psf at trim.
- Volumetric: More than 80% of nominal.

The following control design constraints are incorporated:

- Elevator saturation: 15^o.
- Weighted Sensitivity.
- Flexible Mode: More than 23 rad/s.

Finally, we use the following performance specification for the system:

- Tracking Error: Less than 10% percent tracking error to $\frac{\tau(h)}{s(s+\tau(h))}$, where $\tau(85\ kft) = 0.6$, $\tau(95\ kft) = 0.5$, $\tau(105\ kft) = 0.4$, $\tau(115\ kft) = 0.3$.

Problem Formulation

This section presents LPV $\mathcal{H}^\infty$ control system designs using a weighted $\mathcal{H}^\infty$ mixed sensitivity criteria.

The selection of the weighting functions used in the $\mathcal{H}^\infty$ design process was kept consistent across the operating points. Using the same weighting function structure for each design keeps the order of the controllers the same and allows for interpolation of the weighting function parameters across the gain-scheduled conversion. The weighting functions, however, increase the order of the system and therefore increases the complexity of the problem formulation (the state-feedback controller dimensions increase, which requires additional terms to parameterize the controller). The weights used are those given by Equation (7.3) and Table 7.3.

Results

The vehicle design resulting from the integrated design framework results in the following solution:

- Elevator Area: 29.06 ft^2.
- Engine height: 3.6629 ft.
- Nose Inclination: 6.62^o.
- Stiffness: 1.9919.

The system has the following closed loop properties:

- Mass: 1.24 times nominal.
- Volume: 86.45% of nominal.
- NMP Zeros: Satisfied.
- Flexible Mode: Minimum = 23 rad/s (115 kft).

In figure 32 we observe the pull-up maneuver using the resulting design.

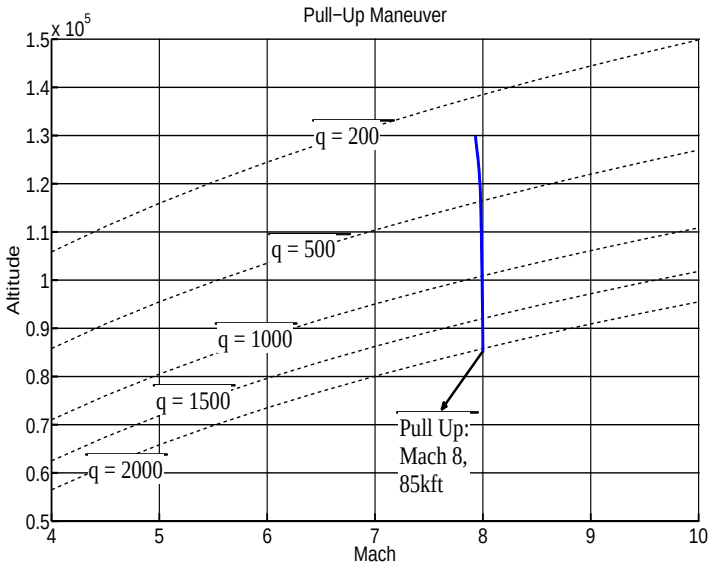

Figure 32: Pull Up maneuver

7.6 Summary

In this chapter we considered several multidisciplinary optimization problems involving aero and control constraints. We considered the performance of the integrated system-control design framework presented in Chapter 3 using multiple approaches for solving the (inner) approximate optimization.

The integrated system-control design methodology was shown to be capable of handling several common control and system design constraints simultaneously. By using an affine approximation for the plant, LMI control constraints, and polynomial approximations for aerodynamic properties, the multidisciplinary optimizations were formulated as BMIs. The computational advantage of using a BMI-specific optimizer was demonstrated by comparing the evaluation time with other nonlinear optimization algorithms.

The use of approximations helped reduce the number of exact function evaluations significantly, improving the computation time required to arrive at a feasible design. This is of importance when the exact function evaluation can be extremely expensive (as in this application). Coupled with simultaneous optimization at multiple operating points, the design and control of a nonlinear system was addressed handled in this multidisciplinary optimization framework.

8

SUMMARY & FUTURE WORK

8.1 Summary

In this work we presented a bilinear matrix inequalities (BMI) based approach to a multidisciplinary optimization problem in order to integrate system and control design. The capabilities of the framework, as well as its limitations, were examined.

The control-relevant design of an air-breathing hypersonic vehicle was considered as an example problem. Such systems are unstable, non-minimum phase, have low frequency flexible modes, and nonlinear (due to saturations and variations in operating environments). Improvements to the standard model were developed, and the importance of accurate modeling of the vehicle exhaust plume was illustrated. In addition, we analyzed the trade-offs associated with various vehicle design configurations; these trade studies were used to formulate approximations of the system properties in the integrated design algorithm.

In order to optimize the vehicle within the integrated system-control design framework the impact of vehicle design choices on system and control metrics were approximated using polynomials. These approximations were used to constrain the search space, while being refined in an iterative optimization process. This multidisciplinary optimization was used to design a vehicle to perform a pull-up maneuver, and the properties of the resulting vehicle was analyzed.

8.2 Future Work

Directions of future research are categorized into three main topics:

Modeling of Hypersonic Vehicles : There are several directions of research on the modeling of scramet powered-hypersonic vehicles; the list below is not meant to be comprehensive.

- Improved model of the plume/aircraft with CFD validation.
- Designing the aftbody from a control perspective.
- Improved engine model.
- Modeling flow separation on lifting surfaces.

Control-Relevant Design : We list some control relevant research directions below:

- Design the vehicle for decentralized control law.
- Incorporate complex control constraints in predicting performance limitations.
- Incorporating parameteric/modeling uncertainty explicitly in the vehicle design.

Multidisciplinary Optimization : Some directions of research in multidisciplinary optimization are:

- Analyzing the properties of the algorithm for integrated system-control design.
- Imposing a structure/constraints on the controller in a numerically efficient manner.
- Incorporating uncertainty in the framework through BMIs.

REFERENCES

[1] A. Rodriguez, J. Dickeson, O. Cifdaloz, R. McCullen, J. Benavides, S. Sridharan, A. Kelkar, J. Vogel, and D. Soloway, "Modeling and Control of Scramjet-Powered Hypersonic Vehicles: Challenges, Trends, & Tradeoffs," in *AIAA Guidance, Navigation and Control Conference*, 2008, pp. 1 —- 39.

[2] D. Soloway, A. Rodriguez, J. Dickeson, O. Cifdaloz, J. Benavides, S. Sridharan, A. Kelkar, and J. Vogel, "Constraint Enforcement for Scramjet-Powered Hypersonic Vehicles with Significant Aero-Elastic-Propulsion Interactions," in *IEEE American Control Conference*, 2009, pp. 3154 – 3159.

[3] J. Dickeson, A. Rodriguez, S. Sridharan, J. Benavides, D. Soloway, A. Kelkar, and J. Vogel, "Decentralized Control of an Airbreathing Scramjet-Powered Hypersonic Vehicle," in *AIAA Guidance, Navigation and Control Conference*, 2009, pp. 1 —- 37.

[4] A. Rodriguez, J. Dickeson, S. Sridharan, A. Korad, J. Khatri, J. Benavides, D. Soloway, A. Kelkar, and J. Vogel, "Control-Relevant Modeling, Analysis, and Design for Scramjet-Powered Hypersonic Vehicles," in *16th AIAA/DLR/DGLR International Space Planes and Hypersonic Systems and Technologies Conference*, 2009, pp. 1 —- 45.

[5] Dickeson J. J., Rodriguez A. A., and S. Sridharan, "Elevator Sizing, Placement, and Control-Relevant Tradeoffs for Hypersonic Vehicles," in *AIAA Guidance, Navigation and Control Conference*, 2010, pp. 1 —- 22.

[6] S. Sridharan, "Control relevant design of scramjet-powered hypersonic vehicles with aero-thermo-elastic-propulsive effects and uncertainty," Master's thesis, Arizona State University, 2010.

[7] S. Sridharan, D. Chitturi, and A. a. Rodriguez, "A receding horizon control approach to portfolio optimization using a risk-minimax objective for wealth tracking," in *IEEE International Conference on Control Applications (CCA)*. Ieee, Sep. 2011, pp. 1282 —-1287. [Online]. Available: http://ieeexplore.ieee.org/lpdocs/epic03/wrapper.htm?arnumber=6044440

[8] S. Sridharan, J. J. Dickeson, and A. A. Rodriguez, "Impact of Plume Modeling on the Design and Control for a Class of Air-Breathing Hypersonic Vehicles," in *AIAA Guidance, Navigation and Control Conference*, 2011, pp. 509 —- 531.

[9] S. Sridharan and A. Rodriguez, "Performance Based Control-Relevant Design for Scramjet-Powered Hypersonic Vehicles," in *AIAA Guidance, Navigation and Control Conference*, 2012, pp. 1 —- 17. [Online]. Available: http://arc.aiaa.org/doi/pdf/10.2514/6.2012-4469

[10] S. Sridharan, A. A. Rodriguez, J. J. Dickeson, and D. Soloway, "Constraint enforcement and robust tube-based control for scramjet-powered hypersonic vehicles with significant uncertainties," in *IEEE American Control Conference*, 2012, pp. 4619 —- 4624. [Online]. Available: http://ieeexplore.ieee.org/xpls/abs_all.jsp?arnumber=6315659

[11] S. Sridharan and A. A. Rodriguez, "Impact of Control Specifications on Vehicle Design for Scramjet-Powered Hypersonic Vehicles," in *AIAA Guidance, Navigation and Control Conference*, 2013, pp. 1 —- 18.

[12] ——, "Design of Portfolio Optimization Strategies and Limitations of Performance Analysis," in *IASTED Control and Applications*, 2013.

[13] G. Stein, "Respect the Unstable," IEEE Control Systems Magazine, pp. 12 – 25, Aug. 2003.

[14] K. Skadron, M. R. Stan, W. Huang, S. Velusamy, K. Sankaranarayanan, D. Tarjan, Skadron K., Stan M. R., Huang W., Velusamy S., and Sankaranarayanan K., "Temperature-Aware Microarchitecture: Extended Discussion and Results," Department of Computer Science, University of Virginia, CS-2003-08, Tech. Rep., 2003.

[15] S. Keshmiri, R. Colgren, and M. Mirmirani, "Development of an Aerodynamic Database for a Generic Hypersonic Air Vehicle," in *AIAA Guidance, Navigation and Control Conf. Paper No. 2006-6257*, 2006.

[16] A. Clark, C. Wu, M. Mirmirani, and S. Choi, "Development of an Airframe Integrated Generic Hypersonic Vehicle Model," in *AIAA Aerospace Conference and Exhibit, Paper No. 2006-6560*, 2006.

[17] M. A. Bolender and D. B. Doman, "A Non-Linear model for the Longitudinal Dynamics of a Hypersonic Airbreathing Vehicle," in *Proceedings of the 2005 Guidance,*

Navigation and Control Conf., Paper No. 2005-6255, vol. 5, no. AIAA-2005-6255, 2005, pp. 3937–3958.

[18] J. J. Dickeson, "Control Relevant Modeling and Design of Scramjet-Powered Hypersonic Vehicles," Ph.D. dissertation, Arizona State University, 2012.

[19] P. Piperni, M. Abdo, F. Kafyeke, and A. T. Isikveren, "Preliminary Aerostructural Optimization of a Large Business Jet," *Journal of Aircraft*, vol. 44, no. 5, pp. 1422 —- 1438, 2007.

[20] J. R. R. A. Martins and A. Lambe, "Multidisciplinary Design Optimization: A Survey of Architectures," *AIAA Journal*, vol. 51, no. 9, pp. 2049 —- 2075, 2013.

[21] R. T. Haftka, "Simultaneous Analysis and Design," *AIAA Journal*, vol. 23, no. 7, pp. 1099 —- 1103, 1985.

[22] E. J. Cramer, J. E. Dennis Jr., P. D. Frank, R. M. Lewis, and G. R. Shubin, "Problem Formulation for Multidisciplinary Optimization," *SIAM Journal on Optimization*, vol. 4, no. 4, pp. 754 —- 776, 1994.

[23] L. S. Lasdon, *Optimization Theory for Large Systems*, 1970.

[24] L. M. Rios and N. V. Sahinidis, "Derivative-free optimization: a review of algorithms and comparison of software implementations," *Journal of Global Optimization*, vol. 56, no. 3, pp. 1247 —- 1293, 2013.

[25] J. Nelder and R. Mead, “A Simplex Method for Function Minimization,” *Computer J.*, vol. 5, pp. 308–313, 1965.

[26] V. Torczon, “On the convergence of pattern search algorithms,” *SIAM Journal on Optimization*, vol. 7, no. 1, pp. 1 —- 25, 1997.

[27] A. L. Custodio and L. N. Vicente, “SID-PSM: A Pattern Search Method Guided by Simplex Derivatives for Use in Derivative-Free Optimization,” Departamento de Matemática, Universidade de Coimbra, Coimbra, Tech. Rep., 2008.

[28] D. R. Jones, C. D. Perttunen, and B. E. Stuckman, “Lipschitzian optimization without the Lipschitz constant,” pp. 157–181, 1993.

[29] M. J. D. Powell, “A direct search optimization method that models the objective and constraint functions by linear interpolation,” in *Advances in Optimization and Numerical Analysis*, 1994, pp. 51 —- 67.

[30] P. Gilmore and C. T. Kelley, “An implicit ltering algorithm for optimization of functions with many local minima,” *SIAM Journal on Optimization*, vol. 5, pp. 269 —- 285, 1995.

[31] D. R. Jones, “A Taxonomy of Global Optimization Methods Based on Response Surfaces,” *Journal of Global Optimization*, vol. 21, pp. 345–383, 2001. [Online]. Available: http://www.springerlink.com/index/KG7634766H12880H.pdf

[32] M. Morari, “Effect of design on the controllability of chemical plants,” in *Interactions Between Process Design and Process Control*, J. D. Perkins, Ed. Pergamon, Oxford, 1992, pp. pp. 3 —- 16.

[33] ——, “Design of resilient processing plant 3: A general framework for the assessment of dynamic resilience,” *Chemical Engineering Science*, vol. 38, no. 11, pp. 1881–1891, 1983. [Online]. Available: http://www.sciencedirect.com/science/article/pii/0009250983850441

[34] F. J. S. and D. P. Looze, “Right Half Plane Poles and Zeros and Design Tradeoffs in Feedback Systems,” *IEEE Transactions on Automatic Control*, vol. 30, no. 6, pp. 555 – 565, 1985.

[35] V. Marcopoli, Freudenberg J. S., R. Middleton, V. Marcopoli, and J. Freudenberg, “Nonminimum Phase Zeros in the General Feedback Configuration,” in *American Control Conf.*, May 2002, pp. 1049 – 1054.

[36] J. B. Hoagg and D. S. Bernstein, “Nonminimum-phase zeros: Much ado about Nothing,” *IEEE Control Systems Magazine*, vol. 24, no. 6, pp. 45 – 57, 2007.

[37] H. K. Fathy, J. A. Reyer, P. Y. Papalambros, and A. G. Ulsoy, “On the Coupling between the Plant and Controller Optimization Problems,” in *American Control Conf.*, 2001, pp. 1864 – 1869.

[38] F. Liao, K. Y. Lum, and J. L. Wang, “An LMI-Based Optimization Approach for Integrated Plant/Output-Feedback Controller Design,” in *American Control Conf.*,, 2005, pp. 4880 – 4885.

[39] R. J. Niewoehner and I. I. Kaminer, “Integrated Aircraft-Controller Design Using Linear Matrix Inequalities,” *Journal of Guidance, Control and Dynamics*, vol. 19, no. 2, pp. 445 – 452, 1996.

[40] K. Grigoriadis, M. J. Carpenter, G. Zhu, and R. E. Skelton, “Optimal Redesign of Linear Systems,” in *American Control Conf.*, 1993, pp. 2680 – 2684.

[41] G. A. Brusher, P. T. Kabamba, and A. G. Ulsoy, “Coupling Between the Modeling and Controller-Design Problems, Part I: Analysis,” *ASME Journal of Dynamic Systems, Measurement, and Control*, vol. 119, no. 3, pp. 498 – 502, 1994.

[42] J. Chen, “New Developments and Applications in Performance Limitation of Feedback Control,” *IEEE Transactions on Automatic Control*, vol. 8, no. 48, p. 1297, 2003.

[43] D. G. Luenberger, *Optimization by Vector Space Methods*. Wiley Professional, 1997.

[44] Dahleh M. A. and I. J. Diaz-Bobillo, *Control of uncertain systems: A linear programming approach*. Prentice Hall, 1995.

[45] S. Boyd and L. Vandenberghe, *Convex Optimization*, 2004.

[46] S. Boyd, L. El Ghaoui, E. Feron, and V. Balakrishnan, *Linear Matrix Inequalities in System and Control Theory*, 15th ed. SIAM, 1994.

[47] K.-C. Goh, M. Safonov, and G. Papavassilopoulos, "A global optimization approach for the BMI problem," *Proceedings of 1994 33rd IEEE Conference on Decision and Control*, vol. 3, 1994.

[48] T.-j. Chung, H.-j. Oh, and C.-s. Chung, "Control System Synthesis Using BMI: Control Synthesis Applications," vol. 1, no. 2, pp. 184–193, 2003.

[49] O. Cifdaloz, "H-Iinfinity Mixed-Sensitivity Optimizations for Infinite Dimensional Plants Subect to Convex Constraints," Ph.D. dissertation, 2007.

[50] S. Boyd, C. Baratt, and S. Norman, "Linear controller design: limits of performance via convex optimization," *Proceedings of the IEEE*, vol. 78, no. 3, pp. 529 – 574, 1990.

[51] P. Gahinet, "Explicit controller formulas for LMI-based H-infinity synthesis," *Proceedings of 1994 American Control Conference - ACC '94*, vol. 3, 1994.

[52] D. Henrion, J. Lofberg, M. Kocvara, and M. Stingl, "Solving polynomial static output feedback problems with PENBMI," *Proceedings of the 44th IEEE Conference on Decision and Control*, 2005.

[53] H. Toker and H. Ozbay, "On the NP-hardness of solving bilinear matrix inequalities and simultaneous stabilization with static output feedback," in *Proceedings of the American Control Conf.*, 1995, pp. 2525—-2526.

[54] J. G. VanAntwerp and R. D. Braatz, "A tutorial on linear and bilinear matrix inequalities," pp. 363–385, 2000.

[55] D. Henrion, J. Lofberg, M. Kocvara, and M. Stingl, "Solving polynomial static output feedback problems with PENBMI," in *Proceedings of the joint IEEE Conference on Decision and Control and European Control Conference*, 2005, pp. 7581 —- 7586.

[56] J. Nie, "Polynomial Matrix Inequality and Semidefinite Representation," *Mathematics of Operations Research*, vol. 36, no. 3, pp. 398—-415, 2011.

[57] D. Henrion and J.-b. Lasserre, "Convergent Relaxations of Polynomial Matrix Inequalities and Static Output Feedback," *IEEE Transactions on Automatic Control*, vol. 51, no. 2, pp. 192 —- 202, 2006.

[58] M. M. Seron, J. H. Braslavsky, and G. C. Goodwin, *Fundamental Limitations in Filtering and Control*, 1997.

[59] S. Skogestad and I. Postlethwaite, *Multivariable Feedback Control: Analysis and Design*, 2ˆnd, Ed. Wiley-Interscience, 2005.

[60] Z.-Q. Wang and M. Sznaier, “L-infinity Optimal Control of SISO Continuous Time Systems and Its Rational Approximations,” pp. 34–39.

[61] V. Kapila and M. Grigoriadis, Karolos, *Actuator Saturation Control*, 1st ed. CRC Press, 2002.

[62] E. D. Sontag, “An algebraic approach to bounded controllability of linear systems,” *International Journal of Control*, vol. 39, no. 1, pp. 181 —- 188, 1984.

[63] W. Heemels and M. Camlibel, “Null controllability of discrete-time linear systems with input and state constraints,” in *2008 47th IEEE Conference on Decision and Control*, no. 1. Ieee, 2008, pp. 3487 —- 3492. [Online]. Available: http://ieeexplore.ieee.org/lpdocs/epic03/wrapper.htm?arnumber=4739333

[64] T. Hu, Z. Lin, and L. Qiu, “An explicit description of null controllable regions of linear systems with saturating actuators,” vol. 47, no. 1, pp. 65–78, 2002.

[65] M. Henk, J. Richter-Gebert, and G. M. Ziegler, “Basic Propeties of Convex Polytopes,” in *Handbook of Discrete and Computational Geometry*, 1997, pp. 243 —- 270.

[66] D. J. Leith and W. E. Leithead, “Survey of gain-scheduling analysis and design,” pp. 1001–1025, 2000.

[67] E. Baumann, C. Bahm, B. Strovers, R. Beck, and M. Richard, "The X-43A Six Degree of Freedom Monte Carlo Analysis," in *46th AIAA Aerospace Sciences Meeting and Exhibit, Paper No. 2008-203*, 2008.

[68] C. Peebles, *Road to Mach 10: Lessons Learned from the X-43A Flight Research Program*. AIAA, 2008.

[69] C. R. McClinton, "X-43 Scramjet Power Breaks the Hypersonic Barrier Dryden Lectureship in Research for 2006," *44th AIAA Aerospace Sciences Meeting and Exhibit, Paper No. 2006-1*, 2007.

[70] V. L. Rausch, C. R. McClinton, and J. L. Crawford, "Hyper-X Flight Validation of Hypersonic Airbreathing Technology," Technical Report, NASA Hyper-X Program Office, pp. 1 – 7, 1997.

[71] W. H. Heiser, D. T. Pratt, D. Daley, and U. Mehta, *Hypersonic Airbreathing Propulsion*. AIAA, 1994.

[72] M. A. Bolender and D. B. Doman, "A Non-Linear Longitudinal Dynamical Model of an Air-Breathing Hypersonic Vehicle," *J. Spacecraft and Rockets*, vol. 44 no. 2, pp. 373–387, 2007.

[73] D. B. D. Michael A. Bolender, M. Bolender, and D. Doman, "Modeling Unsteady Heating Effects on the Structural Dynamics of a Hypersonic Vehicle," in *AIAA Atmospheric Flight Mechanics Conference and Exhibit*, no. AIAA-2006-6646, Keystone, Colorado, 2006.

[74] J. Anderson, *Hypersonic and High-Temperature Gas Dynamics*. Second Edition. AIAA, 2006.

[75] H. Buschek and A. J. Calise, "Robust Control of Hypersonic Vehicles Considering Propulsive and Aeroelastic Effects," *Paper No. AIAA-1993-3762*, pp. 1–11, 1993.

[76] J. Young and J. Underwood, "Development of Aerodynamic Uncertainties for the Space Shuttle Orbiter ," *J. of Spacecraft and Rockets*, vol. 20, no. 6, pp. 513–517, 1983.

[77] M. Bolender, M. Oppenheimer, and D. Doman, "Effects of Unsteady and Viscous Aerodynamics on the Dynamics of a Flexible Air-Breathing Hypersonic Vehicle," in *AIAA Atmospheric Flight Mechanics Conf, & Exhibit, Paper No. 2007-6397*.

[78] J. T. Parker, A. Serrani, S. Yurkovich, M. A. Bolender, and D. B. Doman, "Control-Oriented Modeling of an Air-Breathing Hypersonic Vehicle," *AIAA J. Guidance, Control, and Dynamics*, 2007.

[79] M. Oppenheimer, D. Doman, M. Bolender, and T. Skujins, "A Flexible Hypersonic Vehicle Model Developed with Piston Theory," in *AIAA Atmospheric Flight Mechanics Conference and Exhibit, Paper No. 2007-6396*, 2007.

[80] D. Doman, M. Oppenheimer, and M. Bolender, "Progress in Guidance and Control Research for Space Access and Hypersonic Vehicles," Air Force Research Laboratory (AFRL), Wright Patterson Air Force Base, pp. 1 – 18, Tech. Rep., 2006.

[81] D. Sigthorsson, A. Serrani, S. Yurkovich, M. Bolender, and D. Doman, "Tracking Control for an Overactuated Hypersonic Air-Breathing Vehicle with Steady State Constraints," in {*AIAA*} *Guidance, Navigation and Control Conf., Paper No. 2006-6558*, 2006.

[82] T. Adami, J. Zhu, M. Bolender, D. Doman, and M. Oppenheimer, "Flight Control of Hypersonic Scramjet Vehicles Using a Differential Algebraic Approach," in {*AIAA Guidance, Navigation and Control Conf.*}, *Paper No. 2006-6559*, 2006.

[83] T. Williams, M. A. Bolender, D. Doman, and O. Mortaya, "An Aerothermal Flexible Mode Analysis of a Hypersonic Vehicle," Airforce Research Laboratory (AFRL), Wright Patterson Air Force Base, pp. 1 – 25,, Tech. Rep., 2006.

[84] J. T. Parker, A. Serrani, S. Yurkovich, M. Bolender, and D. Doman, "Approximate Feedback Linearization of an Air-Breathing Hypersonic Vehicle," Air Force Research Laboratory (AFRL), Wright Patterson Air Force Base, pp. 1 – 20, Tech. Rep., 2005.

[85] K. Groves, D. Sigthorsson, A. Serrani, S. Yurkovich, M. Bolender, and D. Doman, "Reference Command Tracking for a Linearized Model of an Air-Breathing Hypersonic Vehicle," in *AIAA Guidance, Navigation and Control Conf. and Exhibit, Paper No. 2005-6144*, 2005.

[86] K. P. Groves, A. Serrani, S. Yurkovich, M. Bolender, and D. Doman, "Anti-Windup Control for an Air-Breathing Hypersonic Vehicle Model," Air Force Research Laboratory (AFRL), Wright Patterson Air Force Base, pp. 1 – 27, Tech. Rep., 2005.

[87] M. A. Bolender and D. B. Doman, “A Non-Linear Model for the Longitudinal Dynamics of a Hypersonic Air-Breathing Vehicle,” in *Proceedings of the 2005 Guidance, Navigation and Control Conf., Paper No. 2005-6255*, 2005.

[88] J. J. Dickeson, A. A. Rodriguez, S. Sridharan, and A. Korad, “Elevator sizing, placement, and control relevant tradeoffs for Hypersonic Vehicles,” in *AIAA Guidance, Navigation and Control Conference*, 2010, pp. pp. 1 —- 23.

[89] J. D. Anderson, *Modern Compressible Flow, 3rd Edition*. McGraw-Hill, 2002.

[90] J. J. Bertin, *Hypersonic Aerothermodynamics*. AIAA Education Series, 1994.

[91] M. W. Oppenheimer and D. B. Doman, “A Hypersonic Vehicle Model Developed with Piston Theory,” in *AIAA 2006-6637*, 2006.

[92] C. E. Cockrell, W. C. Englelund, R. D. Bittner, T. N. Jentink, A. D. Dilley, and A. Frendi, “Integrated Aeropropulsive Computational Fluid Dynamics Methodology for the Hyper-X Flight Experiment,” *J. of Spacecraft and Rockets*, pp. 836–843, 2001.

[93] C. Breitsamter, T. Cvrlje, B. Laschka, M. Heller, and G. Sachs, “Lateral–Directional Coupling and Unsteady Aerodynamic Effects of Hypersonic Vehicles,” *J. Spacecraft and Rockets*, pp. 159–167, 2001.

[94] M. Davis and J. White, "X-43A Flight-Test-Determined Aerodynamic Force and Moment Characteristics at Mach 7.0 ," *J. of Spacecraft and Rockets*, vol. 45, no. 3, pp. 472–484, 2008.

[95] S. Berry, K. Daryabeigi, K. Wurster, and R. Bittner, "Boundary Layer Transition on X-43A," in *38th Fluid Dynamics Conf. and Exhibit, Paper No. 2008-3736*, 2008.

[96] S. A. Berry, A. H. Auslender, A. D. Diller, and J. F. Calleja, "Hypersonic Boundary-Layer Trip Development for Hyper-X," *J. Spacecraft and Rockets*, pp. 853–864, 2001.

[97] R. Starkey, D. Liu, R. Chang, and P. Chem, "Rapid Conceptual Design and Analysis of a Hypersonic Air-Breathing Missile," in *15th AIAA International Space Planes and Hypersonic Systems and Technologies Conf., 2008-2590*, 2008.

[98] S. Torrez, N. Scholten, J. Driscoll, M. Bolender, M. Oppenheimer, and D. D. Doman, "A Scramjet Engine Model Including Effects of Precomubstions Shocks and Dissociation," in *44th AIAA/ASME/SAE/ASEE Joint Propulsion Conference and Exhibit, Paper No. 2008-6386*, 2008.

[99] D. Glass, "Ceramic Matrix Composite (CMC) Thermal Protection Systems (TPS) and Hot Structures for Hypersonic Vehicles ," in 15^{th} *AIAA International Space Planes and Hypersonic Systems and Technologies Conf/*, 2008.

[100] D. H. Baldelli, R. Lind, and M. Brenner, "Nonlinear Aeroelastic/Aeroservoelastic Modeling by Block-Oriented Identification," *J. Guidance, Control and Dynamics*, pp. 1056–1064, 2005.

[101] R. Lind and M. Brenner, *Robust Aeroservoelastic Stablity Analysis: Flight Test Applications*. Springer, 1999.

[102] F. R. Chavez and D. K. Schmidt, "Analytical Aeropropulsive/Aeroelastic Hypersonic-Vehicle Model with Dynamic Analysis," *J. Guidance, Control and Dynamics*, pp. 1308–1319, 1994.

[103] ——, "An Integrated Analytical Aeropropulsive/Aeroelastic Model for the Dynamic Analysis of Hypersonic Vehicle, NASA ARC92-2," NASA, Tech. Rep., Jun. 1992.

[104] M. Rosenlicht, *Introduction to Real Analysis*. Dover Publications Inc., 1986.

[105] I. M. Hull, "Inversion of the Prandtl-Meyer relation," *Aeronautical Journal*, vol. Vol. 79, S, pp. pp. 417 —- 418, 1975.

[106] S. Gumussoy, M. Millstone, and M. Overton, "H∞ strong stabilization via HIFOO, a package for fixed-order controller design," *2008 47th IEEE Conference on Decision and Control*, 2008.

[107] P. Gahinet and P. Apkarian, "Structured H-Infinity Synthesis in MATLAB," in *18th IFAC World Congress*, vol. 18, 2011, pp. 1435–1440. [Online]. Available: http://www.ifac-papersonline.net/Detailed/47945.html

[108] I. Kroo, "Aeronautical applications of evolutionary design," in *VKI Lecture Series on Optimization Methods & Tools for Multicriteria/Multidisciplinary Design*, 2004.

[109] K. G. Bowcutt, "Multidisciplinary Optimization of Airbreathing Hypersonic Vehicles," *Journal of Propulsion and Power*, vol. Vol. 17, N, pp. 1184 – 1190, 2001.

[110] R. Nelson, *Flight Stability and Automatic Control*. McGraw-Hill Science/Engineering/Math, 1997.

[111] J. D. Anderson, *Aircraft Performance and Design*. McGraw-Hill, 1999.

[112] M. Kočvara and M. Stingl, "On the solution of large-scale SDP problems by the modified barrier method using iterative solvers," pp. 285–287, 2009.

APPENDIX A

Trade Studies

A.1 Overview

In this chapter we present a complete list of figures and results obtained from performing single parameter trade studies on the hypersonic vehicle. These results are used to inform the vehicle design process in an integrated system-control multidisciplinary optimization. The parameters considered are

- Elevator location (Section A.2) and elevator size (Section A.3).
- Engine inlet height (Section A.4) and location (Sections A.5 and A.6).
- Upper (Section A.7) and lower (Section A.8) nose angles.
- Stiffness of the vehicle (Section A.9).

Tables A.1 and A.2 in Section A.10 summarizes the trade studies.

A.2 Elevator Location Trade Studies

In this section, we examine the impact of the elevator location on various system properties. The trade study has the following features:

- Elevator location $L_{elev} \in [65, 85]$ feet behind the nose.
- Flow separation by elevator not modeled.
- Elevator assumed to operate on free stream (no downwash).
- Changes in mass distribution neglected.

A.2.1 Static Properties

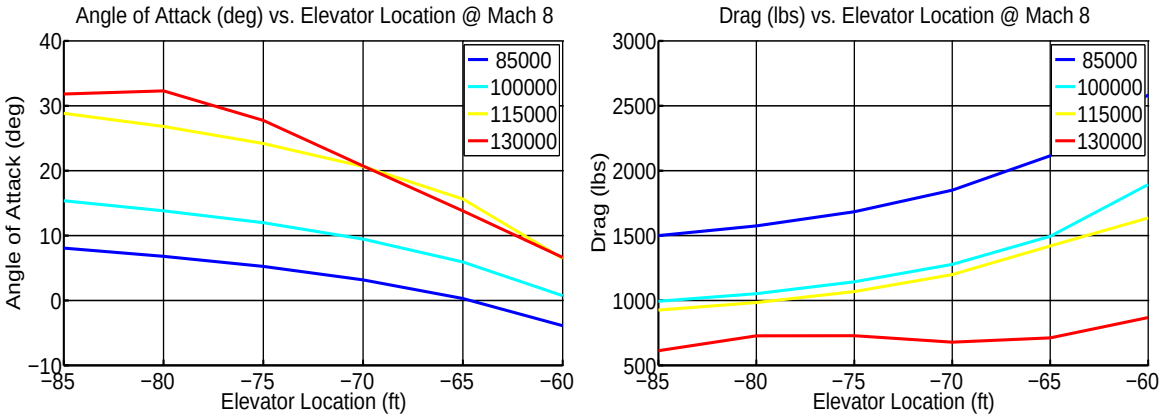

Trim AOA Trim Drag

Figure 33: Trim AOA and Drag with Elevator Location

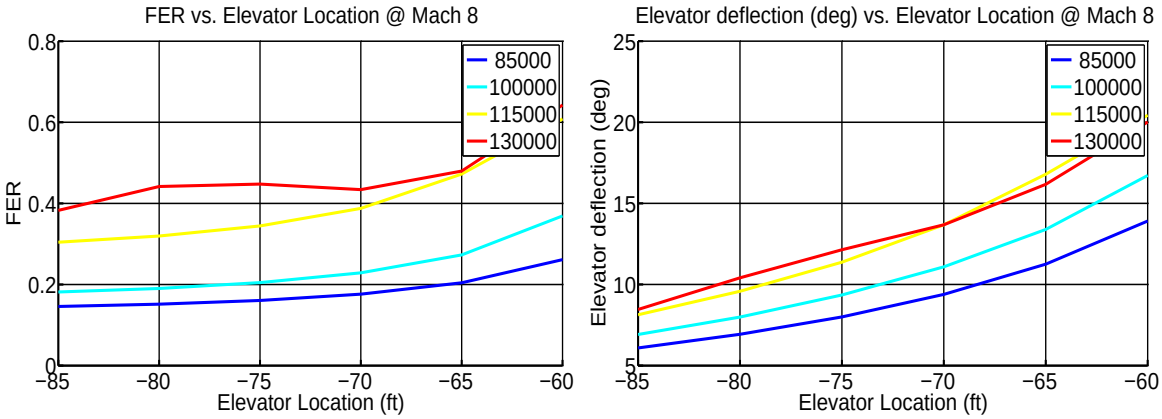

Trim FER Trim Elevator

Figure 34: Trim FER, Elevator with Elevator Location

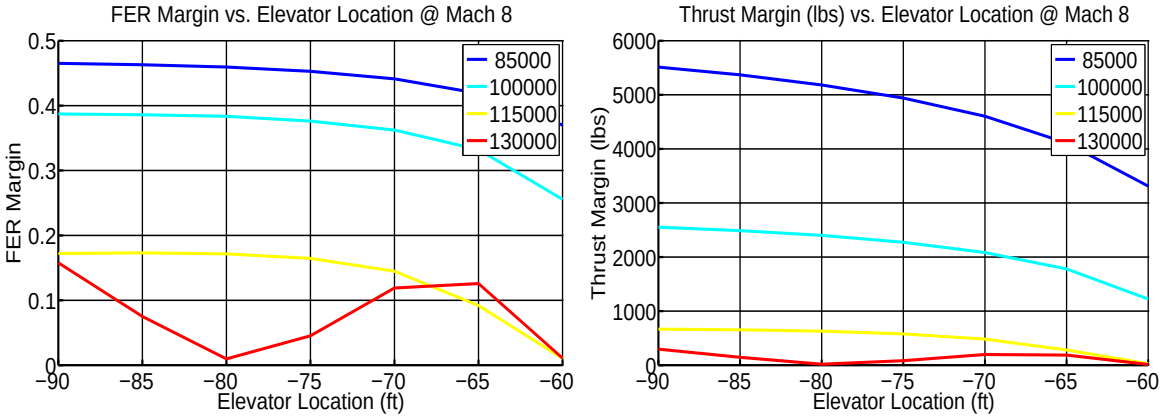

FER Margin Thrust Margin

Figure 35: FER and Thrust Margin with Elevator Location

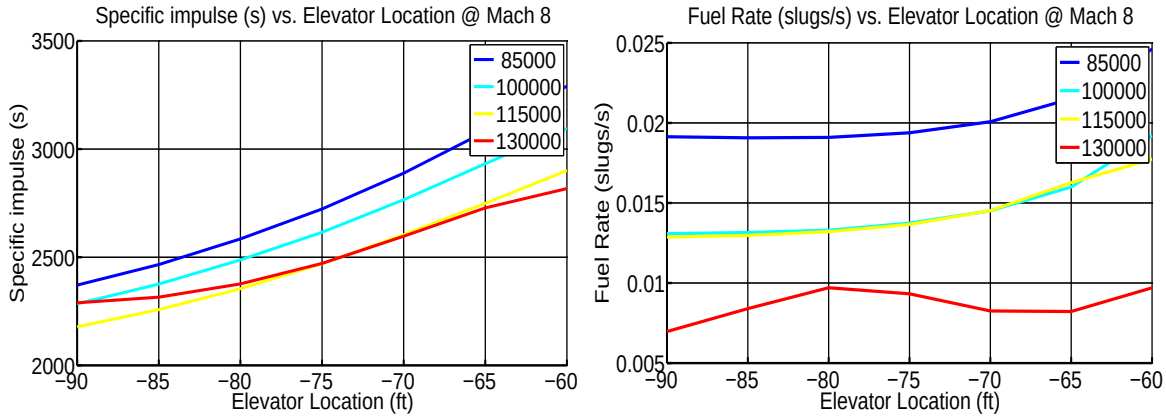

Specific Impulse Fuel Rate

Figure 36: Fuel Rate and Specific Impulse with Elevator Location

A.2.2 Dynamic Properties

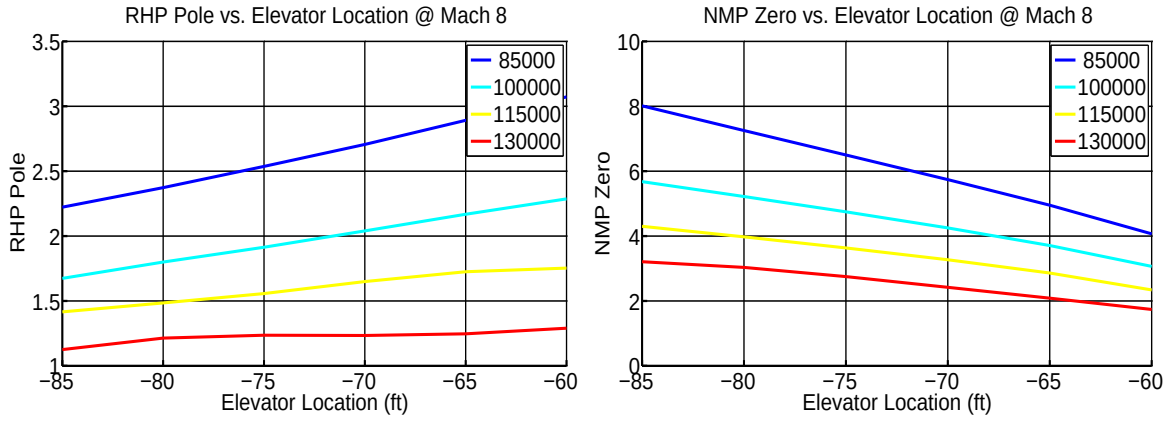

RHP Pole NMP Zero

Figure 37: Pole and Zero with Elevator Location

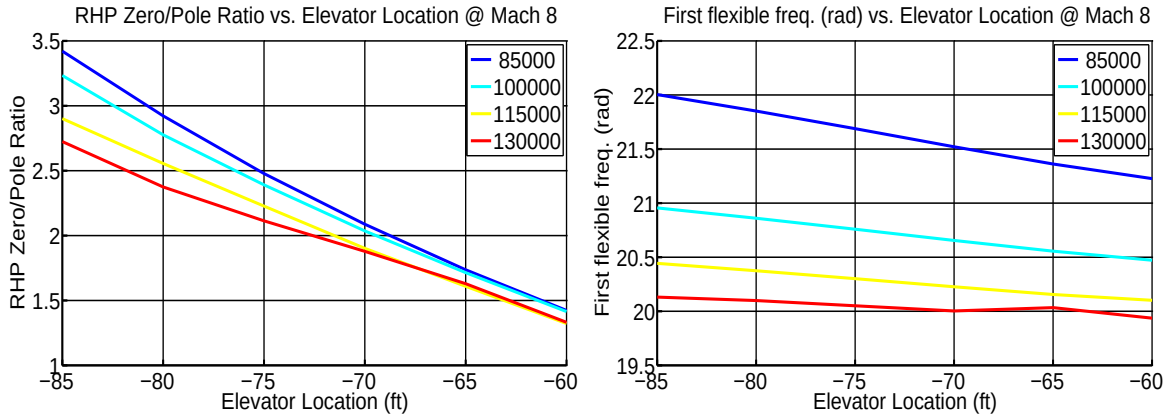

Zero Pole Ratio First Flexible Mode

Figure 38: Zero-Pole Ratio, Flexibility with Elevator Location

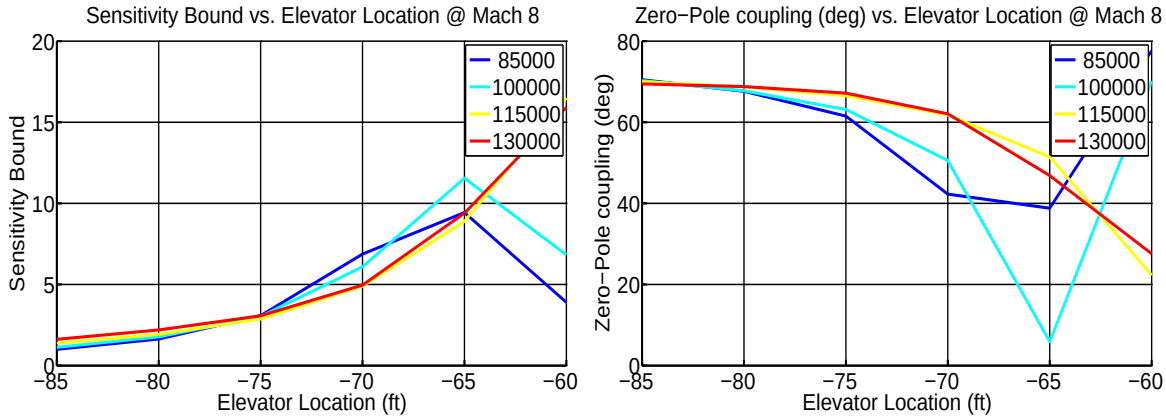

Sensitivity Bound Pole Zero Coupling

Figure 39: Zero Pole Impact with Elevator Location

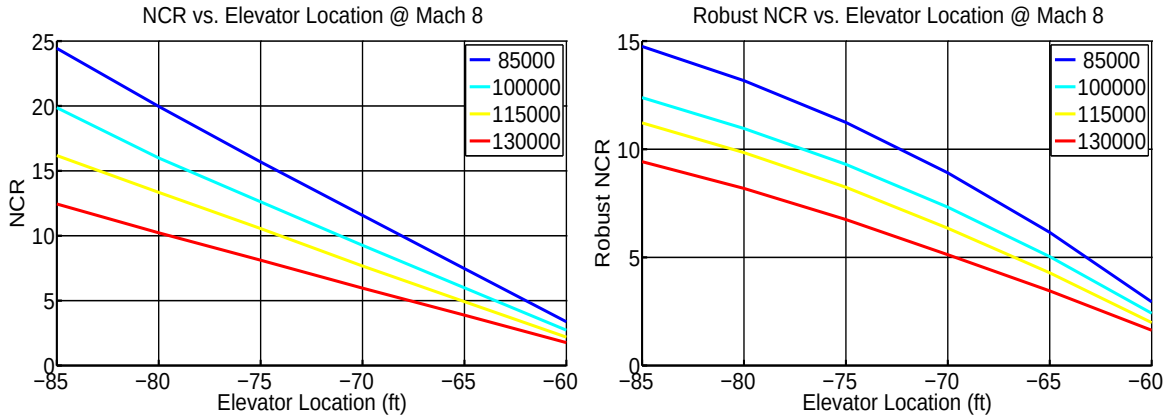

NCR Pole Zero Coupling

Figure 40: (R)NCR variation with Elevator Location

A.3 Elevator Sizing Trade Studies

In this section, we examine the impact of the elevator area on various system properties. The trade study has the following features:

- Elevator area varied: $S_{elev} \in [8.5,\ 34]$ ft^2.
- Elevator modeled as flat plate - flow separation not captured.
- Changes in mass neglected.

A.3.1 Static Properties

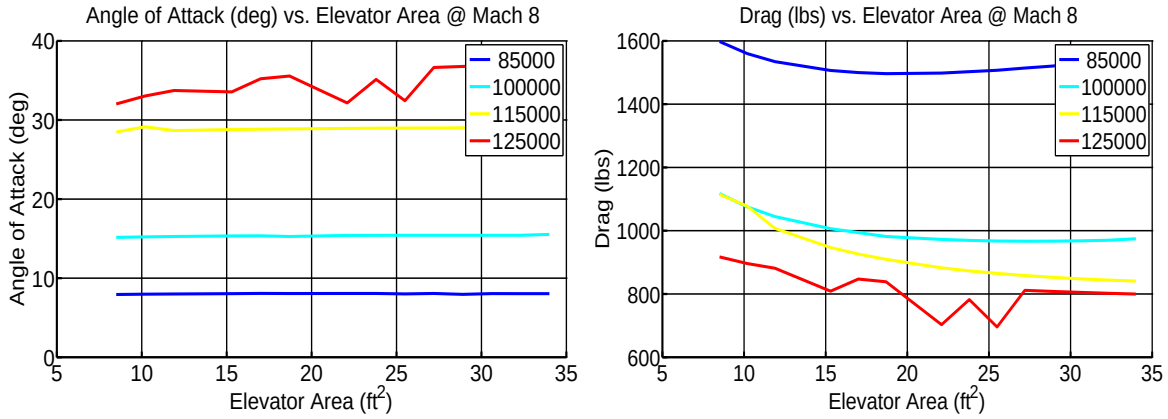

Trim AOA Trim Drag

Figure 41: Trim AOA and Drag with Elevator Area

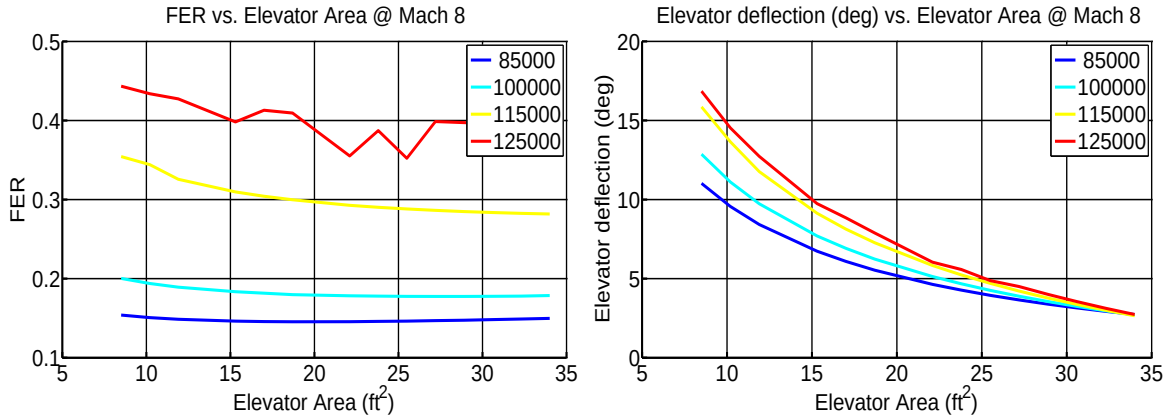

Trim FER Trim Elevator

Figure 42: Trim FER, Elevator with Elevator Area

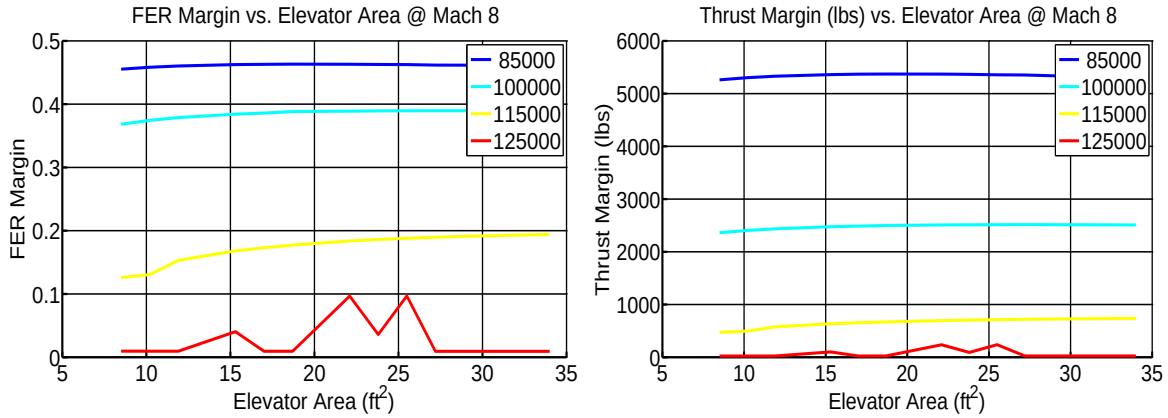

FER Margin Thrust Margin

Figure 43: FER and Thrust Margin with Elevator Area

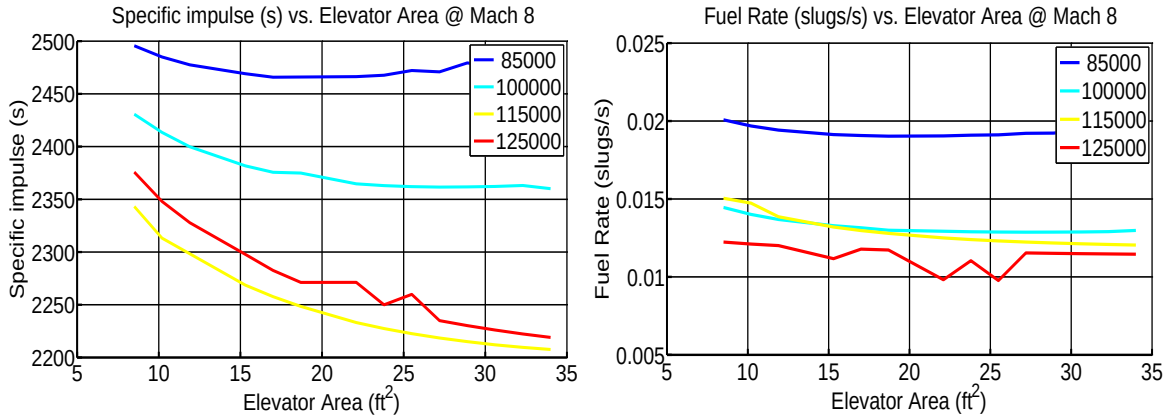

Specific Impulse Fuel Rate

Figure 44: Fuel Rate and Specific Impulse with Elevator Area

A.3.2 Dynamic Properties

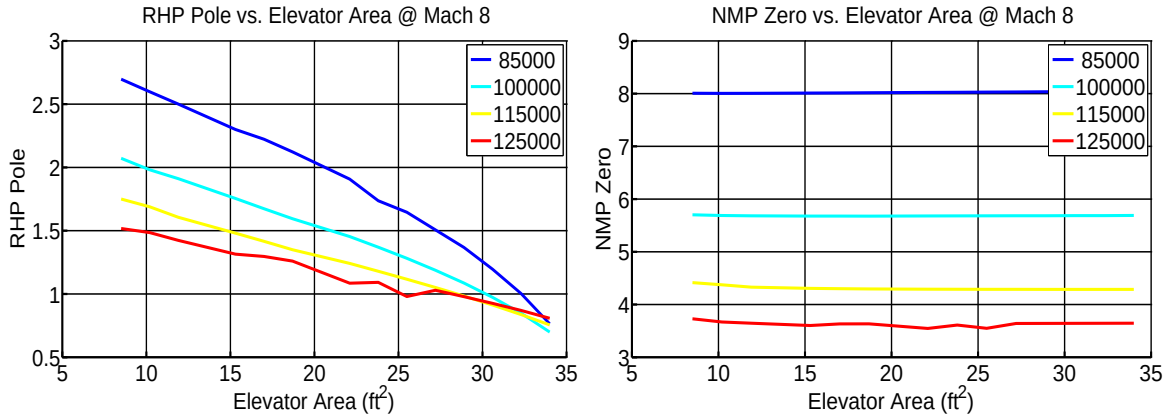

RHP Pole NMP Zero

Figure 45: Pole and Zero with Elevator Area

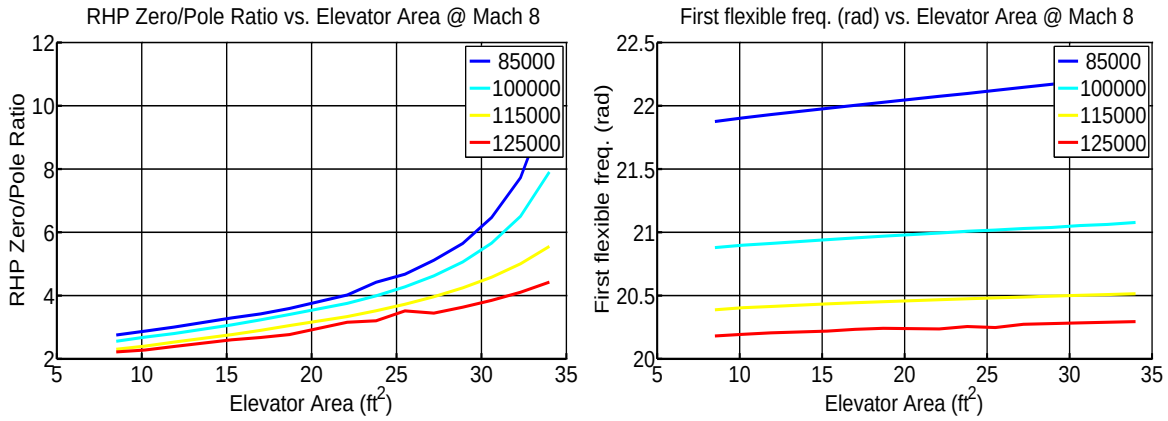

Zero Pole Ratio First Flexible Mode

Figure 46: Zero-Pole Ratio, Flexibility with Elevator Area

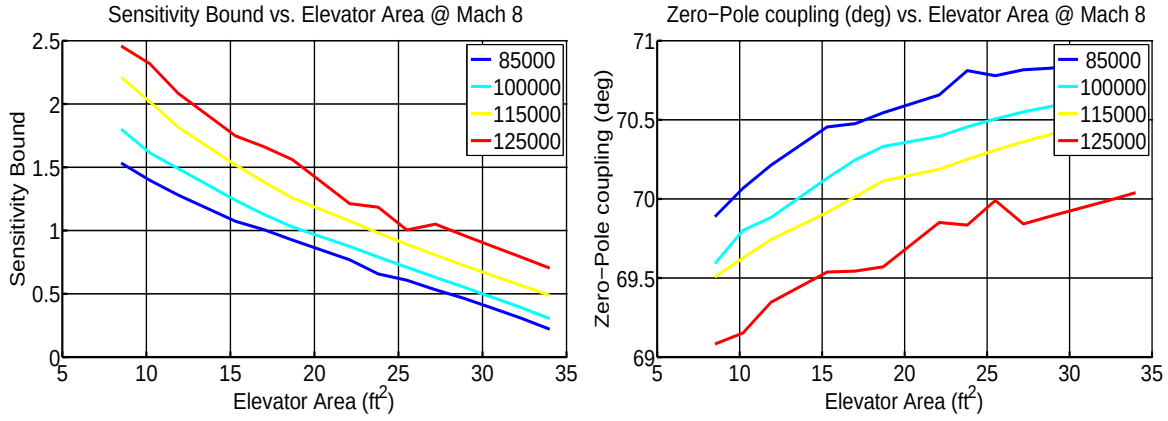

Sensitivity Bound Pole Zero Coupling

Figure 47: Zero Pole Impact with Elevator Area

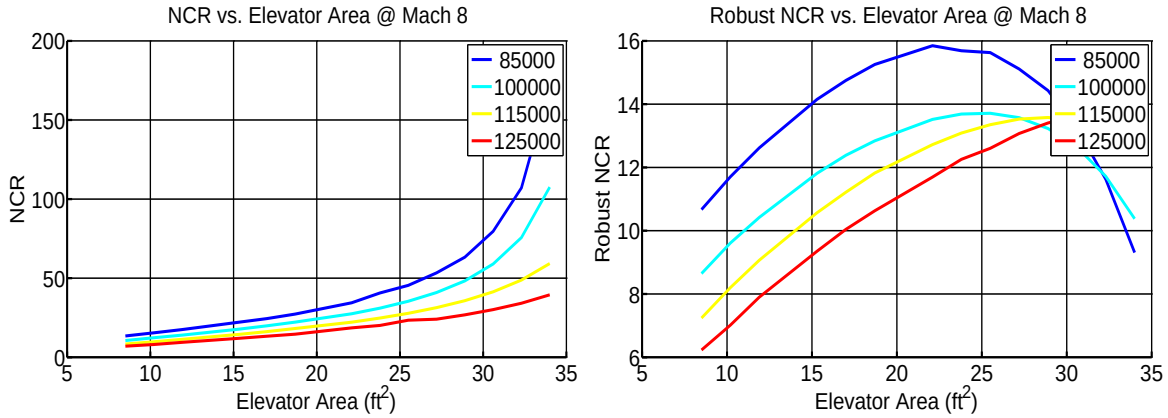

NCR Pole Zero Coupling

Figure 48: (R)NCR variation with Elevator Area

A.4 Engine Inlet Trade Studies

In this section, we examine the impact of increasing the engine inlet height. The trade study has the following features:

- Engine inlet $h_i \in [2, 5]$ feet.
- Shock-on-lip condition assumed.
- Engine mass assumed to scale linearly with height.

A.4.1 Static Properties

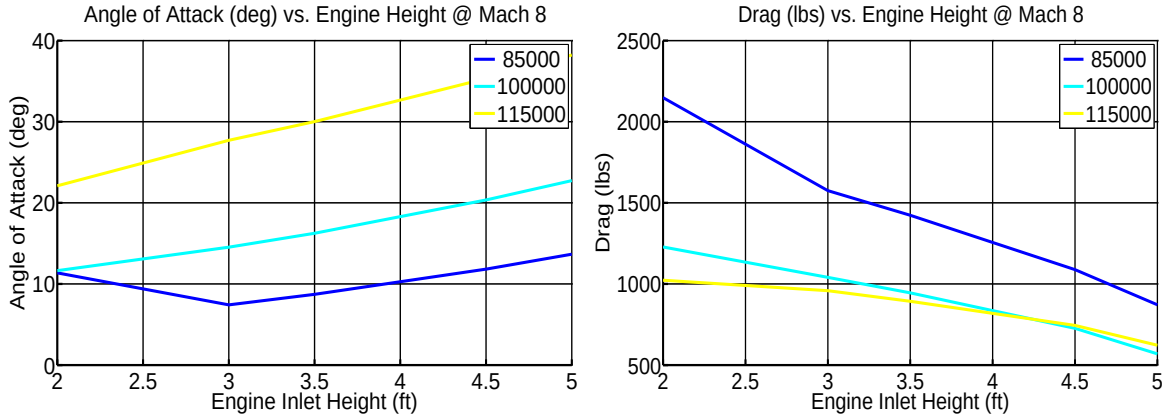

Trim AOA Trim Drag

Figure 49: Trim AOA and Drag with Engine Height

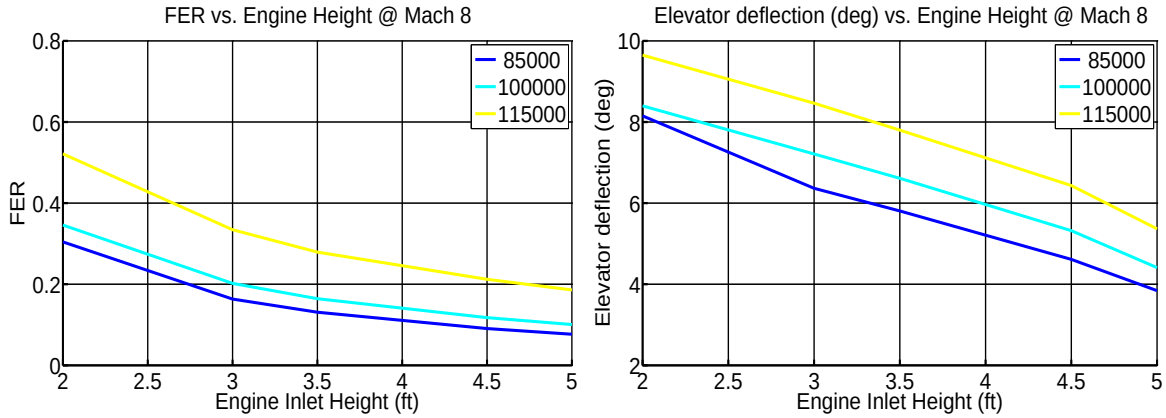

Trim FER Trim Elevator

Figure 50: Trim FER, Elevator with Engine Height

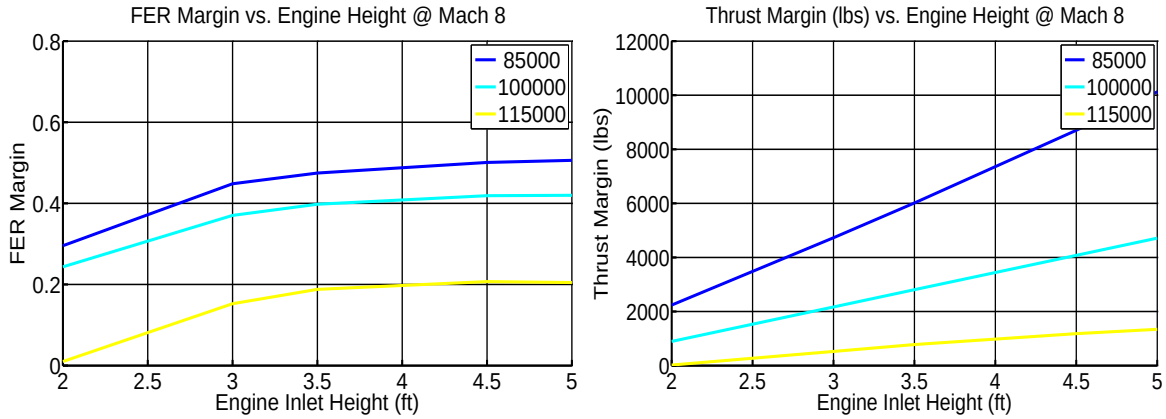

FER Margin Thrust Margin

Figure 51: FER and Thrust Margin with Engine Height

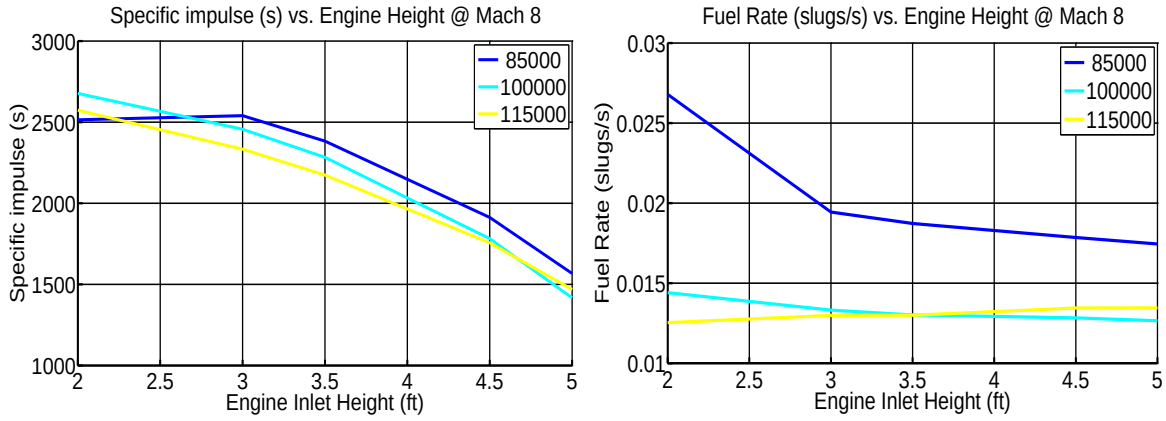

Specific Impulse Fuel Rate

Figure 52: Fuel Rate and Specific Impulse with Engine Height

A.4.2 Dynamic Properties

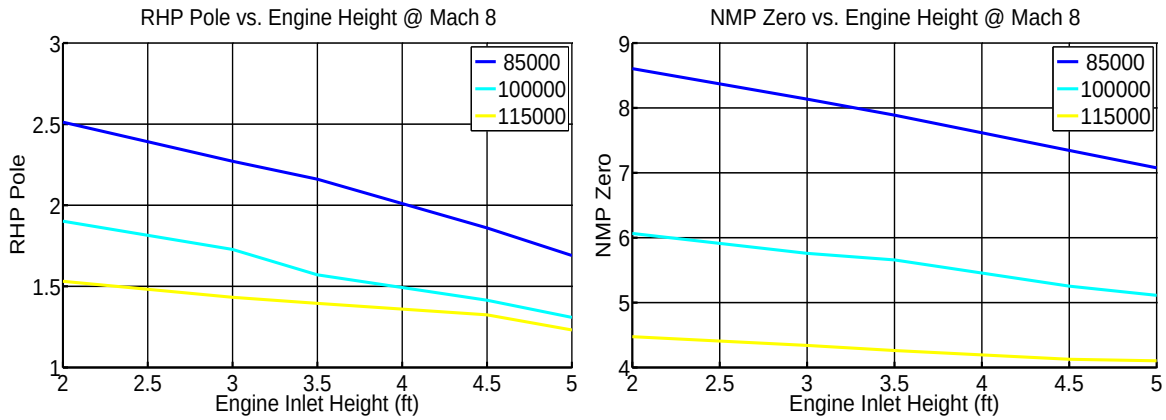

RHP Pole NMP Zero

Figure 53: Pole and Zero with Engine Height

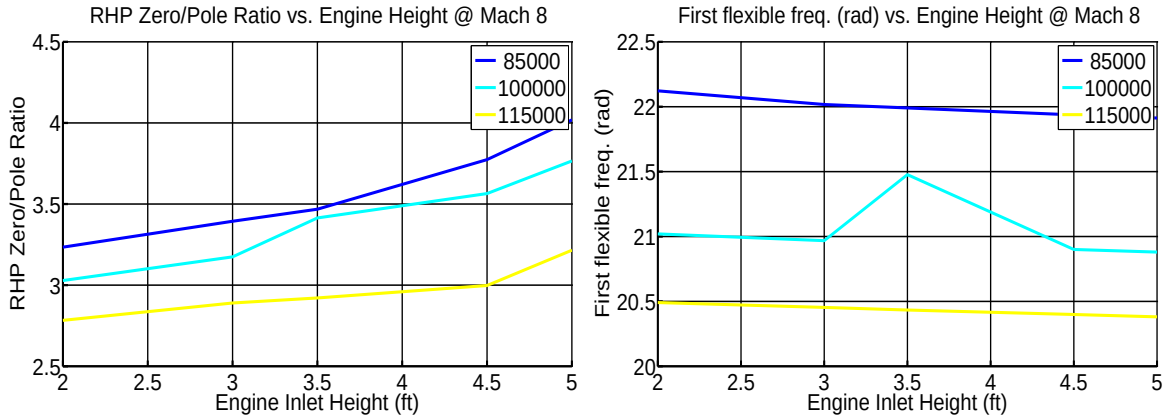

Zero Pole Ratio First Flexible Mode

Figure 54: Zero-Pole Ratio, Flexibility with Engine Height

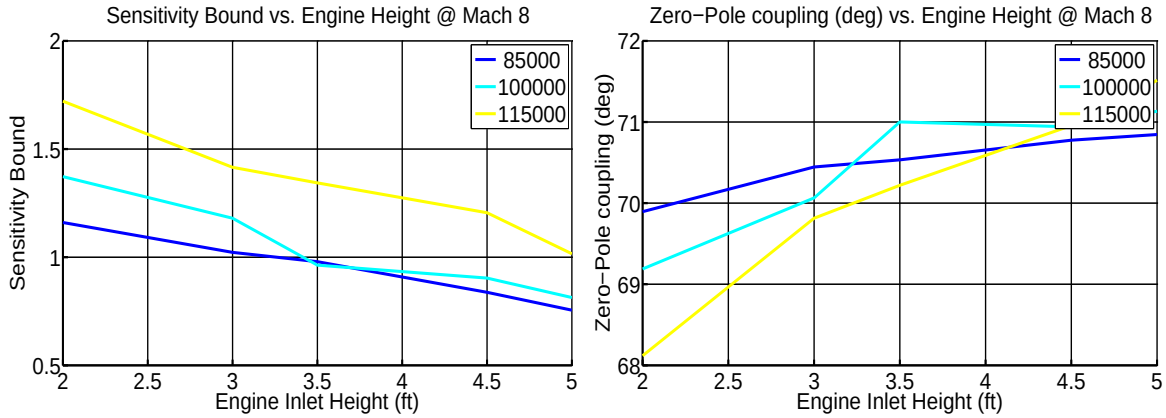

Sensitivity Bound Pole Zero Coupling

Figure 55: Zero Pole Impact with Engine Height

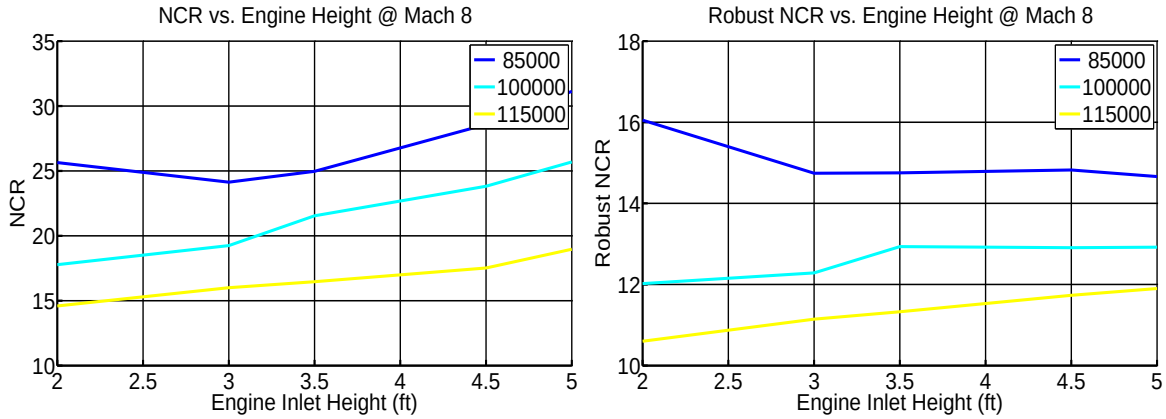

NCR Pole Zero Coupling

Figure 56: (R)NCR variation with Engine Height

A.5 Engine Location Trade Studies

In this section, we examine the impact of changing the engine position. The trade study has the following features:

- Engine location $L_{eng} \in [35, 55]$ feet.
- CG shifts with change in engine.
- Vehicle height variable (constant lower nose inclination).

A.5.1 Static Properties

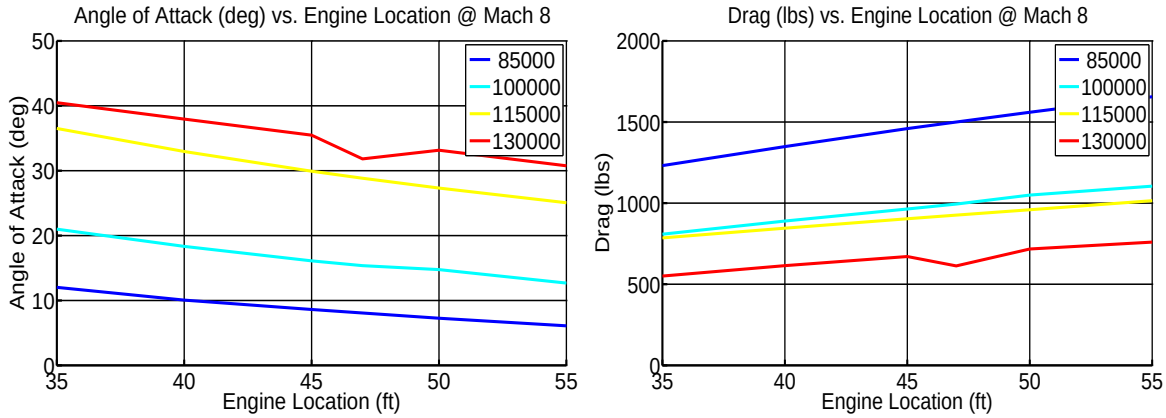

Trim AOA Trim Drag

Figure 57: Trim AOA and Drag with Engine Location

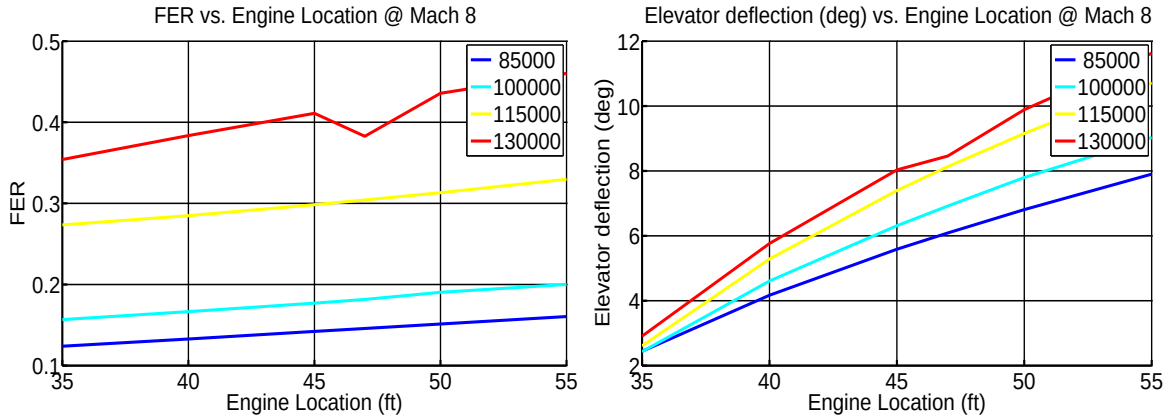

Trim FER Trim Elevator

Figure 58: Trim FER, Elevator with Engine Location

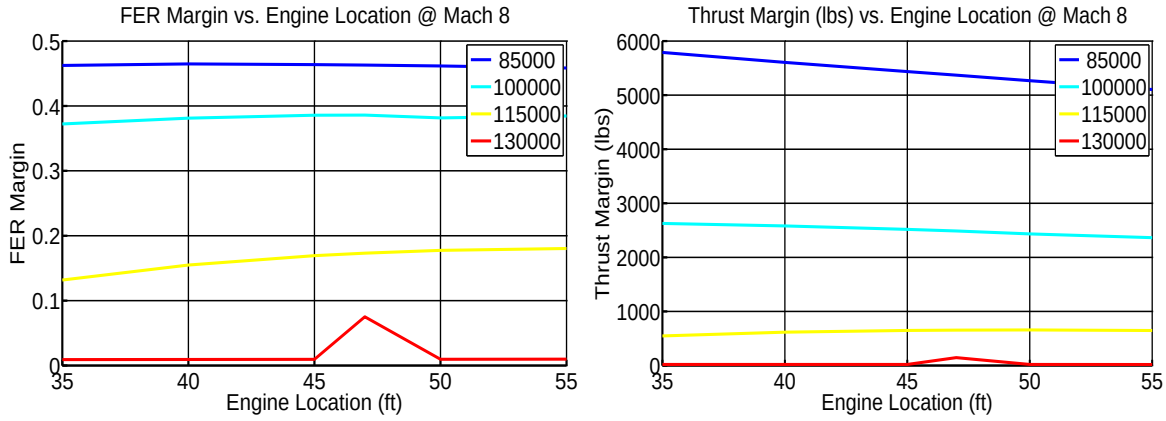

FER Margin Thrust Margin

Figure 59: FER and Thrust Margin with Engine Location

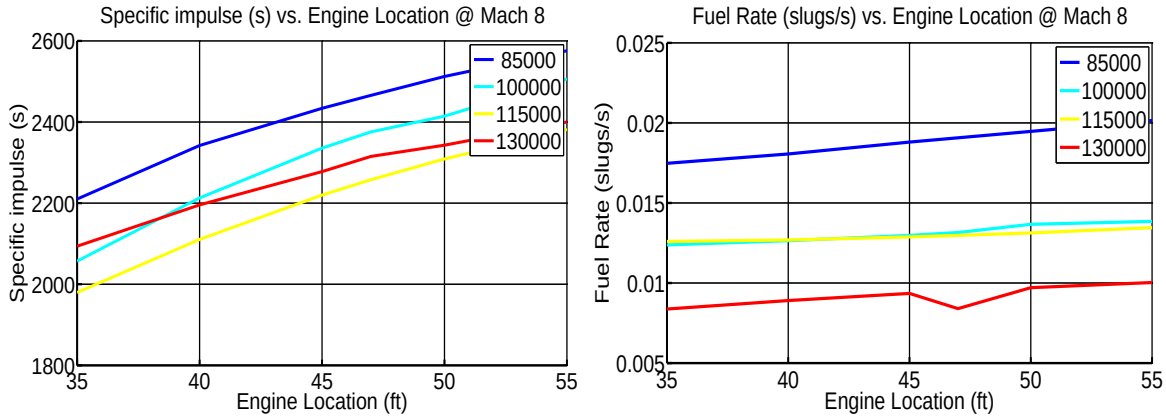

Specific Impulse Fuel Rate

Figure 60: Fuel Rate and Specific Impulse with Engine Location

A.5.2 Dynamic Properties

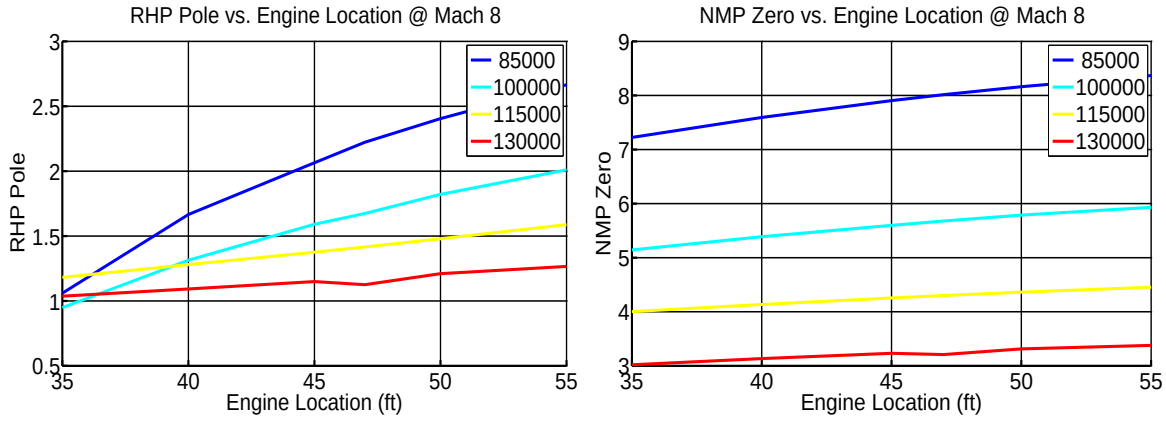

RHP Pole NMP Zero

Figure 61: Pole and Zero with Engine Location

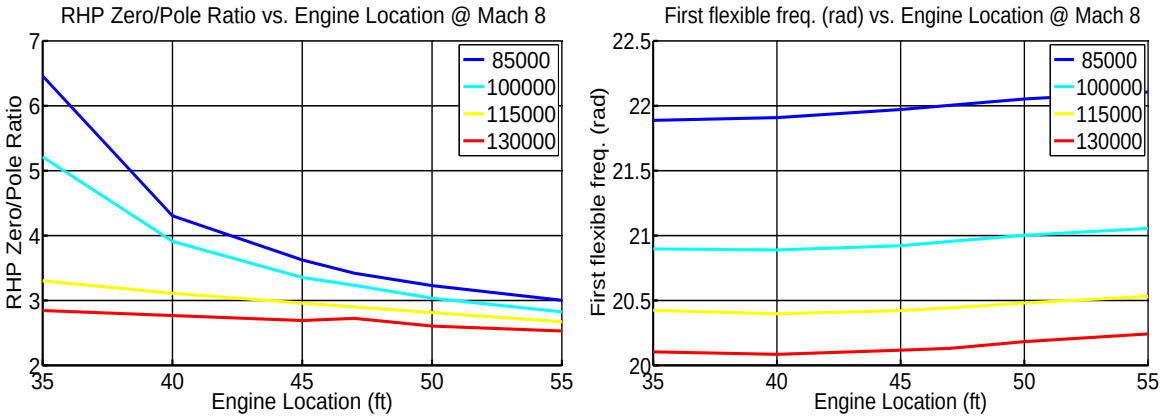

Zero Pole Ratio First Flexible Mode

Figure 62: Zero-Pole Ratio, Flexibility with Engine Location

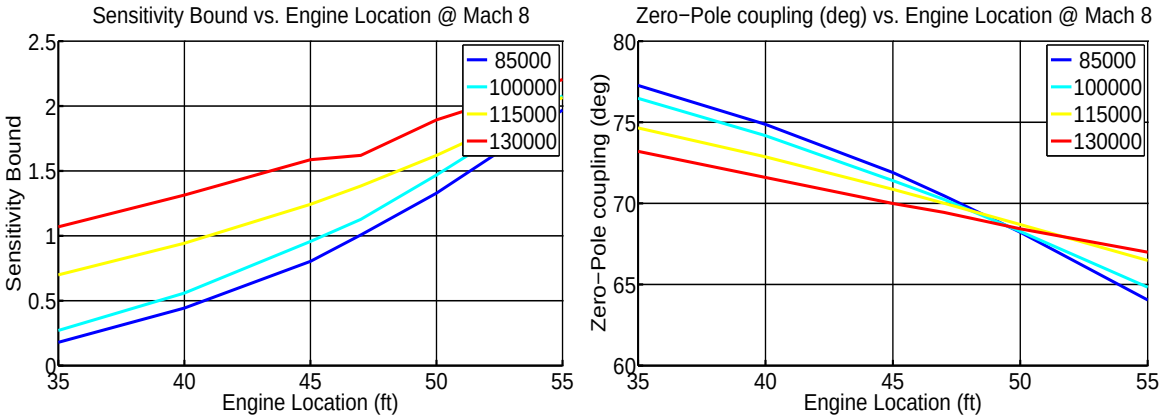

Sensitivity Bound Pole Zero Coupling

Figure 63: Zero Pole Impact with Engine Location

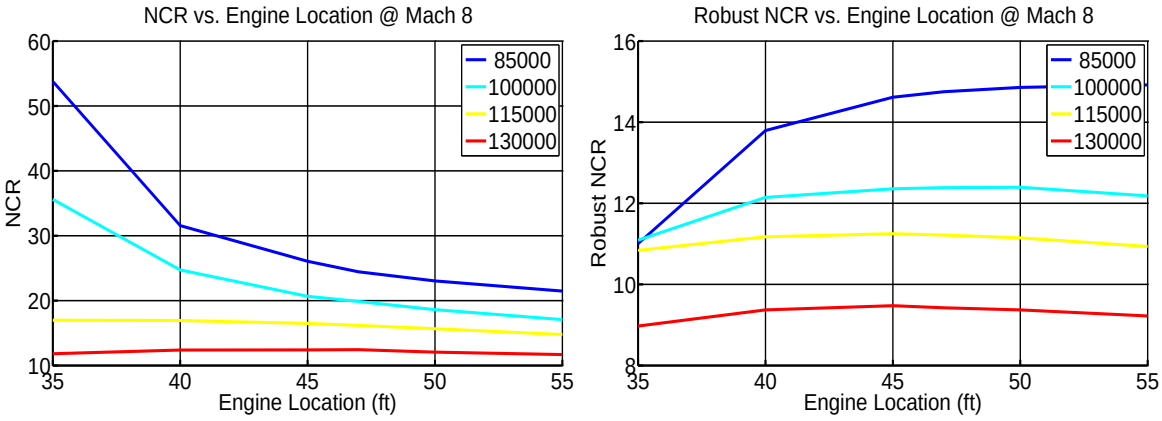

NCR Pole Zero Coupling

Figure 64: (R)NCR variation with Engine Location

A.6 Engine Location (fixed height) Trade Studies

In this section, we examine the impact of changing the engine position. The trade study has the following features:

- Engine location $L_{eng} \in [35, 55]$ feet.
- CG shifts with change in engine.
- Vehicle height constant (variable lower nose inclination).

A.6.1 Static Properties

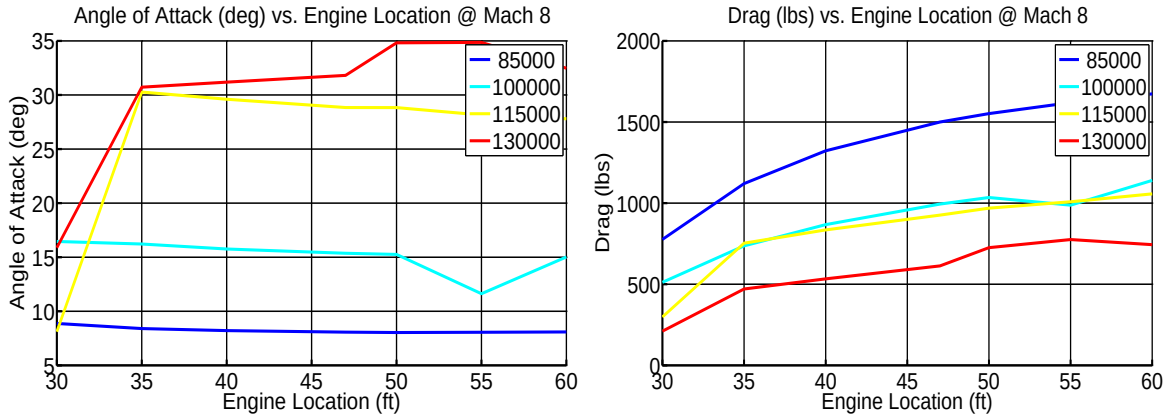

Trim AOA Trim Drag

Figure 65: Trim AOA and Drag with Engine Location

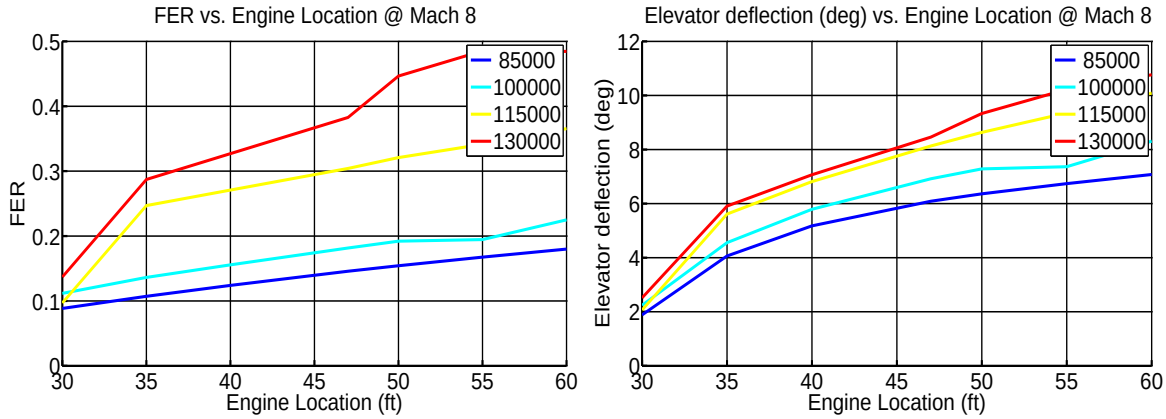

Trim FER Trim Elevator

Figure 66: Trim FER, Elevator with Engine Location

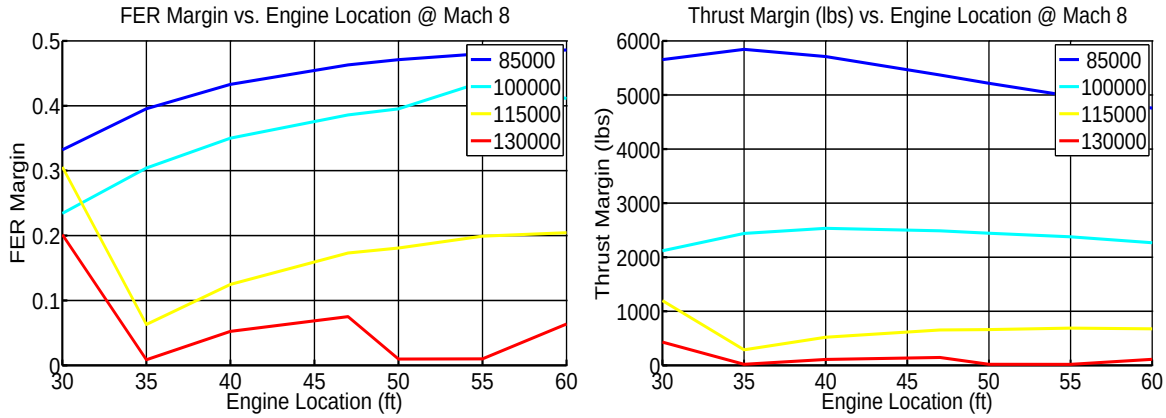

FER Margin Thrust Margin

Figure 67: FER and Thrust Margin with Engine Location

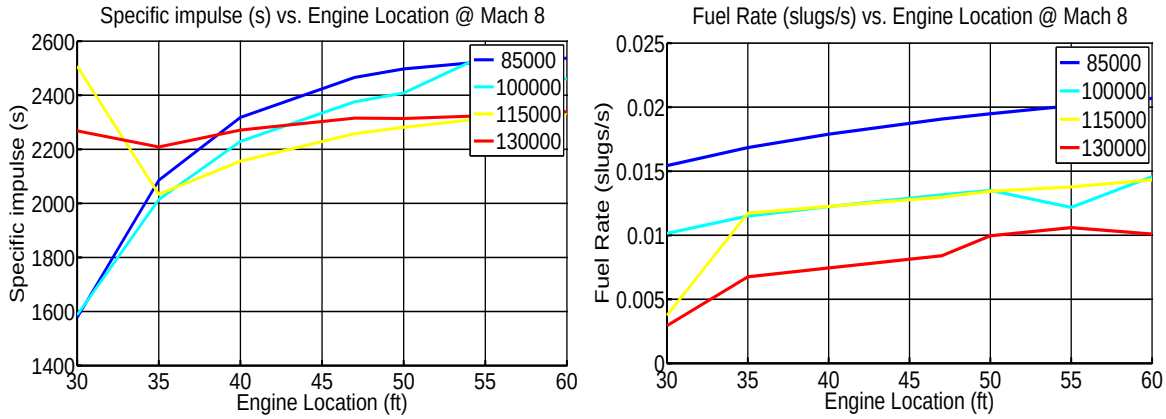

Specific Impulse Fuel Rate

Figure 68: Fuel Rate and Specific Impulse with Engine Location

A.6.2 Dynamic Properties

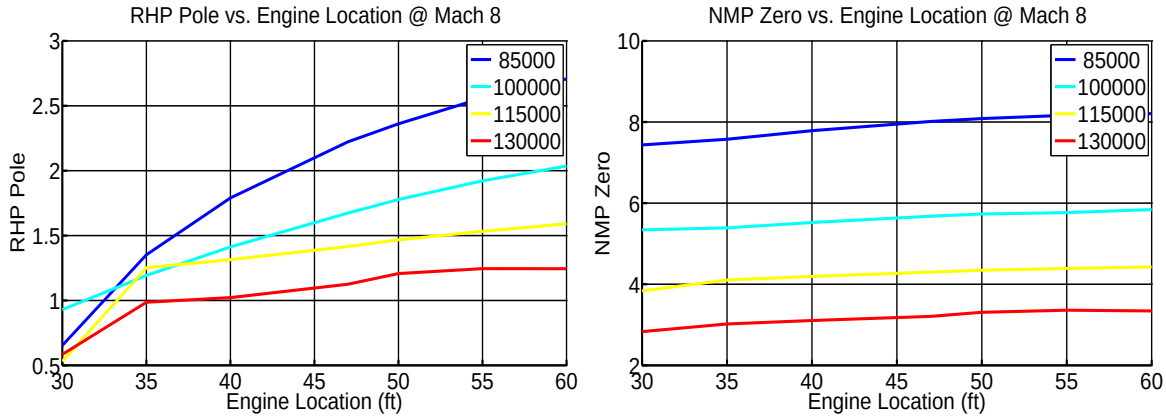

RHP Pole NMP Zero

Figure 69: Pole and Zero with Engine Location

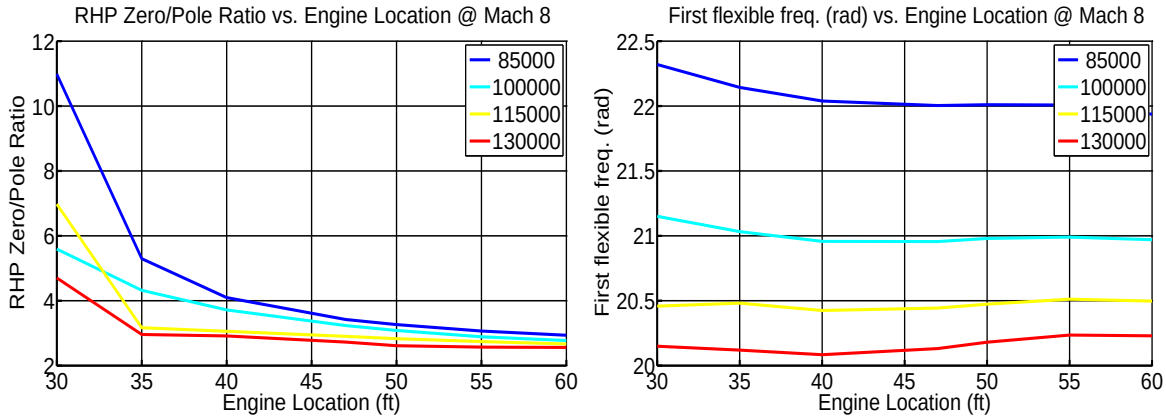

Zero Pole Ratio First Flexible Mode

Figure 70: Zero-Pole Ratio, Flexibility with Engine Location

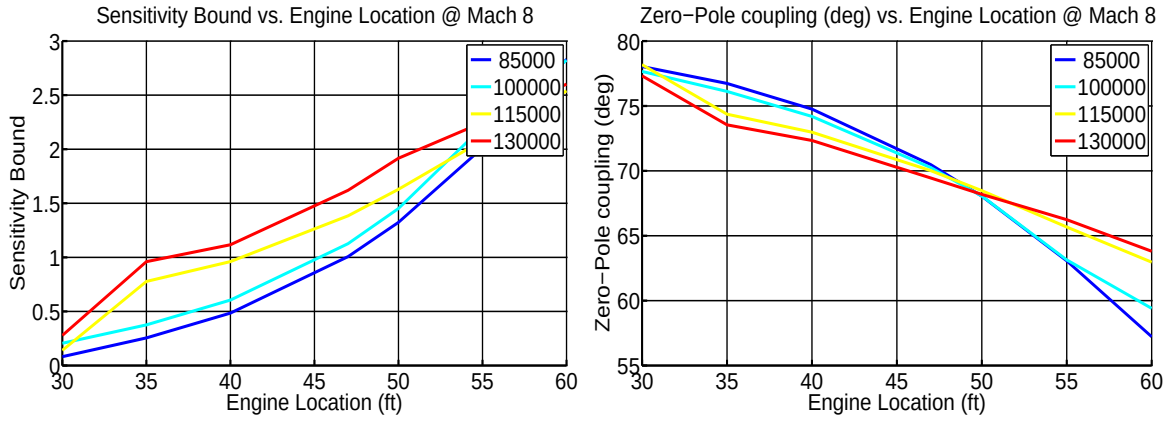

Sensitivity Bound Pole Zero Coupling

Figure 71: Zero Pole Impact with Engine Location

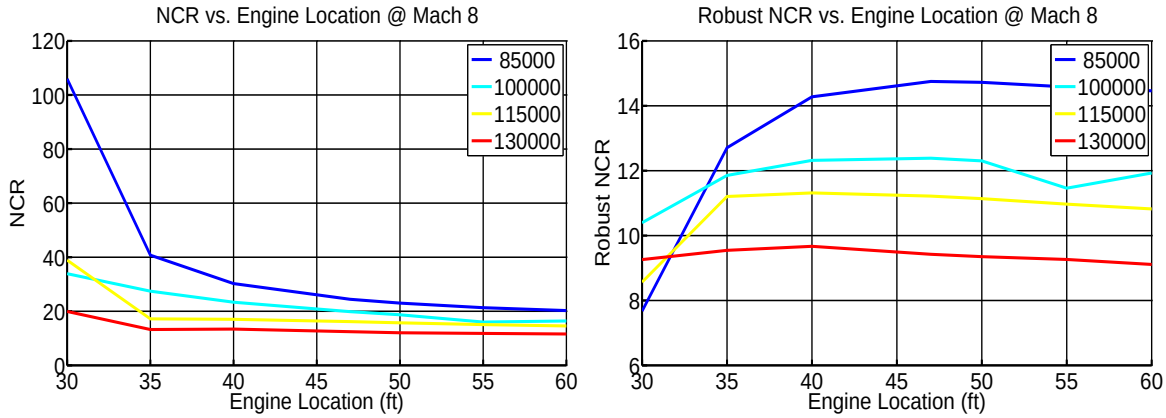

NCR Pole Zero Coupling

Figure 72: (R)NCR variation with Engine Location

A.7 Upper Nose Inclination Trade Studies

In this section, we examine the impact of changing the upper nose inclination. The trade study has the following features:

- Upper nose inclination $\tau_U \in [1, 5]$ deg.
- Heating changes not considered.
- Forebody, aftbody, and engine lengths maintained; height of vehicle changes.

A.7.1 Static Properties

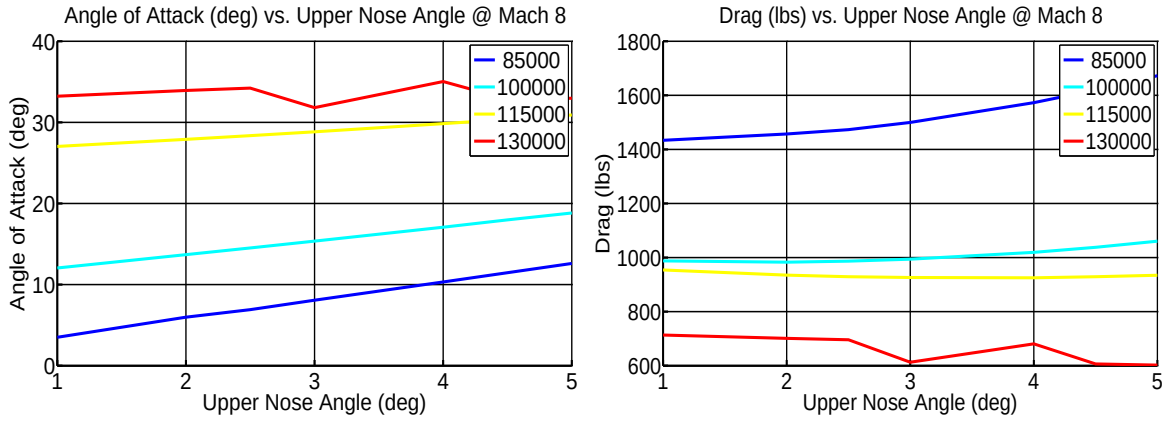

Trim AOA Trim Drag

Figure 73: Trim AOA and Drag with τ_U

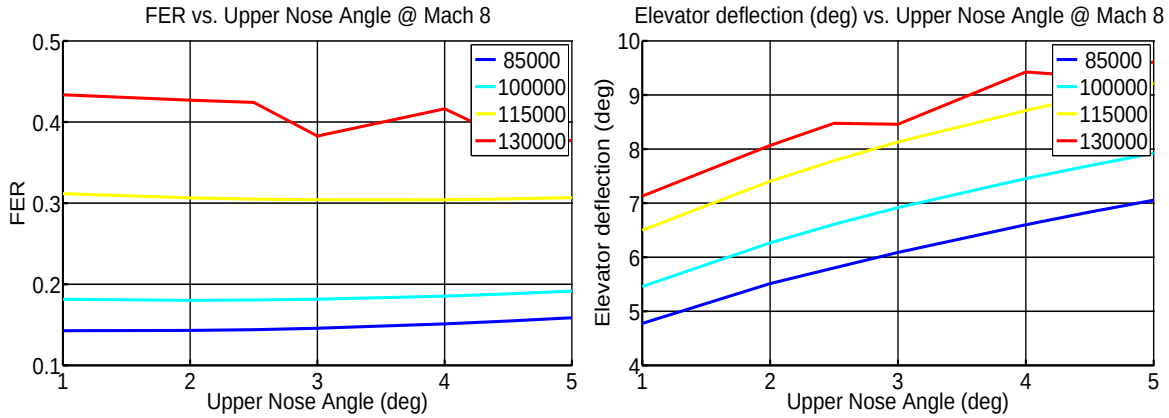

Trim FER Trim Elevator

Figure 74: Trim FER, Elevator with τ_U

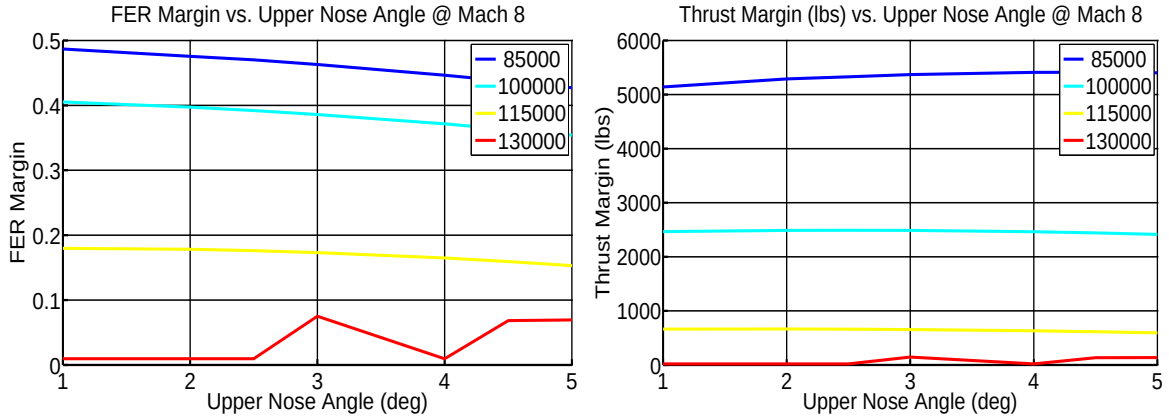

FER Margin Thrust Margin

Figure 75: FER and Thrust Margin with τ_U

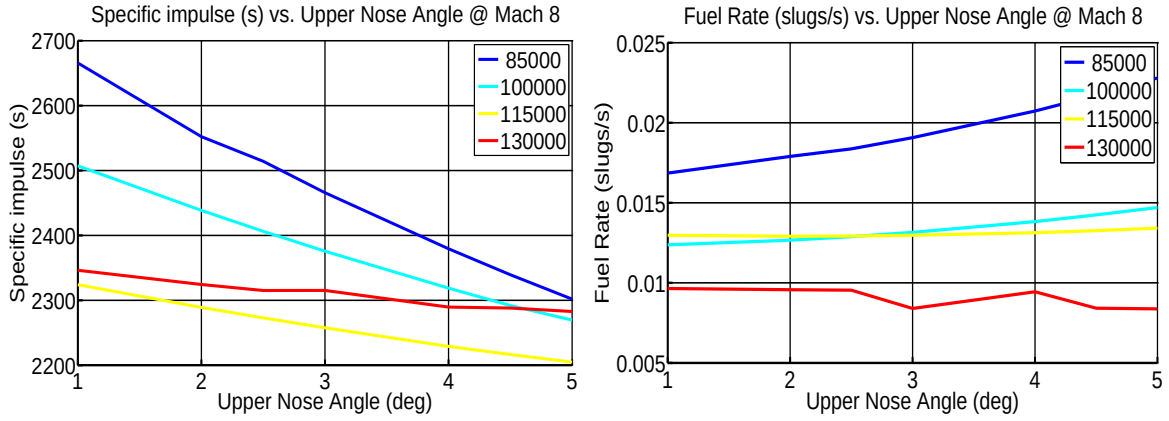

Specific Impulse Fuel Rate

Figure 76: Fuel Rate and Specific Impulse with τ_U

A.7.2 Dynamic Properties

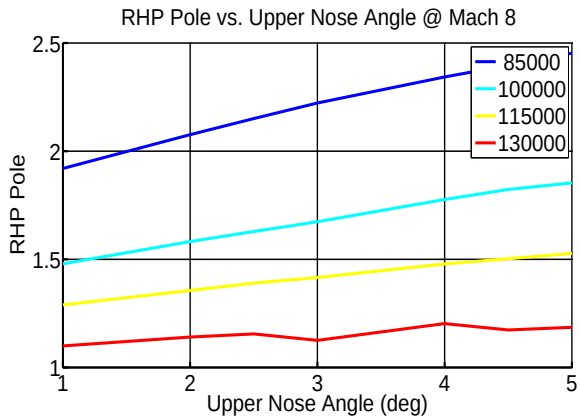

RHP Pole

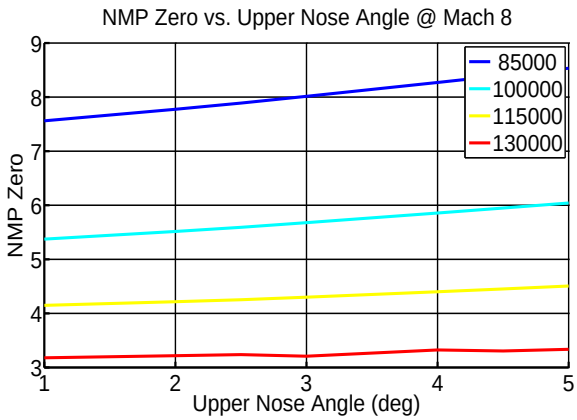

NMP Zero

Figure 77: Pole and Zero with τ_U

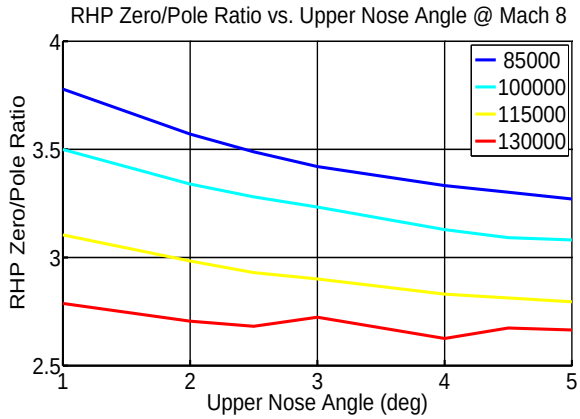

Zero Pole Ratio

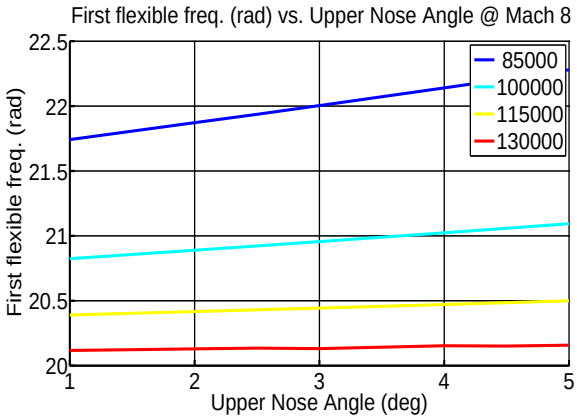

First Flexible Mode

Figure 78: Zero-Pole Ratio, Flexibility with τ_U

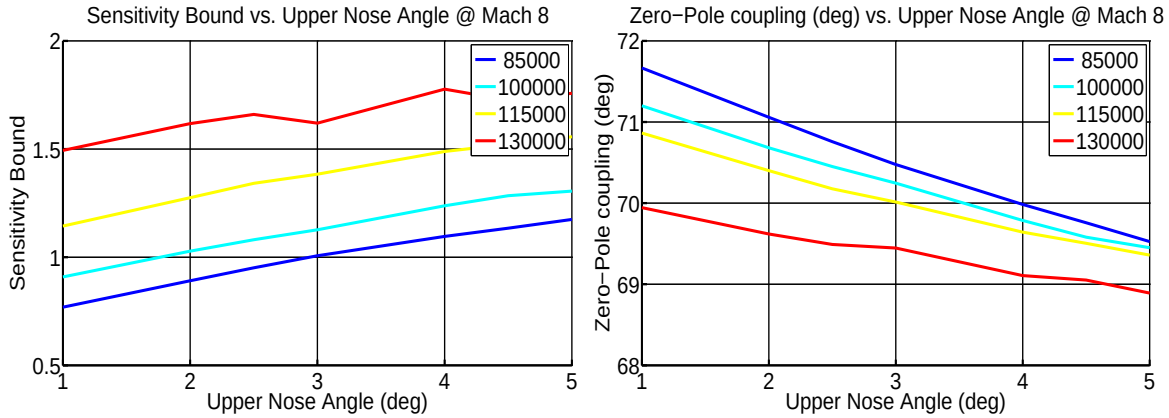

Sensitivity Bound Pole Zero Coupling

Figure 79: Zero Pole Impact with τ_U

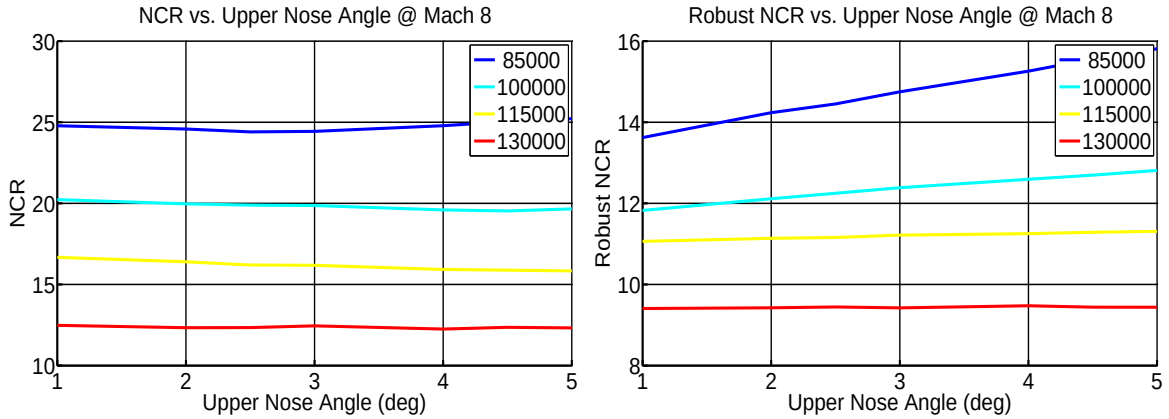

NCR Pole Zero Coupling

Figure 80: (R)NCR variation with τ_U

A.8 Lower Nose Inclination Trade Studies

In this section, we examine the impact of changing the lower nose inclination. The trade study has the following features:

- Upper nose inclination $\tau_L \in [3.2, 8.2]$ deg.
- Heating changes not considered.
- Forebody, aftbody, and engine lengths constant; height of vehicle changes.

A.8.1 Static Properties

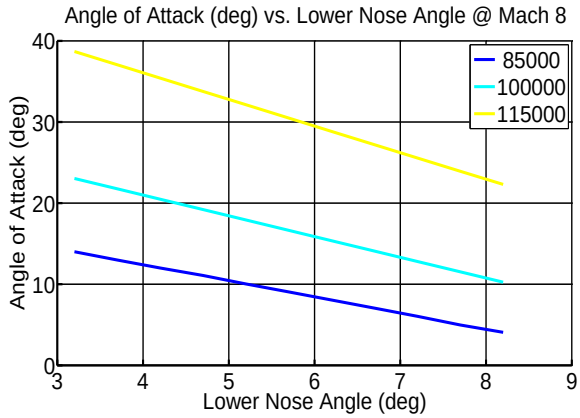

Trim AOA

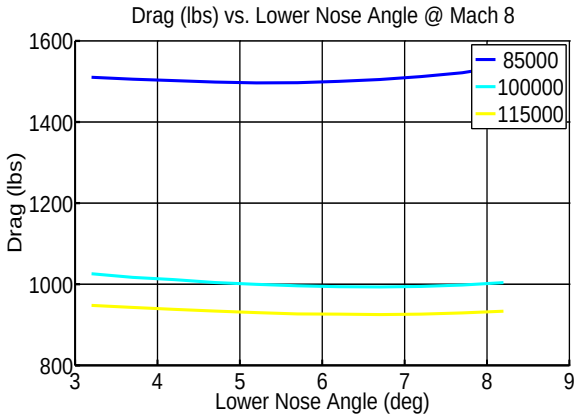

Trim Drag

Figure 81: Trim AOA and Drag with τ_L

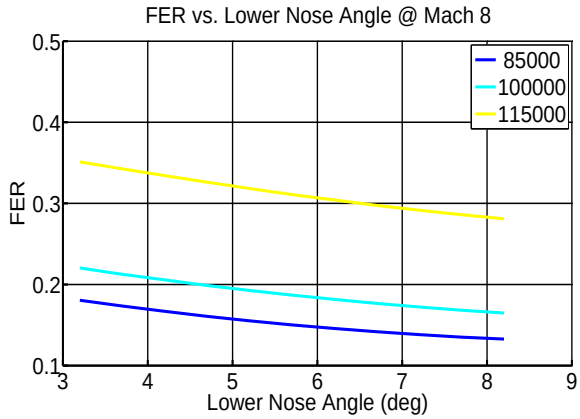

Trim FER

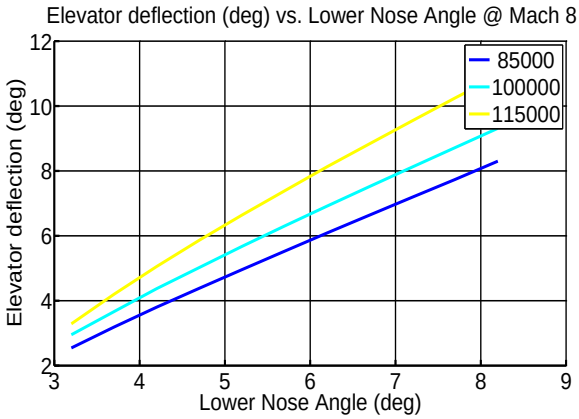

Trim Elevator

Figure 82: Trim FER, Elevator with τ_L

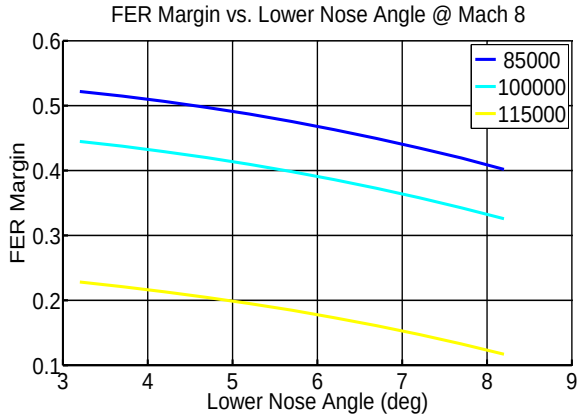

FER Margin

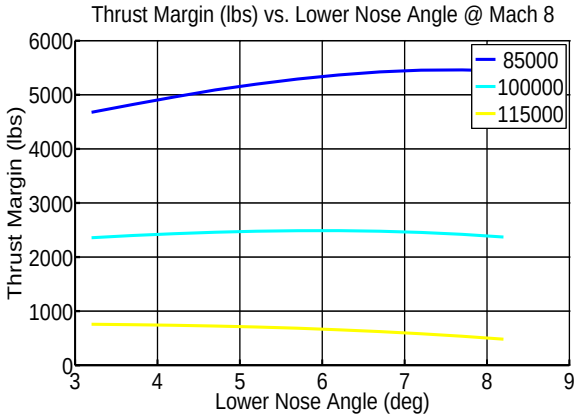

Thrust Margin

Figure 83: FER and Thrust Margin with τ_L

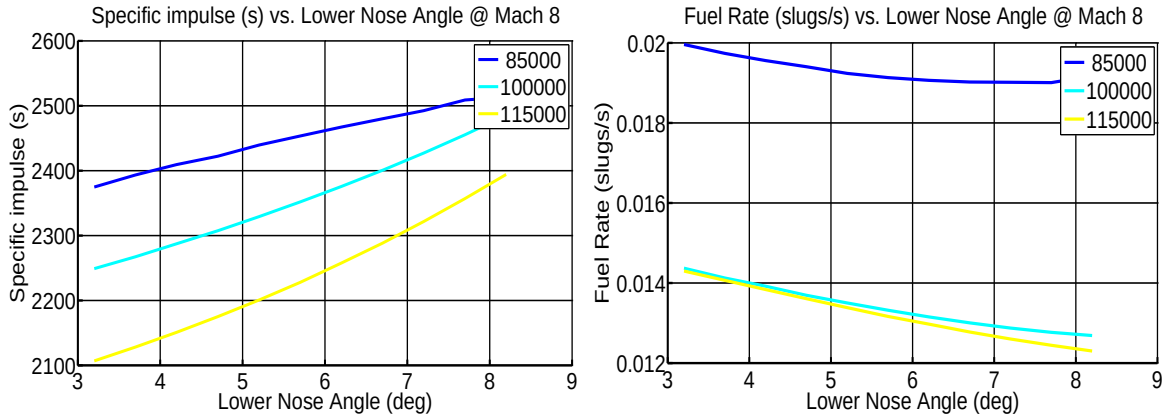

Specific Impulse Fuel Rate

Figure 84: Fuel Rate and Specific Impulse with τ_L

A.8.2 Dynamic Properties

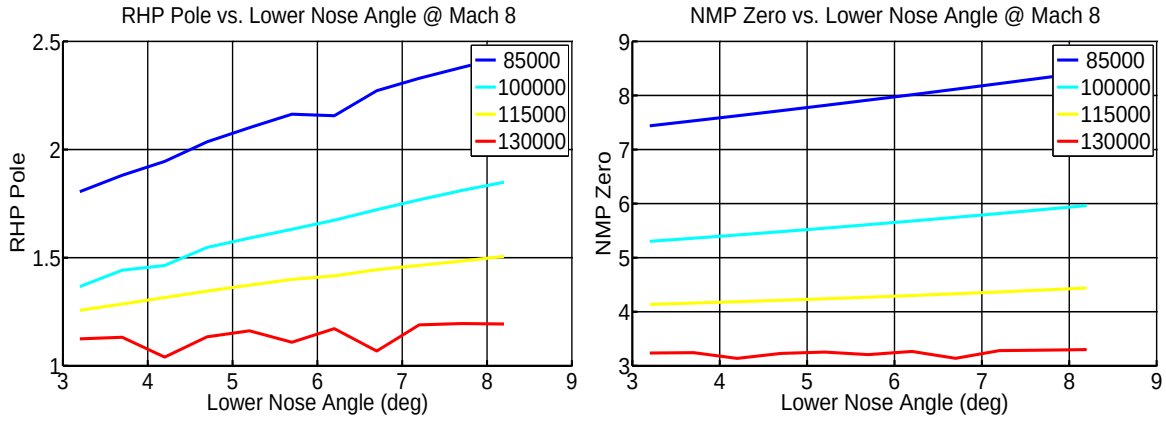

RHP Pole NMP Zero

Figure 85: Pole and Zero with τ_L

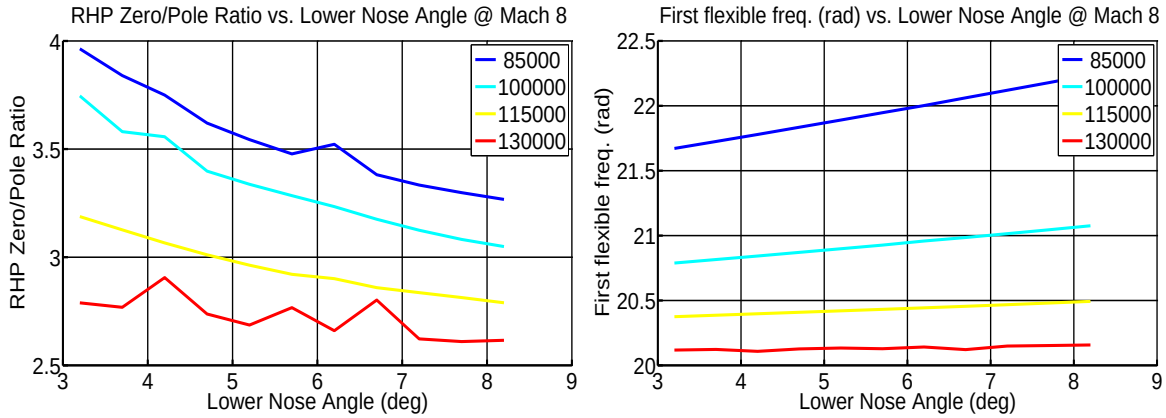

Zero Pole Ratio First Flexible Mode

Figure 86: Zero-Pole Ratio, Flexibility with τ_L

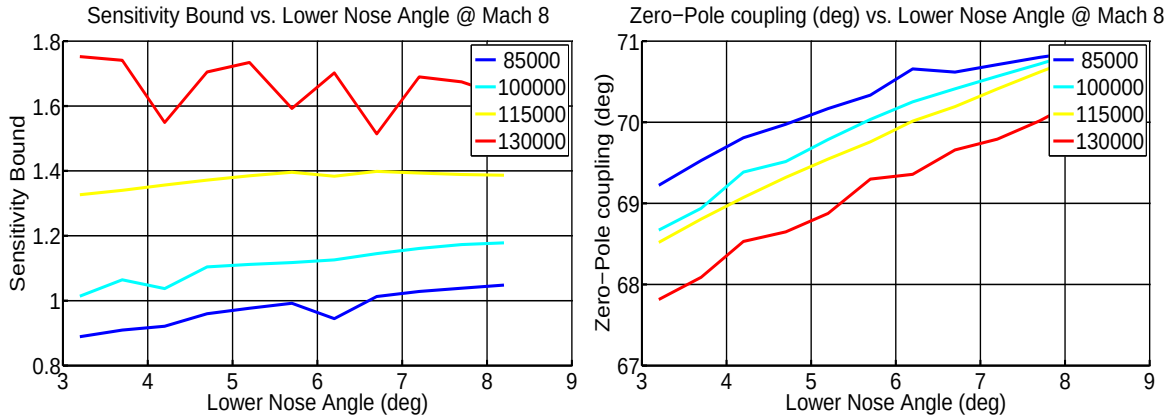

Sensitivity Bound Pole Zero Coupling

Figure 87: Zero Pole Impact with τ_L

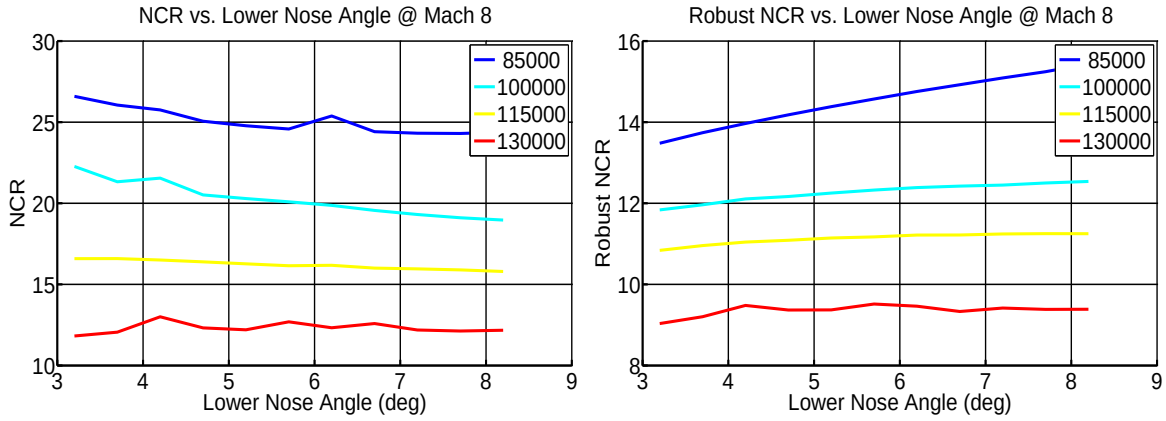

NCR Pole Zero Coupling

Figure 88: (R)NCR variation with τ_L

A.9 Stiffness Trade Studies

In this section, we examine the impact of changing the vehicle stiffness. The trade study has the following features:

- Stiffness scaling $k_{EI} \in [0.5, 2]$.

A.9.1 Static Properties

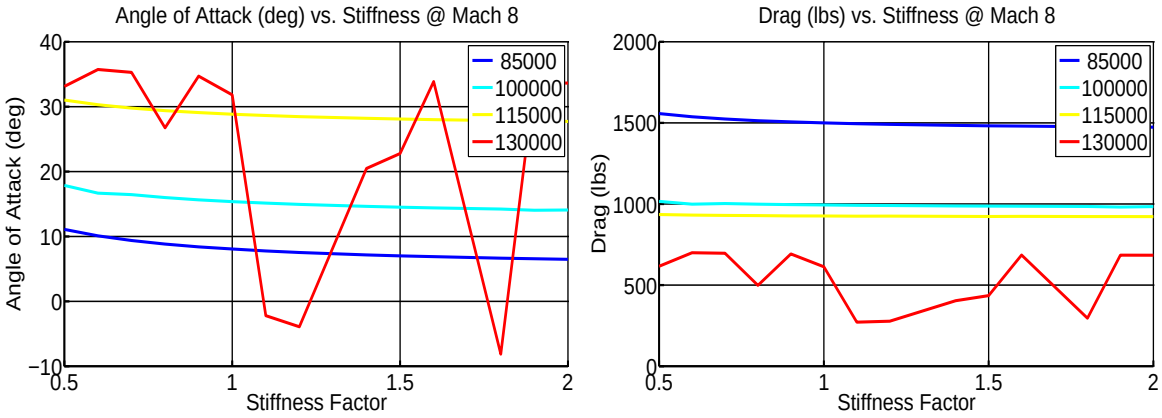

Trim AOA Trim Drag

Figure 89: Trim AOA and Drag with Stiffness

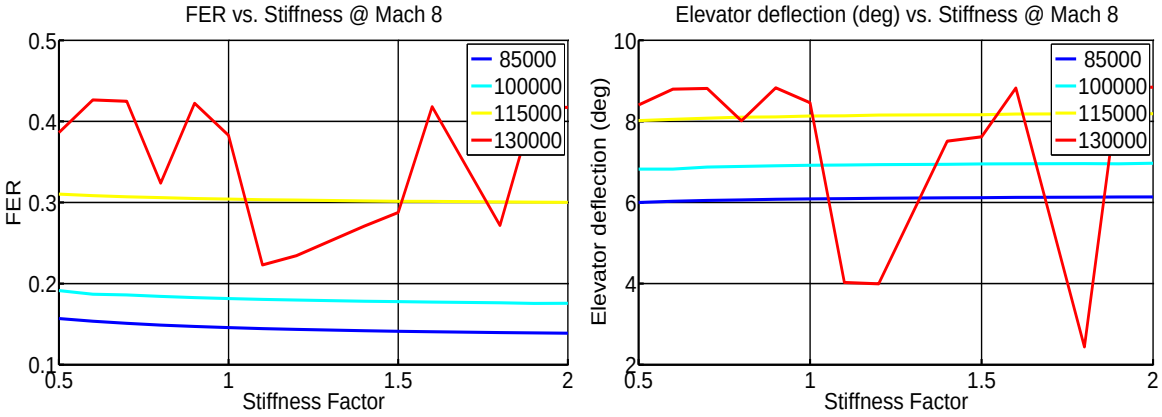

Trim FER Trim Elevator

Figure 90: Trim FER, Elevator with Stiffness

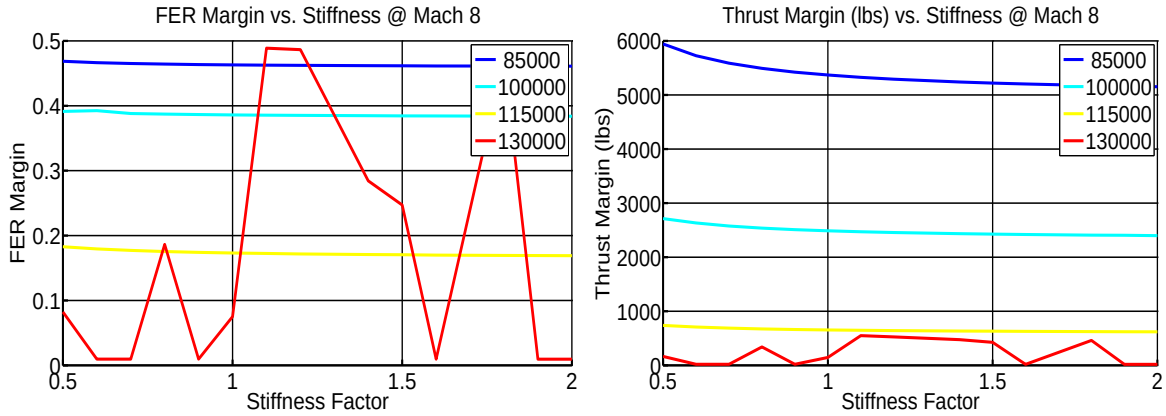

FER Margin Thrust Margin

Figure 91: FER and Thrust Margin with Stiffness

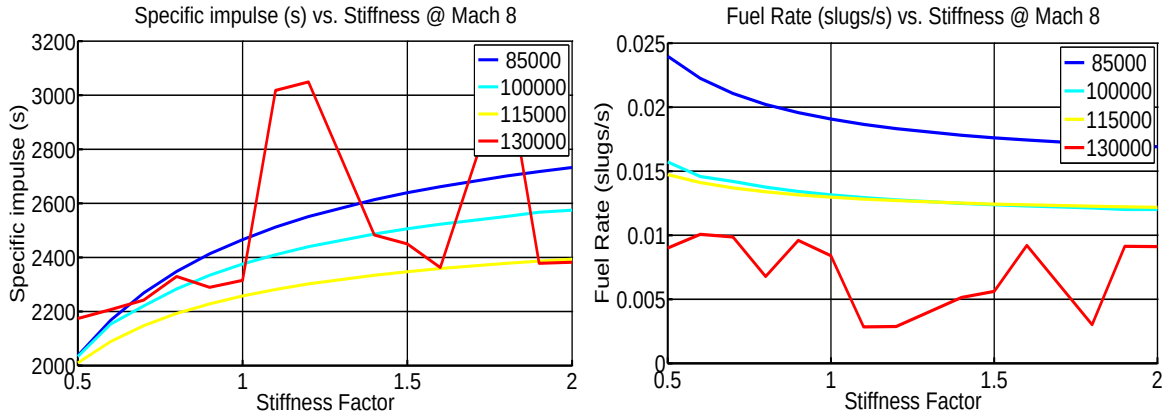

Specific Impulse Fuel Rate

Figure 92: Fuel Rate and Specific Impulse with Siffness

A.9.2 Dynamic Properties

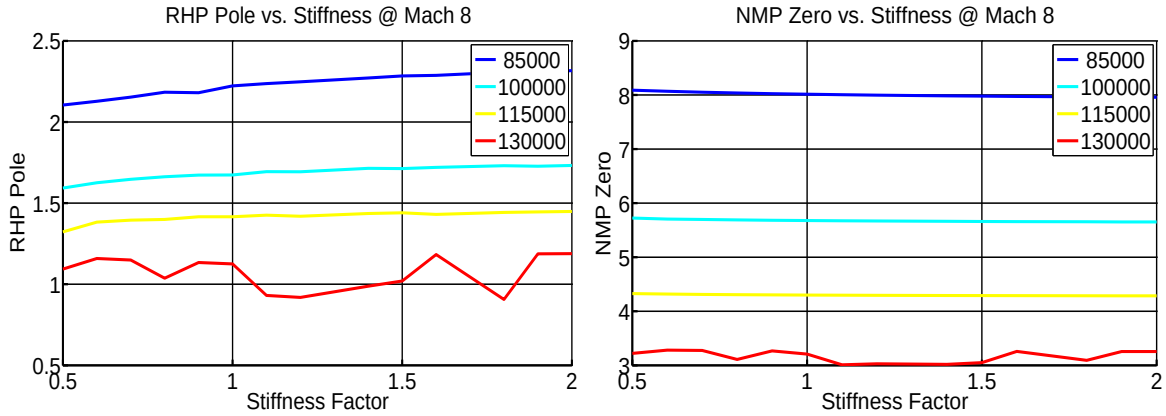

RHP Pole NMP Zero

Figure 93: Pole and Zero with Stiffness

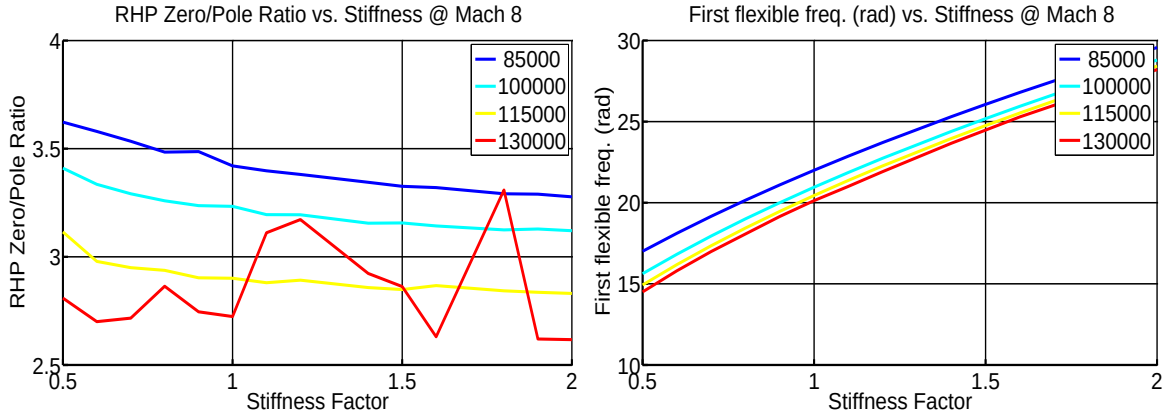

Zero Pole Ratio First Flexible Mode

Figure 94: Zero-Pole Ratio, Flexibility with Stiffness

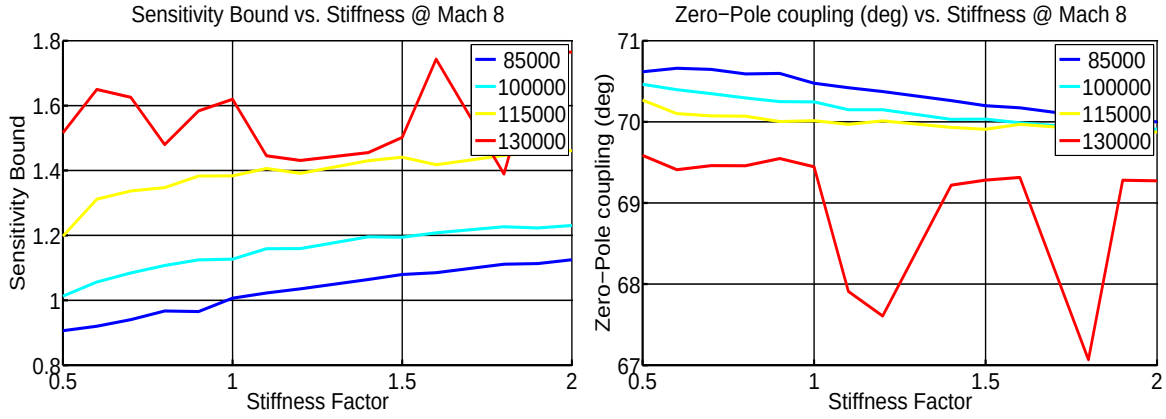

Sensitivity Bound Pole Zero Coupling

Figure 95: Zero Pole Impact with Stiffness

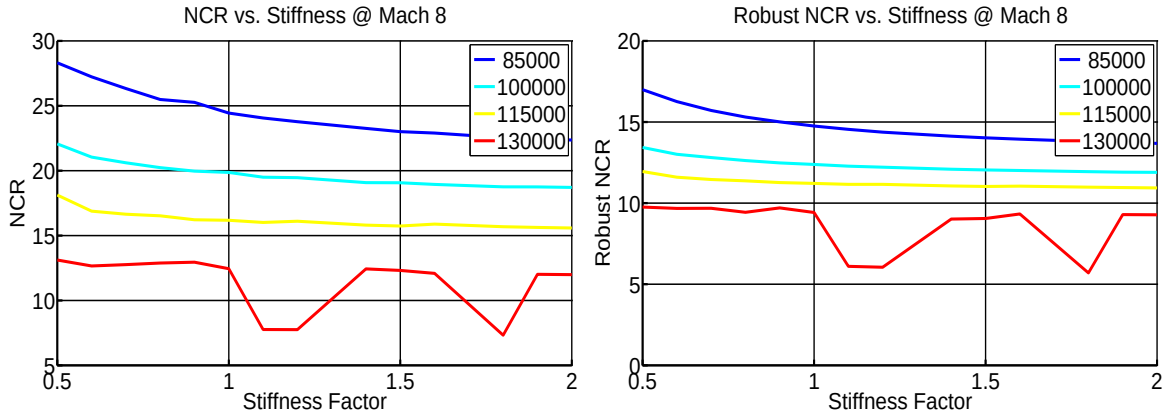

NCR Pole Zero Coupling

Figure 96: (R)NCR variation with Stiffness

A.10 Table of Results

We summarize the results of the trade studies using the tables below. The parameters considered were:

- Elevator Location (L_{elev}) and Size (k_{Elev}).
- Engine location (L_{eng}) and inlet height (h_i).
- Upper nose inclination (τ_U) and lower nose inclination (τ_L).
- Stiffness EI.

The legend for the table is given below:

- $\uparrow$: Increases.
- $\nearrow$: Increases (almost) linearly.
- $\downarrow$: decreases.
- $\searrow$: Decreases (almost) linearly.
- $\cap$: Concave (and attains maximum).
- $\cup$: Convex (and attains minimum).
- $-$: No significant impact.

A.10.1 Static Properties

Table A.1 lists the impact of vehicle design decisions on the static properties of the vehicle. The trends are listed at trim.

The first flexible mode frequency increases linearly with EI; the other parameters do not significantly impact it.

Property	AOA	Drag	FER	Elevator	FER Margin	Thrust Margin
Rearward L_{elev}	$\uparrow$	$\downarrow$	$\downarrow$	$\downarrow$	$\uparrow$	$\uparrow$
Increasing S_e	$-$	$\cup$	$\cup$	$\downarrow$	$-$	$-$
Increasing h_i	$\nearrow$	$\searrow$	$\downarrow$	$\searrow$	$\uparrow$	$\nearrow$
Rearward L_{eng}	$\searrow$	$\nearrow$	$\nearrow$	$\uparrow$	$-$	$-$
τ_U	$\nearrow$	$\uparrow$	$-$	$\nearrow$	$-$	$-$
τ_L	$\searrow$	$-$	$\searrow$	$\nearrow$	$\searrow$	$-$
Increasing EI	$\nearrow$	$-$	$-$	$-$	$-$	$-$

Table A.1: Impact of parameters on static vehicle properties

Property	RHP Pole	NMP Zero	Z/P Ratio	Sensitivity Bound Bound	Zero-Pole Coupling
Rearward L_{elev}	$\searrow$	$\nearrow$	$\nearrow$	$\downarrow$	$\downarrow$
Increasing S_e	$\searrow$	$-$	$\uparrow$	$\downarrow$	$\downarrow$
Increasing h_i	$\searrow$	$\searrow$	$\uparrow$	$\downarrow$	$\downarrow$
Rearward L_{eng}	$\uparrow$	$\nearrow$	$\downarrow$	$\uparrow$	$\uparrow$
Increasing τ_U	$\nearrow$	$\nearrow$	$\downarrow$	$\nearrow$	$\nearrow$
Increasing τ_L	$\nearrow$	$\nearrow$	$\downarrow$	$\nearrow$	$\searrow$
Increasing EI	$\uparrow$	$-$	$\downarrow$	$\uparrow$	$\downarrow$

Table A.2: Impact of parameters on dynamic vehicle properties

A.10.2 Dynamic Properties

The dynamic properties of the trade studies is given in Table A.2. It should be noted that a decrease in coupling between the pole and zero is achieved through an increase in the angle between the pole and zero directionality.